ULTRASONIC TRANSDUCERS FOR WIDEBAND ATTENUATION MEASUREMENTS

J.BERTRAND MAYER

Submitted to the University of Cape-Town
in fulfilment of the requirements for the
degree of Master of Science in Engineering

July 1987

ABSTRACT

An application of ultrasound presently being investigated at the Council for Mineral Technology (MINTEK) is the measurement of the concentration of graphite particles in suspension in an agitated pulp. The principle of the measurement is based on the attenuation characteristics of the medium over a frequency range extending from 0.1 MHz to 10 MHz. This wide range and the highly attenuating medium (typically 3 dB/cm) require therefore that the ultrasonic transducers exhibit efficient wideband characteristics.

Piezoceramic transducers vibrating in thickness-mode are the most suitable to generate ultrasound at these frequencies. However, their high acoustic impedances relative to their liquid loads make them inherently narrowband and inefficient. To overcome these undesirable features, impedance matching techniques are used whereby the impedance mismatch between a transducer and its load is reduced. In this thesis, various electrical and acoustic impedance matching schemes were implemented on a number of commercial PZT5A transducers which were then evaluated in terms of bandwidth and efficiency. At 1 MHz, the 3-dB bandwidth of a PZT5A transducer operating in pulse-echo mode in water was improved from 0.1 MHz for the unmatched case to 0.83 MHz when 2 quarter-wave matching sections were bonded to the radiating surface and an electrical matching section was inserted at the electrical port. The resulting 2-way Insertion Loss over the pass band was 16 dB. Similarly, the 3-dB bandwidth of a 500 kHz PZT5A transducer improved from 50 kHz to 138 kHz with an accompanying Insertion Loss of 12 dB when both electrical and acoustic impedance matching were implemented.

Certain radiation characteristics of thickness-mode transducers such as beam directivity and radiation resistance were investigated as functions of the "diameter to wavelength" ratio, D/λ , of the radiating transducer. Maximum radiation resistance (and therefore maximum acoustic coupling) was observed when $D/\lambda = 13$. The same ratio also produced the best performance in terms of directivity and sensitivity to parallelism between transmitter and reflector (or receiver).

A comprehensive study of the resonance spectra of flexural, in-plane and thickness-mode vibrations of thin disks was also performed using various materials commonly used in transducer construction. The elastic constants of the materials were then determined by three different methods, each method making use of a different resonance spectrum.

KEYWORDS: ULTRASONIC, PIEZOELECTRIC, TRANSDUCER, WIDEBAND, IMPEDANCE MATCHING

DECLARATION

I declare that this thesis is my own work unless indicated to the contrary in the text.

signature removed

B. Mayer

ACKNOWLEDGEMENTS

I would like to thank my supervisor, Prof. J.F.W. Bell, for his help and encouragement throughout the duration of this thesis.

I am also very grateful to the Council for Mineral Technology (MINTEK) for providing financial assistance during the course of the project.

Thanks also go to those members of the staff of the Department of Electrical Engineering who have been of assistance in one way or another.

TABLE OF CONTENTS

LIST OF FIGURES

LIST OF TABLES

CHAPTER 1

GENERAL INTRODUCTION

1.1 Background

A current research programme at the Council for Mineral Technology (MINTEK) consists of an investigation in the use of ultrasound for instrumentation purposes in the mining industry. Two preliminary investigations which have produced encouraging results are namely the measurement of the concentration of graphite granules in an agitated pulp and the on-line measurement of slurry densities. Each application exploits a different property of ultrasound. The measurement of graphite concentration in pulp is based on the fact that the attenuation of ultrasound at high frequencies (typically 1 MHz) through a medium containing particles in suspension is mostly due to the scattering of the acoustic waves by the suspended particles. In the density measurement case, the density of the medium is inferred from its acoustic impedance which is directly proportional to density.

The performance of any instrument based on the use of ultrasound is highly dependent on the characteristics of the ultrasonic transducers used. Three major areas of application of ultrasound are medical imaging, non-destructive testing and surface-wave signal processing devices. In all three applications, the transducers play a key role in the performance of the instruments. Similarly, in the measurements of graphite concentration and slurry density, the transducers are critical and must therefore be designed carefully so as to obtain optimum performance. Recent developments in the use and application of ultrasound have led to new techniques for designing and constructing ultrasonic transducers. A transduction mechanism commonly used for generating and detecting ultrasonic waves is the piezoelectric behaviour of certain materials such as quartz, a naturally occuring crystal, and lead zirconate-titanate (PZT), a piezoceramic. The latter forms part of an important group of piezoelectric materials due

to its high piezoelectric coupling coefficient and its ability to be moulded into components of almost any shape and size. However, piezoceramics are characterized by high acoustic impedances relative to water which makes them inefficient as radiators of ultrasound and narrowband devices. These undesirable features inherent to piezocaremics can be overcome by the implementation of impedance matching techniques at both the acoustic and electrical ports of the transducers.

Due to the varying nature of the uses of ultrasound at MINTEK, the transducers must be designed to suit the particular needs of each application. In the measurement of graphite concentration in pulp, there is a need for efficient wideband piezoelectric transducers operating in water at frequencies ranging from 100 kHz to 10 MHz. To achieve a 3-dB response over this frequency range, it is necessary to use an array of transducers where each transducer operates over a different section of the frequency spectrum. By using wideband transducers it is possible to reduce significantly the number of elements constituting the array and thereby simplify the analysis of the results.

The measurement of slurry density is based on the fact that the acoustic impedance of a medium is directly proportional to its density. In this application a design criterion for the transducer is that it must exhibit strong acoustic coupling to the surrounding medium. This ensures that the internal losses within the transducer are small compared to the energy radiated in the medium. The first experimental results obtained at MINTEK indicated that it was indeed possible to infer the density of a slurry from a measurement of its acoustic impedance. It is envisaged that a more sensitive instrument can be developed if the transducer is designed for maximum coupling with the surrounding medium.

1.2 Objectives of thesis

Two applications of ultrasound discussed in the previous section have identified the need for transducers which exhibit wide bandwidths and high electromechanical efficiencies. These two properties cannot usually be achieved simultaneously since an enhancement in bandwidth is invariably accompanied by a drop in efficiency. Thus, for a given application, an optimum trade-off between the bandwidth of a transducer and its efficiency must be found. It is therefore important to establish the performance criteria of a transducer in the context of its application before proceding to the design and construction stages.

The main objective of this thesis is to carry out a comprehensive theoretical and practical study of the various aspects of the design and construction of ultrasonic transducers. For this purpose, a number of lead zircanate-titanate (PZT5A) disks of various dimensions and resonant frequencies were used. These piezoelectric disks, when used in thickness-mode, posess high piezoelectric coupling coefficients and are therefore efficient at converting electrical energy to mechanical energy and vice versa. However, due to their high acoustic impedance relative to water, the mechanical coupling between the transducers and the surrounding medium is poor, resulting in low energy transfer and narrow bandwidth. To overcome this impedance mismatch, various design techniques have been developed which are based on the use of impedance matching schemes at both the electrical and acoustic ports of the transducer. One of the objectives of this thesis consists of investigating the various matching techniques used on PZT disks operating in media of acoustic impedances comparable to that of water. Acoustic impedance matching via the use of quarter-wave front matching layers is to be implemented and evaluated in terms of bandwidth and efficiency. Similarly, electrical impedance matching is to be implemented by means of impedance transformers and tuning components and evaluated.

Another factor which affects the mechanical coupling between a transducer and its loading medium is the D/λ ratio of the

transducer, i.e. the ratio of the diameter of the transducer to the wavelength of the acoustic wave generated in the medium. Furthermore, this ratio determines certain characteristics of the radiated beam of ultrasound such as, for example, the extent of the near field and the beamwidth. A knowledge of these beam characteristics is very useful in certain applications where the spreading of the beam is to be minimized. A study of the relationship between mechanical coupling and the D/λ ratio is to be carried out,paying particular attention to improvements in bandwidth and efficiency. A qualitative assessment of the effects of the D/λ ratio on beam characteristics is to be performed as well.

The ultimate aim of this project is to design and construct piezoelectric transducers which offer the optimum trade-off between bandwidth and efficiency for the two applications discussed previously, namely the measurements of graphite granule concentration in pulp and slurry density. In the first application, bandwidth is the main criterion whilst, in density measurement, acoustic coupling between the transducer and the surrounding medium is the major design preoccupation. Wideband piezoelectric transducers are to be designed and constructed using both electrical and acoustic impedance matching on PZT disks whose resonant frequencies lie in the frequency range of interest, i.e. from 0.1 to 10 MHz. For the measurement of slurry density, piezoelectric transducers exhibiting high radiation efficiencies at resonance are to be implemented. In addition, the dimensions of the transducers must be carefully chosen in both applications so that the optimum D/λ ratios are obtained.

Besides the acoustic constraints imposed on the transducers discussed above, certain physical considerations must also be taken into account. In both the graphite concentration and slurry density measurements, the instruments are to operate in very abrasive liquids over a temperature range of $10^{o}C$ to $40^{o}C$. Robustness and temperature stability are therefore important design considerations. Furthermore, the construction of the transducers must be made simple with the use of readily available materials.

1.3 Literature review

The implementation of efficient broadband transducers using piezoelectric ceramics has been the subject of extensive research in the last two decades. Non-destructive testing and medical imaging are two areas which have prompted most of the resarch in the field. A review of the various design techniques used for enhancing the bandwidth and efficiency of piezoelectric transducers is given in this section together with some pubished data on the performance of a number of transducers.

Equivalent electrical models form the basis of most transducer design techniques which involve the implementation of acoustic and electrical impedance matching. A widely used model for thickness mode transducers is the one developed by Mason [1]. The transducer is considered as a six terminal device, one pair representing the electrical port, and the other two, the mechanical ports on either side of the transducer. This model allows the transducer to be analysed for different loads on either side of the transducer, as is often the case when lossy or air backings and quarter-wave front matching layers are implemented on the transducer. A second model, developed more recently by Krimholtz et. al. [2] and known as the KLM model, uses transmission line formalism and, therefore, lends itself to the analysis of cascaded acoustic circuits as found in the implementation of multiple quarter-wave matching layers. Both the Mason and KLM models are confined to analysis in the frequency domain, i.e. they yield the frequency response of the transducer. If the impulse response is required, an inverse Fourier transform must be performed on the frequency response. An alternative model which permits the direct analysis of a thickness mode piezoelectric transducer in the time domain is the discrete time model developed by Hayward and Jackson [3]. However, this model can only be analysed on a computer since it utilizes z-transforms and digital filter theory.

A successful implementation of acoustic impedance matching techniques on a number of PZT7A transducers operating in water was realised by Kossoff [4]. Using the Mason model as the

electromechanical equivalent circuit, he analysed the frequency response of a piezoelectric transducer for a variety of matching conditions at the acoustic ports. 3-dB bandwidths of up to 90% were reported. Goll and Auld [5] also implemented a double-layer impedance matching scheme on a PZT5A transducer and reported a 70% 3-dB bandwidth with a 2-way Insertion Loss of 6 dB. A design method based on the KLM model has been developed by Desilets et. al. [6], and implemented on a PZT5A disk. A 3-dB bandwidth of more than an octave was otained, with an accompanying Insertion Loss of 3.2 dB. Souquet et. al. [7] reported a 74% 3-dB bandwidth accompanied by a 1-way Insertion Loss of less than 5 dB for a PZT5A transducer implemented with two quarter-wave front matching layers and a mismatched backing. Another article of interest by Houze et. al. [8] describes how the bandwidth of a thickness mode piezoelectric transducer can be enhanced by the right choice for the diameter of the disk. This technique is especially useful when acoustic matching and damping are not always possible owing, for example, to technical difficulties in machining quarter-wave matching layers for high frequency applications.

1.4 Contents of thesis

Due to their electromechanical nature, piezoelectric transducers encompass a variety of disciplines such as, for example, vibration of solids, electric circuit theory and acoustics. In this thesis, three broad aspects of thickness mode piezoelectric transducers are investigated. These fall under the following general headings:

(i) Vibrations of disks and rods and their application in material characterisation.

(ii) Radiation characteristics of thickness-mode piezoelectric transducers.

(iii) Equivalent electrical models for thickness-mode piezoelectric transducers and their application in impedance matching schemes.

A study of the resonance spectra of the various modes of vibration of disks and rods and a technique for determining the elastic properties of a material are described in Chapter 2. A pulse-echo system based on a magnetostrictive acoustic transmission line is used to determine experimentally the in-plane and flexural resonances of disks and the longitudinal resonances of rods of a number of different materials. The elastic constants of the materials, i.e. Poisson's ratio and Young's modulus, are then calculated from the resonance spectra. Various epoxies and resins which are used in the construction of wideband piezo-electric transducers are characterised by this method. The complex interaction between the flexural and thickness modes of vibration of a disk is illustrated for different diameter to thickness ratios. Although the in-plane vibrations of disks do not generate ultrasound, they play an important part in the design of ultrasonic transducers owing to the piezoelectric coupling of certain modes, e.g.the "breathing" mode. It is therefore important that these modes be remote from the thickness ones in the frequency spectrum. This is achieved by properly choosing the dimensions of the transducer. The piezoelectric coupling of the "breathing" mode is demonstrated on the pulse-echo system and its position in the frequency spectrum noted.

In chapter 3, two aspects of the radiation characteristics of thickness-mode piezoelectric transducers are investigated. These are, firstly, the radiation impedance of the loading medium acting on a transducer, and secondly, the radiation beam pattern of a transducer when operating as a transmitter. Radiation impedance represents the mechanical loading of the medium surrounding a transducer and possesses a resistive and a reactive component. The resistive component is due to the acoustic energy radiated in the loading medium while the reactive component is a result of the mass loading of the medium onto the transducer. A theoretical analysis of the radiation impedance of a circular piston vibrating in a loading medium indicates that the magnitudes of both the resistive and reactive components are functions of the D/λ ratio. This is verified experimentally by measuring the radiation impedances of a number of transducers of various D/λ ratios operating in

water. The resistive and reactive components are determined from admittance circle diagrams obtained for each transducer and plotted against D/λ. The experimental trends are then compared with theory and the possibilities of maximizing radiation resistance, and hence acoustic coupling, by proper choice of the D/λ ratio are investigated.

Radiation beam characteristics such as the extent of the near-field and the beamwidth play an important part in certain applications where, for example, the spreading of the beam generated by a transducer must be low, i.e. the transducer must be highly directional. A qualitative assessment of the effects of the D/λ ratio on the beam characteristics of thin disk thickness-mode transducers operating in water is performed by means of four PZT5A disks of resonant frequency 2 MHz and diameters ranging from 5 to 40 mm. Relative measurements of directivity and near-field extent are made in pulse-echo mode and subsequently plotted against D/λ.

The third and most important aspect of thickness-mode piezoelectric transducers is the application of equivalent electrical models in transducer design. Chapters 4 and 5 are devoted to the implementation of impedance matching techniques on PZT transducers for bandwidth and efficiency enhancements. Electrical impedance matching via the use of impedance transformers and tuning inductors and capacitors is covered in Chapter 4. A number of PZT5A disks of various dimensions and resonant frequencies are configured with different matching circuits at their electrical port and the corresponding frequency responses are measured in pulse-echo mode. The simple electrical model for thickness-mode piezoelectric transducers is used to explain the effects of the matching circuits on the frequency responses. Furthermore, a technique is developed for designing an appropriate electrical matching circuit so as to enhance the bandwidth and efficiency of a given thickness-mode piezoelectric transducer.

Acoustic impedance matching via the use of one or more quarter-wave matching layers at the front face of a thickness-mode transducer is investigated in Chapter 5. Two PZT5A disks of

resonant frequencies 500 kHz and 1 MHz respectively are first implemented with one quarter-wave layer and calibrated by measuring their 2-way Insertion Loss as a function of frequency. Improvements in bandwidth and efficiency over the unmatched cases are noted. The same transducers are then implemented with two quarter-wave matching layers and calibrated as before. The results are then compared with previous ones and further improvements in bandwidth noted. Finally, the combined effects of acoustic and electrical impedance matching are investigated. The two acoustically matched transducers are matched electrically as well and their 2-way Insertion Losses are measured and compared with previous results.

An alternative way of determining the frequency response of a pulse-echo transducer is proposed in Chapter 5. It consists of exciting the transducer with a square pulse of a certain duration and sampling the echo response. A Fast Fourier Transform (FFT) performed on the sampled data then yields the frequency response of the transducer operating in pulse-echo mode. This technique is implemented using a digital storage oscilloscope fitted with an HP-IB interface for sampling the echo response and an HP-85 computer to perform the FFT operation. The validity of this technique is confirmed by using it to calibrate a number of transducers and comparing their frequency responses with those obtained by direct measurement.

CHAPTER 2

VIBRATIONS OF DISKS AND RODS

2.1 Introduction

Thin disks and cylindrical rods vibrate in a large number of different modes, some of which have relatively simple geometries and others, more complicated ones. The simple modes have been analysed mathematically in a number of textbooks [9,10] and solved for various boundary conditions. In this chapter, the modes of vibration that are investigated are limited to flexural, in-plane and thickness-mode vibrations of disks, and longitudinal vibrations of rods. These modes are particularly relevant to the study of thickness-mode ultrasonic transducers due to the nature of their motion. Before going into further details about the contents of this chapter, it is necessary to describe the motion of the various modes which have been analysed.

(i) Longitudinal or thickness-mode vibrations

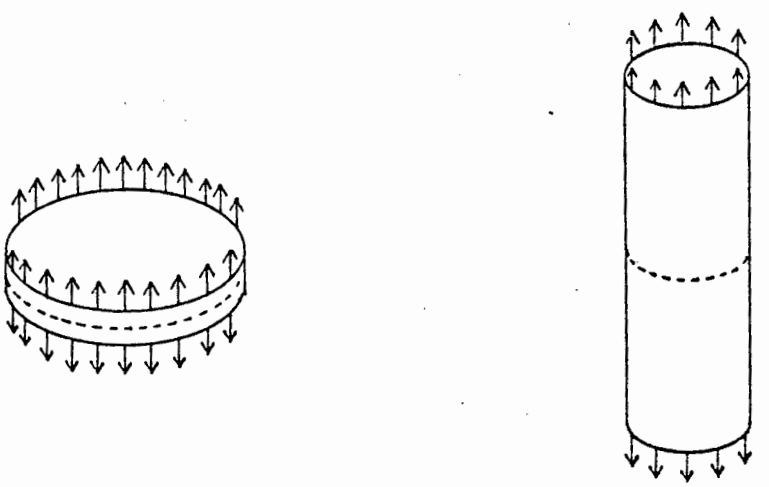

(i) (ii)

Figure 2.1: Fundamental modes of longitudinal vibration of (i) thin disk and (ii) cylindrical rod. The net strain produced along the axis of the disk/rod enables piezoelectric excitation.

This type of vibration is characterised by particles vibrating parallel to the axis as shown in Figure 2.1. A distinguishing feature of longitudinal vibrations is the net resultant strain which is produced along the axis of the solid as it expands and contracts, thus allowing this type of motion to be excited piezoelectrically. Furthermore, thin disks vibrating in thickness-mode exhibit strong acoustic coupling to the surrounding medium owing to the large surface area that is loaded by the medium.

(ii) Flexural vibrations

(i) (ii)

Figure 2.2: Two modes of flexural vibrations: (i) mode [1,0] (ii) mode [0,2]. The resultant strain across the thickness of the disk is always zero.

Flexural vibrations of disks are characterised by particles moving transversely to the plane as shown in Figure 2.2 above. The notation used to describe the various modes is [m,n], where m is the number of nodal circles and n, the number of nodal diameters. As a disk vibrates flexurally, the one half of the disk is in compression while the other half is in tension as seen from Figure 2.2 (i). Thus, the resultant strain across the thickness of the disk is always zero and, consequently, flexural vibrations do not respond to piezoelectric excitation.

(iii) In-plane vibrations

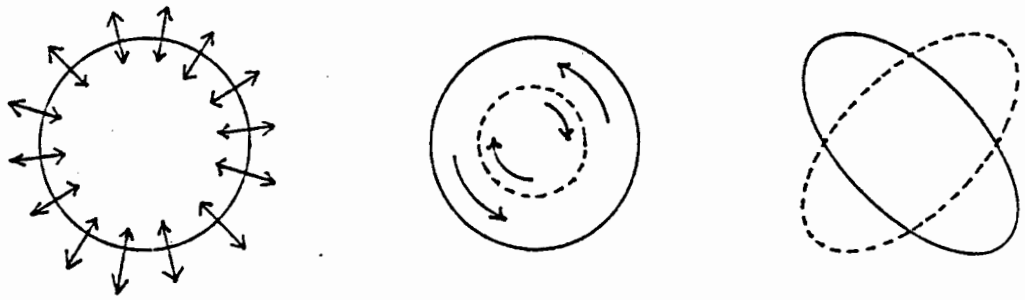

(i) (ii) (iii)

Figure 2.3: Three classes of in-plane vibration: (i) Radial, (ii) Torsional, (iii) Compound. The radial mode exhibits a net areal change and therefore couples pizoelectrically.

In-plane vibrations of disks, also known as contour extensional vibrations, are characterised by particles moving in the plane of the disk. These are classified in three general modes, namely radial, torsional and compound modes. In radial modes, the particles have pure radial motion, while in torsional modes, they have rotational motion only, as seen from Figure 2.3 above. Compound modes are characterised by particles having both a radial and a rotational component of motion. The notation used to describe the various modes is [m,n], where m is the number of nodal circles and n, the number of nodal diameters. Radial modes, also known as "breathing" modes, are particularly important to thickness-mode piezoelectric transducers because of their ability to couple piezoelectrically. However, due to the small area of the disk that is loaded by the medium, radial modes exhibit very poor acoustic coupling and low radiation efficiencies.

The resonance spectra of the various modes of vibration described above are determined experimentally by a pulse-echo technique for a number of disks and rods of various dimensions machined from different materials. The elastic constants of the materials, i.e. Young's modulus and Poisson's ratio, are then calculated by three different techniques. Each technique uses

the resonance spectrum of a different mode of vibration and the results are then compared with one another. Certain epoxies and casting resins which are commonly used in the contruction of wideband ultrasonic transducers are characterised by these techniques. The interaction between the various modes of vibration is analysed in the frequency domain and the piezoelectric coupling of the "breathing" mode is demonstrated by the pulse-echo technique.

2.2 The Pulse-Echo Technique

2.2.1 Using an acoustic transmision line

Resonance spectra of disks and rods can be determined experimentally by means of a pulse-echo technique developed by Bell et. al. [11]. This technique consists of exciting a resonator by an acoustic pulse containing a number of oscillations at a certain frequency and identifying the resonances of the resonator by observing the characteristics of the echo returns as the frequency of oscillations constituting the pulse is varied. Depending on the geometric features of the resonator and the frequency range of its resonance spectra, the appropriate driving mechanism must be chosen. Two mechanisms are used in this chapter: the first one consists of a magnotostrictive source coupled to an acoustic transmission line, while the second one uses a piezoelectric source in water. The maximum frequency which can be generated by a magnetostrictive source is limited to about 500 kHz, whereas in the case of a piezoelectric source, the limit depends on the operating range of the source.

The magnetostrictive acoustic transmission line technique is used extensively to determine the resonance spectra of flexural and in-plane vibrations of thin disks, and longitudinal vibrations of rods. A schematic diagram of the system is given in Figure 2.4 below.

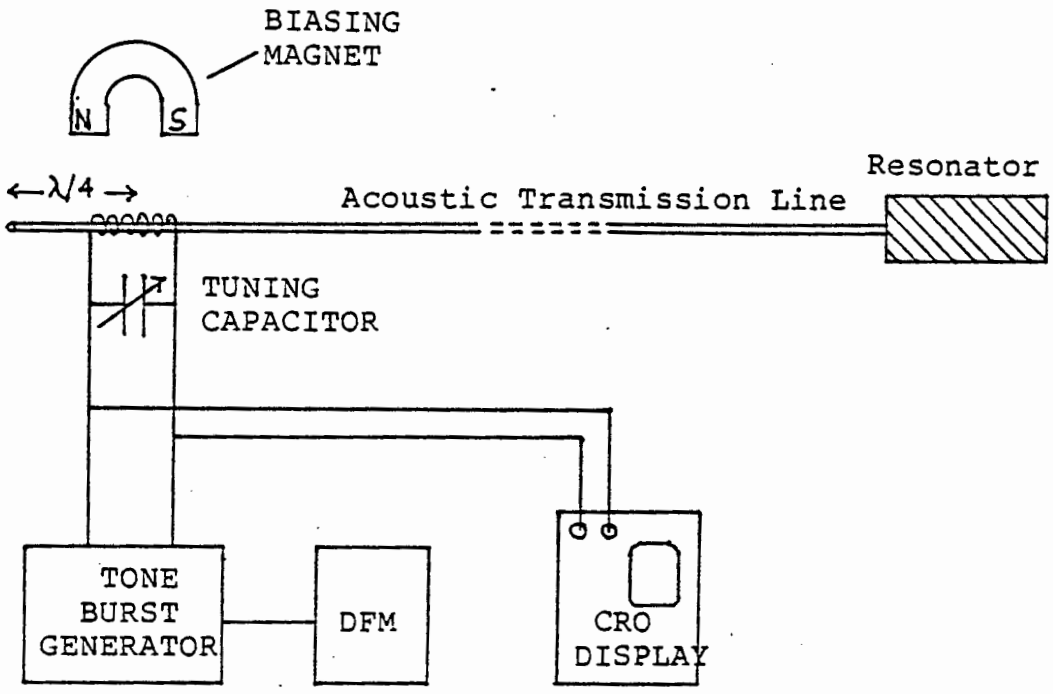

Figure 2.4: Schematic diagram of the magnetostrictive pulse-echo system.

The main features of the system are:

(i) A magnetostrictive source, made by winding a coil around a piece of nickel wire and exciting the coil with an a.c voltage, is used to transmit and receive a burst of longitudinal stress waves along the acoustic transmission line. Due to the non-linearity of the magnetostrictive phenomenon, a biasing magnet is placed near the coil to improve the efficiency of the source. In addition, a tuning capacitor is connected across the coil to allow maximum current flow.

(ii) An acoustic transmission line, usually made of nickel, links the resonator to the magnetostrictive source. By appropriately positioning the end of the transmission line on the resonator,it is possible to excite certain modes of vibration only, while leaving other modes unexcited. An essential constraint imposed on the line is that it must

be sufficiently long to prevent interference between the driving pulse and the echo.

(iii) An oscilloscope displays the echo signal from the resonator. By the reverse effect of magnetostriction, the acoustic echo from the the resonator, upon reaching the coil, generates an electrical voltage across it, the features of which are the same as the acoustic echo.

(iv) A digital frequency meter measures the frequency of the oscillations in the burst.

The procedure for determining the resonance spectrum of a particular mode of vibration of a disk or rod firstly consists of selecting the appropriate drive technique,i.e., placing the end of the acoustic line in the correct position and orientation on the resonator. Figure 2.5 illustrates the various drive techniques for exciting flexural and in-plane vibrations of disks and longitudinal vibrations of rods.

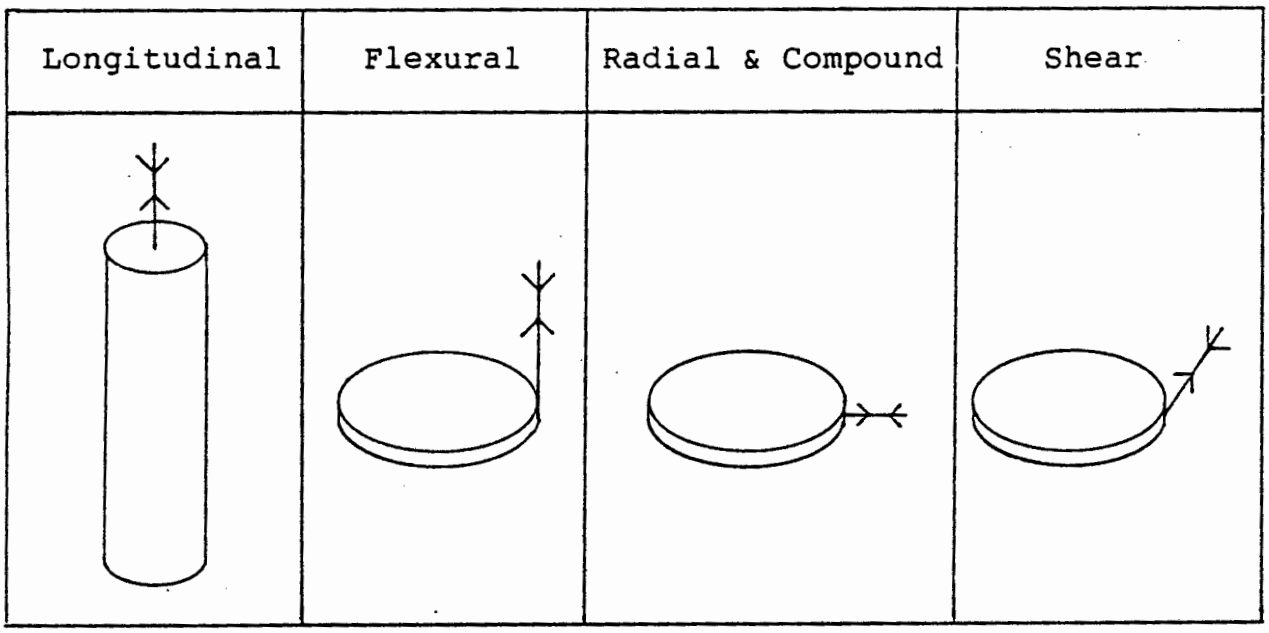

Figure 2.5: Driving techniques for various modes of disk and rod vibrations.

After selecting the appropriate drive for a particular mode of vibration, the resonance spectrum of the resonator is determined by observing the shape of the echo on the

oscilloscope as the frequency of the oscillations in the burst is varied. At resonance, the echo is characterised by a distinctive phase-sensitive null as shown in Figure 2.6 (i), providing a precise setting of frequency. However, if the mechanical coupling between the line and the resonator is weak, the echo obtained does not have a null as shown in Figure 2.6 (ii). The extent to which the transmission line couples to the resonator is determined by, amongst other factors, the thickness of the wire and the size of the resonator at the point of contact. Thus, to obtain good echoes, it is important that for a given resonator, the transmision line is of adequate thickness. A theoretical description of the pulse-echo system and the echo behaviour near resonance for simple resonators is given in [12].

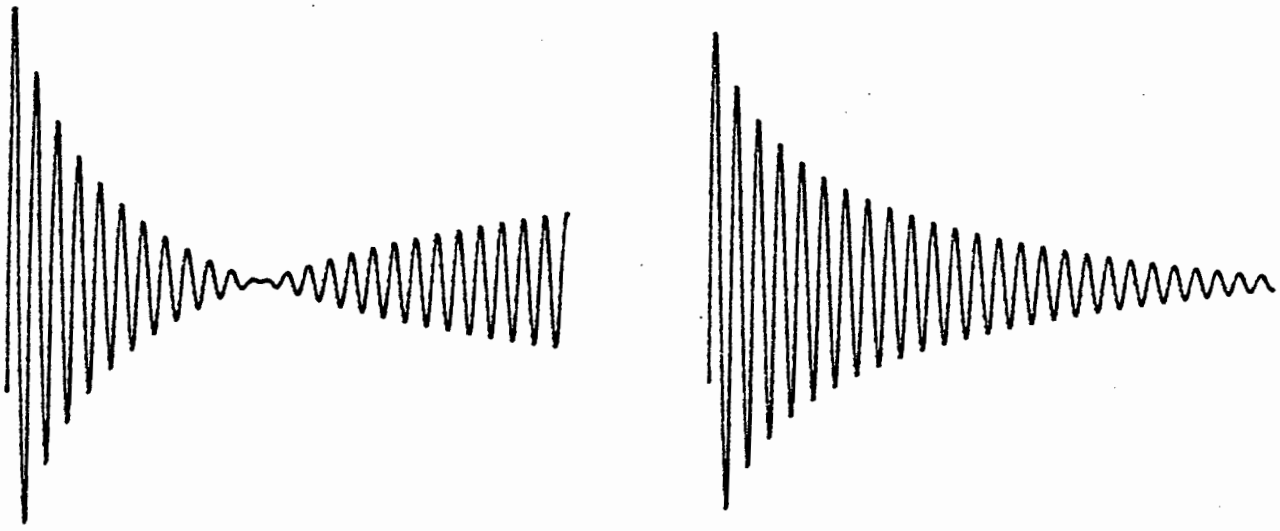

(i) (ii)

Figure 2.6: Two echo signals with the features of resonance. The signal in (i) shows a null and therefore indicates strong coupling between the resonator and the line. The signal in (ii) is characterised by weak coupling.

2.2.2 Using a piezoelectric source in water

Thickness-mode vibrations of thin disks cannot normally be analysed by means of the magnetostrictive transmission line technique for two main reasons. Firstly, the frequencies of the resonance spectra are often too high for the operating range of the magnetostrictive source, and secondly, the mechanical coupling between the disk and the wire is poor due to the

acoustic impedance mismatch at the point of contact. This mismatch is a result of the large difference in the cross-sectional areas of the disk and the transmission wire.

An alternative method for exciting thickness-mode vibrations in thin disks consists of replacing the magnetostrictive source and the transmission line by a piezoelectric transducer immersed in water as shown in Figure 2.7. Here, plane waves are incident on the disk, thereby exciting it in thickness-mode. The resonator serves as a reflector to the transmitted pulse so that, when the frequency of oscillations in the pulse corresponds to one of the thickness-mode resonances of the resonator, the echo picked up by the transducer has the characteristics of Figure 2.6. In this system, the frequency range over which a resonator can be analysed is limited by the bandwidth of the transducer. A broadband transducer will therefore allow a wider section of the resonance spectrum of a resonator to be analysed.

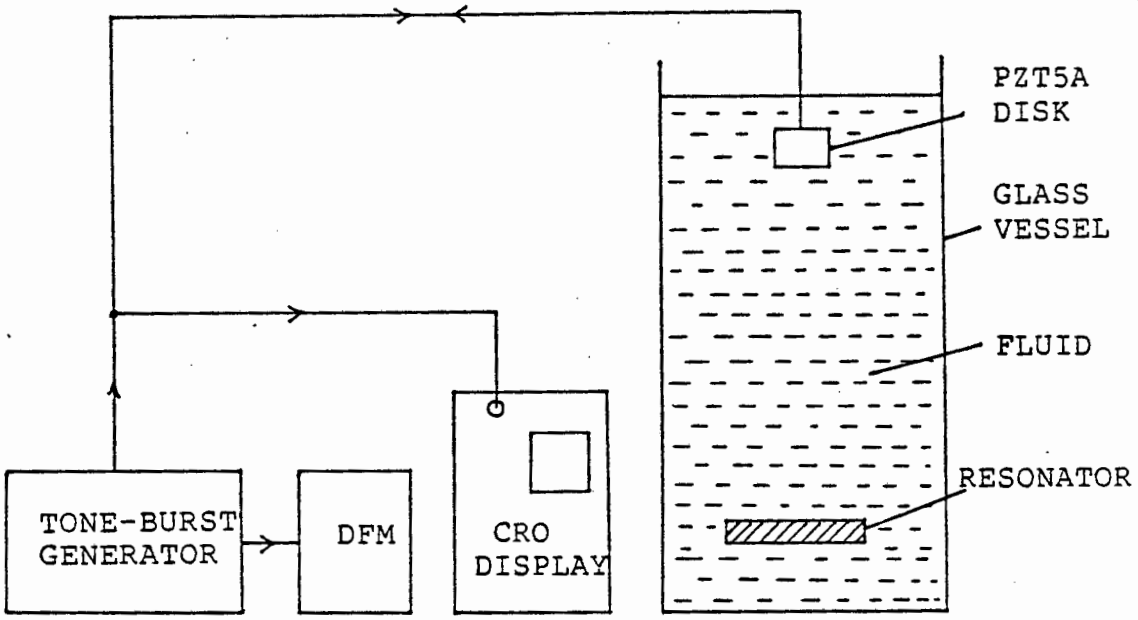

Figure 2.7: Laboratory set-up of pulse-echo system using a piezoelectric source in water. The effective bandwidth of the system depends on the bandwidth of the transducer.

2.3 Longitudinal vibrations of disks and rods

2.3.1 Theory

The theory of longitudinal vibrations of rods and bars is described in detail in various textbooks [9,10,13]. This section outlines the important equations that are used to determine the resonant frequencies of a disk or rod for the case of free boundary conditions.

The wave equation describing longitudinal vibrations in a rod is given by:

$$\delta^2u/\delta t^2 = c_o^2 . \delta^2u/\delta x^2 \quad ; \quad c_o^2 = E/p \quad \ldots\ldots\ldots\ldots (2.1)$$

where $u = u(x,t)$ is the longitudinal displacement of a particle in the rod expressed as a function of time t and distance x;

E : Young's modulus for the material
p : density of material

A general solution to the wave equation of (2.1) is:

$$u(x,t) = [A \cos (wx/c_o) + B \sin (wx/c_o)] \cos wt \ldots (2.2)$$

The constants A and B are evaluated for the boundary conditions at the two ends of the rod. In this chapter, all rods are analysed with both ends free. Thus, for a free rod of length L, the general solution is given as:

$$u_n(x,t) = A_n \cos (n\pi x/L).\cos (w_n t); \quad n=1,2,3,\ldots\ldots (2.3)$$

where $w_n = n\pi c_o/L$

or $f_n = w_n/2\pi = nc_o/2L$; $\quad n=1,2,3,\ldots\ldots (2.4)$

Equation (2.3) indicates that the solution to the wave equation (2.1) for the case of a rod free at both ends consists of an infinite number of discrete solutions, each solution corresponding to a different value of n, and hence to a different frequency as seen from equation (2.4). Thus, a rod

will vibrate at certain frequencies which are determined by its length L, the longitudinal sound velocity c_o for the material, and the integer n which represents the mode of vibration.

2.3.2 Experimental Results

A number of disks and rods were machined from various materials and their longitudinal or thickness-mode resonance spectra were determined by one of the two methods described previously. The materials used include standard metals such as aluminium, steel and titanium, and various epoxies and plastics commonly used in ultrasonic work. The epoxies were moulded into thin disks and their resonance spectra were determined by the pulse-echo technique using a piezoelectric source in water. The metals on the other hand were machined into rods and analysed by the acoustic transmission line technique. The elastic constants for the materials used are then evaluated by different techniques which make use of their resonance spectra.

Six rods machined from aluminium, steel, titanium, perspex, "billiard ball" material and poco-graphite are excited in their longitudinal modes of vibration by means of the laboratory set-up of Figure 2.4. The first few modes are identified for each rod and the corresponding frequencies noted. A plot of resonant frequency versus mode number for each rod is given in Figure 2.8. It should be noted that, except for titanium, the rods are all of approximately the same length and that the six graphs are plotted on the same scale. Thus, a material of high longitudinal velocity is characterised by a steep curve. Aluminium and steel fall in this category, while the three non-metallic materials have relatively low velocities. Table 2.1 below lists the fundamental (half-wavelength) resonant frequencies f_o and the corresponding rod velocities c_o' for the six materials used.

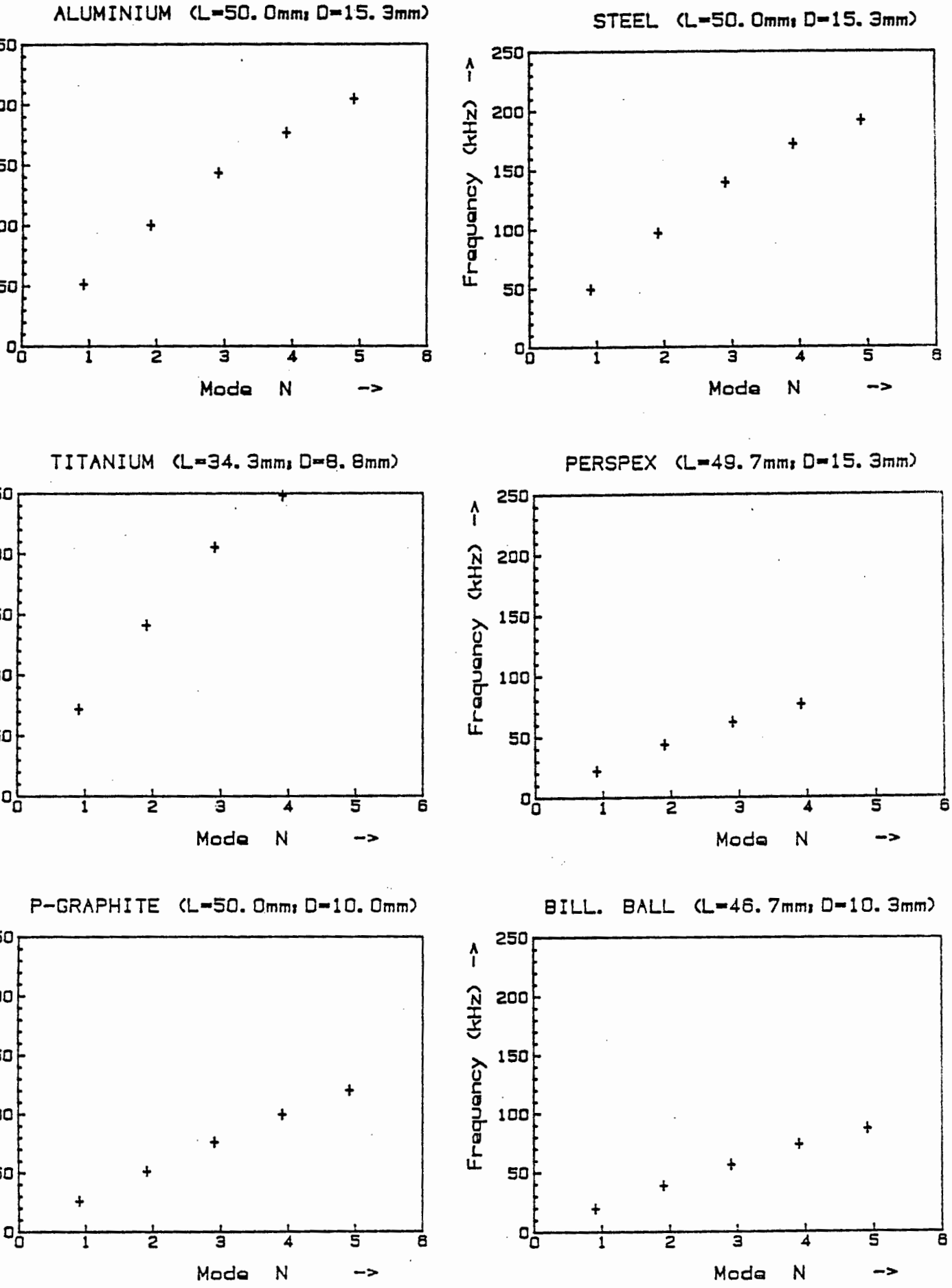

Figure 2.8: Longitudinal resonance spectra of six rods of various materials determined experimentally by the acoustic transmission line pulse-echo technique.

Material	L (mm)	f_o (kHz)	$c_o'=2f_oL$ (m/s)
Aluminium	50.0	51.1	5110
Steel	50.0	49.1	4910
Titanium	34.2	71.5	4891
Perspex	49.7	22.0	2187
P-graphite	50.0	25.7	2570
Bill. ball	46.7	19.7	1840

Table 2.1: Experimental data on longitudinal vibrations of rods

Note that the velocities tabulated above do not correspond to the actual longitudinal velocities of the materials. The lateral motion that accompanies the longitudinal vibrations of a rod of finite length and thickness causes the rod to resonate at a lower frequency. This property is exploited in the determination of the elastic constants of a material as will be shown in the next section.

The thickness-mode resonance spectra of a number of thin disks moulded from various epoxies and resins are determined by the pulse-echo technique using a piezoelectric source in water as shown in Figure 2.7. A plot of resonant frequency versus mode number for each disk is given in Figure 2.9. In each case, the points lie approximately on a straight line, indicating that there exists a harmonic relationship between successive modes. The slope of the line, df/dN, gives the fundamental resonant frequency f_o of the disk. The bulk velocity of the material is then determined from the thickness of the disk and its value of f_o. Note that in the case of thin disks, the bulk velocity must be used. This is always higher than the longitudinal wave velocity c_o of thin rods. Table 2.2 below lists the fundamental resonant frequencies and the corresponding bulk velocities c_B for the six epoxies and plastics used.

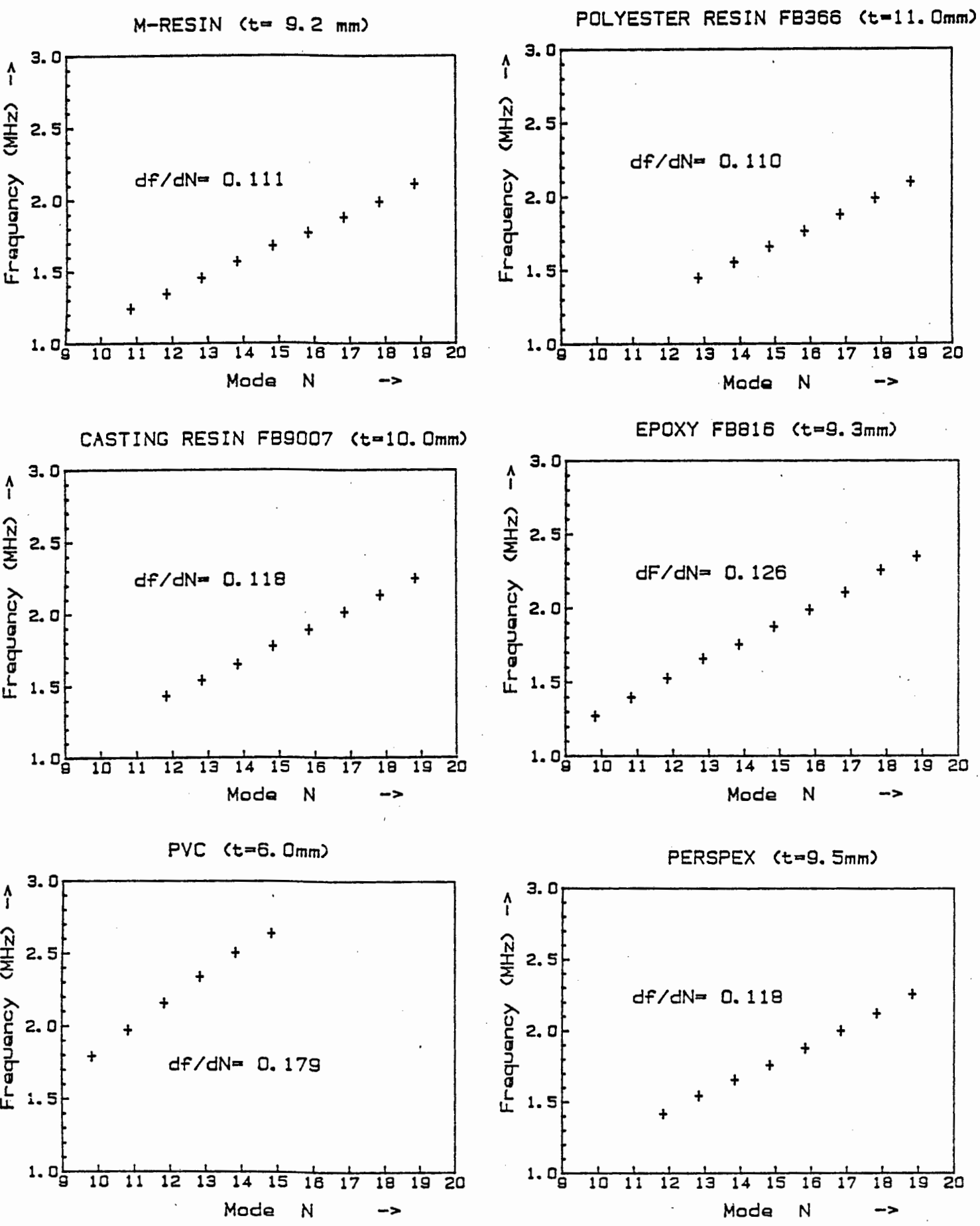

Figure 2.9: Thickness-mode resonance spectra of six disks determined experimentally by the pulse-echo technique using a piezoelectric source in water.

Material	t(mm)	f_o(kHz)	c_B(m/s)
M-Resin: HR Hardener (100:40)	9.2	111	2042
Fobroglass Polyester Resin FB366	11.0	110	2420
Fobroglass Casting Resin FB9007	10.0	118	2360
Fobroglass Epoxy FB816	9.3	126	2344
PVC	6.0	179	2148
Perspex	9.5	118	2242

Table 2.2: Experimental data on thickness-mode vibrations of thin disks made of epoxies and plastics.

2.3.3 Material characterisation using longitudinal resonance spectra.

The elastic properties of an isotropic material, i.e.Young's modulus and Poisson's ratio, can be determined from the longitudinal resonance spectrum of a rod of the material by considering the dispersive or non-harmonic nature of the spectrum. For the ideal case of a long thin rod vibrating longitudinally with both ends free, the frequency equation (2.4) indicates that there is a pure harmonic relationship between successive modes, i.e. all resonant frequencies are integral multiples of the fundamental. In practice however, the longitudinal resonance of a rod of finite length and thickness is dispersive as shown in Figure 2.10(i). This departure from the ideal case is due to the transverse motion of the rod as it vibrates longitudinally. If the longitudinal velocity c_o is to be calculated for every observed resonant frequency and plotted against mode number n, a graph as shown in Figure 2.10(ii) will be obtained.

The degree of departure of the actual velocity from the ideal value is a function of two independent variables: Poisson's ratio for the material and the diameter to wavelength ratio of the rod. Bancroft [14] derives a precise set of equations for calculating this degree of departure and computes a table relating the fractional change in velocity, c/c_o, to Poisson's ratio, σ , and diameter to wavelength ratio, D/λ . The table is reproduced in Appendix A1.

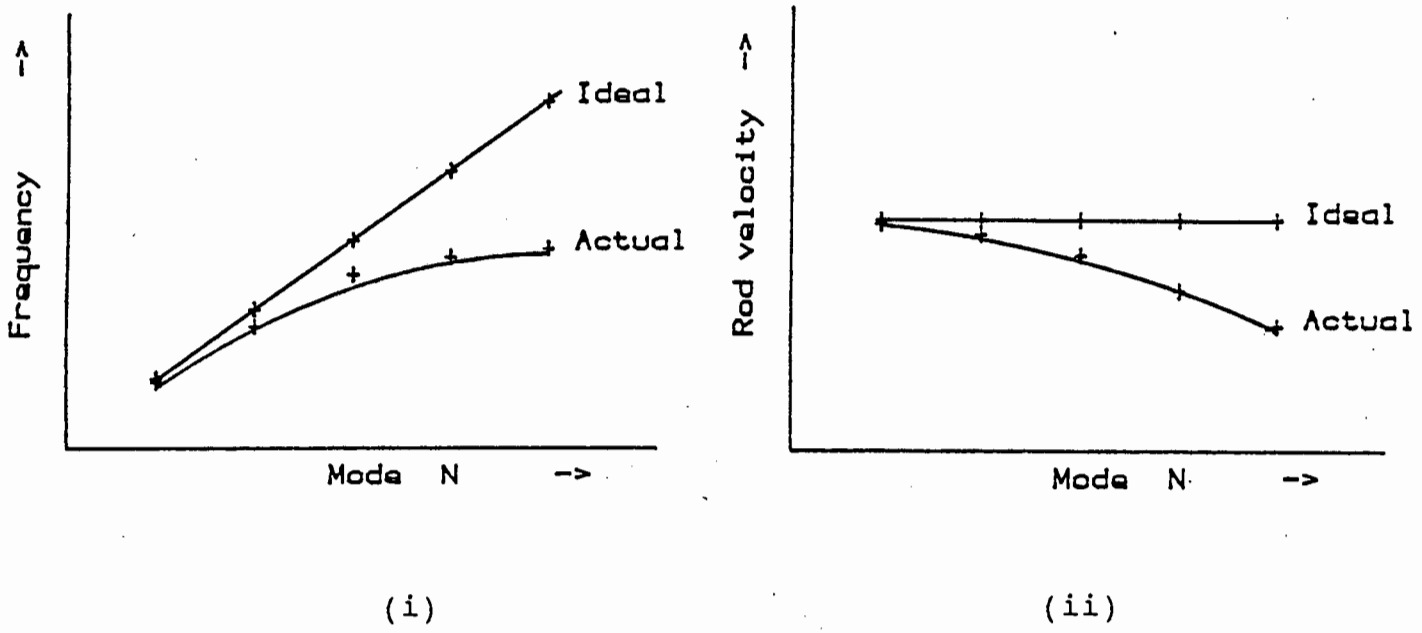

(i) (ii)

Figure 2.10: Dispersive curves of longitudinal vibrations of rods

Poisson's ratio and the longitudinal velocity c_o for a material are determined by applying a correction scheme based on the use of Bancroft's table to the resonance spectrum of a rod of the material of known dimensions. This is illustrated by way of an example where a rod of poco-graphite (an isotropic material) is characterised from its longitudinal resonance spectrum. For every resonant frequency f_n, the actual velocity c_n and the ratio λ_n/D are calculated. These values and an arbitrary value of Poisson's ratio are then used to calculate the longitudinal velocity c_o from Bancroft's table. Thus, for every value of f_n (or λ_n/D) and σ, a corresponding value for the longitudinal velocity c_o is obtained. Figure 2.11 shows a plot of c_o versus mode number n for three different values of Poisson's ratio. The correct Poisson's ratio is the one which yields consistent values for the rod velocity c_o. In this case, a Poisson's ratio of 0.25 is the correct value for poco-graphite.

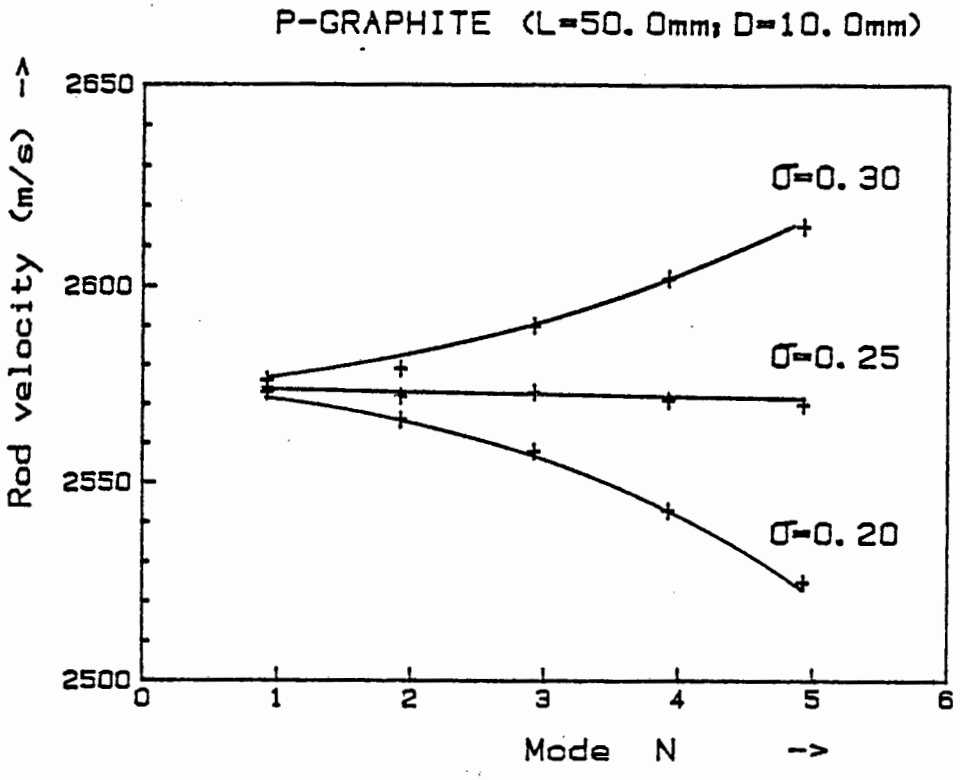

Figure 2.11: Graphical representation of Bancroft's correction scheme for determining the longitudinal velocity c_o and Poisson's ratio σ of a poco-graphite rod.

Young's modulus for poco-graphite is then calculated from the density of the material and its longitudinal velocity c_o as determined from the Bancroft's correction method by the following equation:

$$E = c_o^2 . p \quad \ldots\ldots\ldots\ldots\ldots\ldots \quad (2.5)$$

Thus, the elastic constants of poco-graphite determined from the longitudinal resonance spectrum of a rod 50.0 mm long and 10.0 mm diameter are:

Poisson's ratio, $\sigma = 0.25$
Longitudinal velocity, $c_o = 2570$ m/s
Density, $p = 1760$ kg/m^3
Young's Modulus, $E = 1.16 \times 10^{10}$ N/m^2

The five other rods are characterised in the same way and the results are tabulated in Table 2.4 at the end of this chapter.

In the case of thin disks, the thickness-mode resonance spectra can only be used to determine the bulk velocity of sound in the materials. The Bulk modulus is then calculated by substituting c_o by c_B in equation (2.5). Poisson's ratio, however, cannot be evaluated from the data. The elastic properties of the six epoxies and plastics used are also tabulated in Table 2.4.

2.4 Flexural vibrations of thin disks

2.4.1 Theory

A mathematical analysis of flexural vibrations in thin disks is given in [9] and numerical solutions to the transcendental frequency equations are computed by Leissa [15] for various boundary conditions. In this section, the important equations are presented for the case of a completely free disk and the computed roots to the corresponding frequency equation are tabulated.

The general wave equation describing transverse vibrations in a circular plate is:

$$\nabla^4 u + [\, 12p(1-\sigma^2)/(Et^2) \,].\delta^2u/\delta t^2 = 0 \quad \ldots\ldots\ldots \quad (2.6)$$

where $u = u(x,y,t)$ is the transverse displacement of a particle from its equilibrium position

E: Young's modulus

t: Plate thickness

p: Density of plate

σ: Poisson's ratio

It is assumed that $u(x,y,t)$ is periodic in time and that the period of any one particle is independent of its position (x,y). Therefore,

$$u(x,y,t) = u(x,y).\sin wt \quad \ldots\ldots\ldots\ldots\ldots\ldots (2.7)$$

Changing from Cartesian to polar coordinates and assuming that the displacement of particles with respect to θ is sinusoidal,

the new expression for u becomes:

$$u(x,y)\sin wt \equiv u(r,\theta)\sin wt = u(r)\sin(n\theta)\sin wt \quad ....(2.8)$$
$$; \; n = 0,1,2,...$$

In this equation, n represents the number of nodal diameters on the surface of the disk.

By substituting the new expression for u in the wave equation (2.6) and replacing the Laplacian operator by its polar equivalent, the general solution is given as:

$$u_n(r,\theta,t) = [A_nJ_n(kr) + B_nI_n(kr)]\sin(n\theta)\sin(wt) \quad .....(2.9)$$
$$; \; n=0,1,2,...$$

where $$k = [\ 12p(1-\sigma^2)w^2/(Et^2)\ ]^{1/4} \quad .....(2.10)$$

and J_n and I_n are the Bessel and modified Bessel functions of the first kind respectively and n is the order set by the number of nodal diameters. Thus, for every value of n, there exists a general solution u_n.

The frequency equation for the flexural vibrations of a free disk is obtained by applying the boundary conditions to the general solution of (2.9). This operation yields the following transcendental frequency equation:

$$\frac{\lambda^2J_n(\lambda)+(1-\sigma)[\lambda J_n'(\lambda)-n^2J_n(\lambda)]}{\lambda^2I_n(\lambda)-(1-\sigma)[\lambda I_n'(\lambda)-n^2I_n(\lambda)]} = \frac{\lambda^3I_n'(\lambda)+(1-\sigma)n^2[\lambda J_n'(\lambda)-J_n(\lambda)]}{\lambda^3I_n'(\lambda)-(1-\sigma)n^2[\lambda I_n'(\lambda)-I_n(\lambda)]}$$
$$; \; n = 0,1,2,..... \quad (2.11)$$

where

$$\lambda = kD/2 = [\ 12p(1-\sigma^2)w^2/(Et^2)\ ]^{1/4}.D/2 \quad .....(2.12)$$

The above equation contains Poisson's ratio σ and n, the number of nodal diameters. To determine values of λ which satisfy the above equation, a value must first be assigned to σ and n respectively. Then, values of λ which satisfy the frequency equation are computed numerically. For every value of σ and n, there exists an infinite number of solutions, the m^{th} solution,

λ_{mn}, corresponding to the resonance mode containing m nodal circles and n nodal diameters. Since λ is a function of w as seen from equation (2.12), the frequencies of the various resonant modes can be calculated from the roots λ_{mn}.

Values of λ_{mn} which satisfy the frequency equation (2.12) have been computed numerically by Leissa [15] for σ=0.33 and n ranging from 0 to 6. These are tabulated below:

m	λ^2 for values of n of—						
	0	1	2	3	4	5	6
0	----------	----------	5. 253	12. 23	• 21. 6	• 33. 1	• 46. 2
1	9. 084	20. 52	35. 25	52. 91	• 73. 1	• 95. 8	• 121. 0
2	38. 55	59. 86	83. 9	111. 3	142. 8	175. 0	210. 3
3	87. 80	119. 0	154. 0	192. 1	232. 3	274. 6	319. 7
4	157. 0	198. 2	242. 7	290. 7	340. 4	392. 4	447. 3
5	245. 9	296. 9	350. 8	408. 4	467. 9	529. 5	593. 9
6	354. 6	415. 3	479. 2	546. 2	615. 0	686. 4	760. 1
7	483. 1	651. 8	627. 0	703. 3	781. 8	864. 4	952. 3
8	631. 0	711. 3	794. 7	880. 3	968. 5	1061	1158. 7
9	798. 6	888. 6	981. 6	1076	1175	1277	1384
10	986. 0	1086	1188	1292	1401	1513	1631

Table 2.3: Values of λ^2 for a completely free circular plate with σ = 0.33.

2.4.2 Experimental results

The flexural resonance spectra of six disks of various dimensions made of aluminium, stainless steel, titanium, fused quartz and perspex are determined by the pulse-echo technique as described in section 2.2.1 and illustrated in Figure 2.4. The drive technique used to excite flexural vibrations in thin disks is illustrated schematically in Figure 2.5.

To identify a particular mode in the flexural resonance spectrum of a disk, use is made of the λ^2 values tabulated in Table 2.3. Equation (2.12), which expresses λ in terms of w and other physical parameters of the disk, can be rewritten as:

$$\lambda^2 = (\sqrt{12}).D^2w/(4c_pt) \quad \ldots\ldots\ldots\ldots\ldots\ldots\ldots\ldots(2.13)$$

where

$$c_p = [\ E/p(1-\sigma^2)\ ]^{1/2}$$

Therefore,

$$\lambda^2/w = (\sqrt{12}).D^2/4c_pt$$

or

$$\lambda^2/f = \pi(\sqrt{12}).D^2/2c_pt \quad \ldots\ldots\ldots\ldots\ldots\ldots\ldots\ldots(2.14)$$

The right hand side of eq (2.14) above is constant for a particular disk, i.e.

$$\lambda_{mn}^2/f_{mn} = \text{constant} \quad \ldots\ldots\ldots\ldots\ldots\ldots\ldots\ldots(2.15)$$

Thus, for any resonance mode (m,n) of a given disk, the ratio λ_{mn}^2/f_{mn} yields a constant value. This feature is used to identify the various modes that are observed experimentally. If a mode is incorrectly identified, the resulting λ^2/f ratio will not be consistent with the other ratios. Conversely, if the mode is correctly identified, then a constant λ^2/f ratio will be obtained.

The flexural resonances of six disks are determined over a limited frequency range and identified by the technique described above. These are displayed graphically in Figure 2.12. Note that the modes have been classified in three groups: the first one consists of those modes with nodal diameters only, i.e. the (0,n) modes; the second group consists of modes with nodal circles only, i.e. the (m,0) modes; and the third group contains those modes that are characterised by both nodal circles and nodal diameters, i.e. the (m,n) modes. The diameter to thickness ratios of the disks vary considerably with the fused quartz disk having a ratio of ≈25 and the one aluminium disk, a ratio of ≈3.5. Consequently, the frequency ranges covered by the resonance spectra of the various disks also vary as seen from the graphs of Figure 2.12.

A distinguishing feature of flexural vibrations in thin disks is the relatively low frequency range within which their resonance spectra lie when compared to thickness-mode vibrations. Furthermore, a reduction in the thickness of a disk

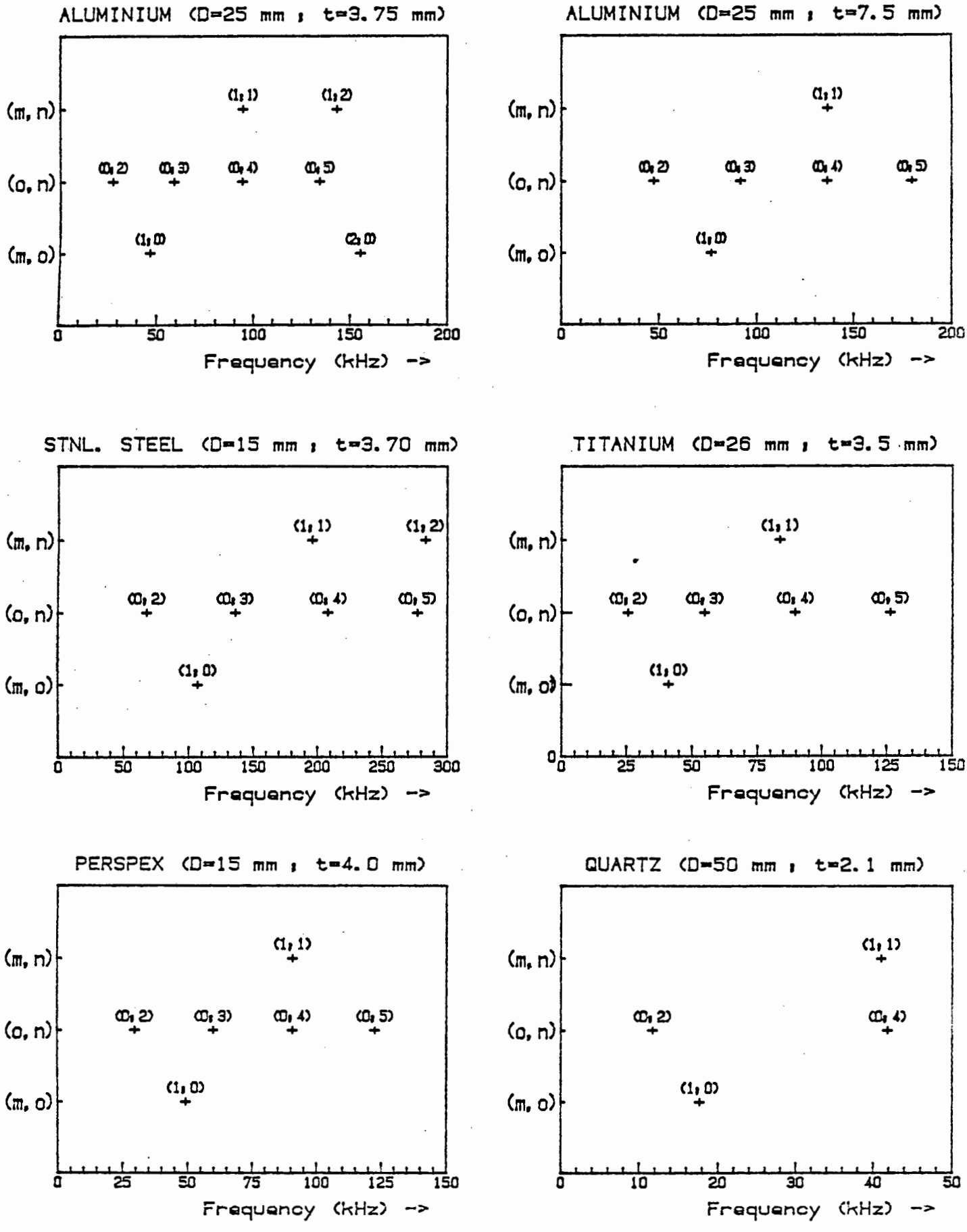

Figure 2.12: Flexural resonance spectra of six disks of various materials determined experimentally by the pulse-echo technique .

results in its flexural resonance spectrum being shifted down in frequency while its thickness-mode spectrum is shifted up. Thus, interaction between flexural and thickness-mode vibrations does not generally occur in thin disks. However, in the case of thick disks, there is a possibility of there being interaction between the two modes.

The relative positions of the various modes of flexural vibrations of a disk are a function of the geometry of the disk and the elastic properties of the material. In some cases, two modes may coincide in frequency as shown by the (1,1) and (0.4) modes of the aluminiun disks in Figure 2.12. Note also that the first two modes in all six spectra are the (0,2) and (1,0) modes. The positions of these two modes relative to each other can be used to determine the elastic properties of the material of a disk, as described in the following section.

2.4.3 Material characterisation using flexural resonance spectrum

Poisson's ratio and Young's modulus for a material can be determined from the first two flexural resonances of a free disk of the material by a method developed by Martincek [17]. Nomograms relating Poisson's ratio to the ratio of the first two frequencies, f_{10}/f_{02}, for t/R values ranging from 0.0 to 1.0 are reproduced in Appendix A2. Young's modulus for the material is then calculated using the frequency of the (1,0) mode in the following equation:

$$E = (4\pi^2 f_{10}^2 R^2 p) / \bar{w}^2 \quad \ldots\ldots\ldots\ldots (2.16)$$

where

R : Radius of disk

p : Density of material

f_{10} : Frequency of (1,0) mode

and $\bar{w}$ is a function of two variables, namely Poisson's ratio and t/R ratio, which is evaluated by interpolation from Table A2 in Appendix A2.

The advantage of this method lies in the fact that only the first two resonance modes are required for calculating the elastic constants of a material.

To illustrate the use of this technique, the elastic constants of an aluminium disk of diameter 25.1 mm and thickness 3.75 mm are evaluated using the following experimental data:

$$f_{02} = 27.6 \text{ kHz}$$
$$f_{10} = 47.0 \text{ kHz}$$
$$p = 2700 \text{ kg/m}^3$$
$$t/R = 0.30$$

Therefore,

$$f_{10}/f_{02} = 1.70$$

The above ratio is used to determine Poisson's ratio from the nomograms of Appendix A2. Thus,

$$\text{Poisson's ratio, } \sigma = 0.35$$

By interpolation from Table A2 in Appendix A2, a value for $\bar{w}$ is obtained as

$$\bar{w} = 0.73$$

Young's modulus for aluminium is then calculated by substitution in equation (2.16). Thus,

$$\text{Young's modulus, } E = 6.9 \times 10^{10} \quad \text{N/m}^2$$

The same method is used to characterise the other materials used for studying flexural vibrations.The results are tabulated in Table 2.4 alongside those obtained from the longitudinal resonance spectra of rods of the same materials. Note that if a material is anisotropic, the elastic constants will be different for each method. Conversely, an isotropic material will produce consistent results with both methods.

2.5 In-Plane Vibrations of Disks

2.5.1 Theory

The theory of in-plane vibrations of disks is studied by Love [9] who derives frequency equations for the three classes of vibrations, namely radial, torsional and compound modes. This section outlines the important equations and presents a table of solutions to the transcendental frequency equations for radial and compound modes computed by Chaplain [16].

The wave equations governing the in-plane motion of particles in a disk are given by:

$$\delta T_1/\delta x + \delta S_1/\delta y = 2pt\ \delta^2 u/\delta t^2$$
$$\delta S_1/\delta x + \delta T_2/\delta y = 2pt\ \delta^2 v/\delta t^2 \qquad \ldots\ldots\ldots (2.17)$$

where T_1, T_2 and S_1 are the stress resultants given by the approximate formulae

$$T_1 = 2Et/(1-\sigma^2)\ .\ (\ \delta u/\delta x + \sigma\ \delta v/\delta y\ )$$

$$T_2 = 2Et/(1-\sigma^2)\ .\ (\ \delta v/\delta y + \sigma\ \delta u/\delta x\ )$$

$$S_1 = Et/(1+\sigma)\ .\ (\ \delta u/\delta y + \delta v/\delta x\ )$$

and

E : Young's modulus
σ : Poisson's ratio
p : Density
t : Thickness of disk

and u=u(x,y,t) and v=v(x,y,t) are the components of displacement in cartesian coordinates (x,y) and time t.

The wave equations above are solved by introducing new components of displacement and the three frequency equations for radial, torsional and compound modes are obtained by considering the presence of the radial and rotational components of motion in the various modes of vibration.

Radial modes

These are characterised by particles having no rotational motion. Thus, the frequency equation is given as:

$$\frac{d}{dR} J_1(K) + \frac{\sigma}{R} J_1(K) = 0 \quad \ldots\ldots\ldots\ldots\ldots \quad (2.18)$$

where $K = wR\,[p(1-\sigma^2)/E]^{1/2}$

w : Angular velocity

R : Radius of disk

There is an infinite number of solutions to eq (2.18), the n^{th} solution K_{nR} corresponding to the resonance mode which has n nodal circles, the (n,R) mode. Chaplain [16] computed the roots of the frequency equation for σ ranging from 0 to 0.5 and n equal to 1 and 2. These are listed in Table A3.1, Appendix A3.

Compound modes

These are characterised by the presence of both rotational and radial components of motion. The frequency equation for this case is:

$$\frac{n\,[\,M_n(\Theta K)-(n+1)\,]}{(K\Theta)^2/2 - n(n+1) + M_n(K)} = \frac{2M_n(\Theta K)+ (K\Theta)^2 - 2n(n+1)}{2n\,[\,M_n(K) - (n+1)\,]} \quad \ldots(2.19)$$

where $K = wR\,[\,p(1-\sigma^2)/E\,]^{1/2}$ $\ldots\ldots\ldots\ldots\ldots\ldots$ (2.20)

$\Theta = [\,2/(1-\sigma)\,]^{1/2}$

$M_n(\alpha) = \alpha\, J_{n-1}(\alpha)/J_n(\alpha)$

For a given σ and n, the roots K of the above equation are computed numerically, the m^{th} root K_{mn} corresponding to the mode with m nodal circles and n nodal diameters, the (m,n) mode. Table A3.1 lists the values of K_{mn} which satisfy equation (2.19) for σ ranging from 0 to 0.5 and n ranging from 1 to 10.

The frequencies at which the various resonance modes occur can be calculated from the K_{mn} values and eq (2.20) which relates K to w.

2.5.2 Experimental Results

In- plane vibrations of thin disks are particularly important to the study of piezoelectric transducers because of the ability of some of their modes to couple piezoelectrically. To demonstrate this, a very simple experiment is devised where a PZT5A disk is mechanically excited in its in-plane modes by the acoustic transmission line technique of Figure 2.4. The piezoelectric coupling of each mode is then tested by observing the electrical voltage developed across the transducer. If a particular mode couples piezoelectrically, a voltage will develop across the terminals of the transducer.

The piezoelectric coupling of the "breathing" or (1,R) mode is demonstrated by the photograph of Figure 2.11 which shows two traces on an oscilloscope screen.

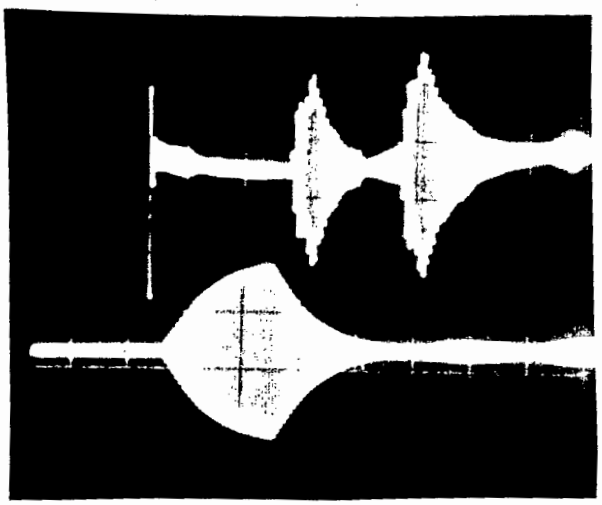

Figure 2.13: Photograph showing the mechanical and electrical coupling of the (1,R) mode of a PZT5A disk. The top trace shows the mechanical driving burst and echo and the bottom trace, the electrical voltage across the transducer. These traces indicate a condition of mechanical resonance accompanied by piezoelectric coupling.

The top trace is that which is obtained from the magnetostrictive transmitter/receiver. The first burst to the left is the driving burst and the one to the right constitutes the echo with its distinctive features of mechanical resonance. The bottom trace shows the voltage developed across the transducer as a result of the piezoelectric coupling.

A further investigation of the in-plane resonance spectra of thin disks is carried out by exciting four disks of different materials and dimensions by the acoustic transmission line technique of Figure 2.4, with the end of the wire placed radially at the periphery of the disk. The materials used are aluminium, stainless steel, titanium and fused quartz.

Mode identification is achieved by a method similar to that used for flexural vibrations. By rewriting equation (2.20) in the following form:

$$K/w = R\,(p(1-\sigma^2)/E)^{1/2} = \text{constant}$$

a ratio is obtained which is constant for all the radial and compound modes of a particular disk, i.e.,

$$K_{mn}/f_{mn} = \text{constant for all } m,n$$

Thus, if a given resonance is correctly identified, the corresponding K/f ratio will be consistent with those of the other identified modes.

The in-plane resonance spectra of the four disks mentioned above are identified and displayed graphically in Figure 2.14. The (1,R) or "breathing" mode is plotted on a separate line as shown to emphasize its position relative to the other modes. For most materials, it occurs between the (1,1) and (1,3) modes. The different scales used on the frequency axis are accounted for by the variation in the dimensions of the disks. A disk of small diameter will have its resonances at higher frequencies than a larger diameter disk. The spectra of the aluminium and steel disks illustrate this property.

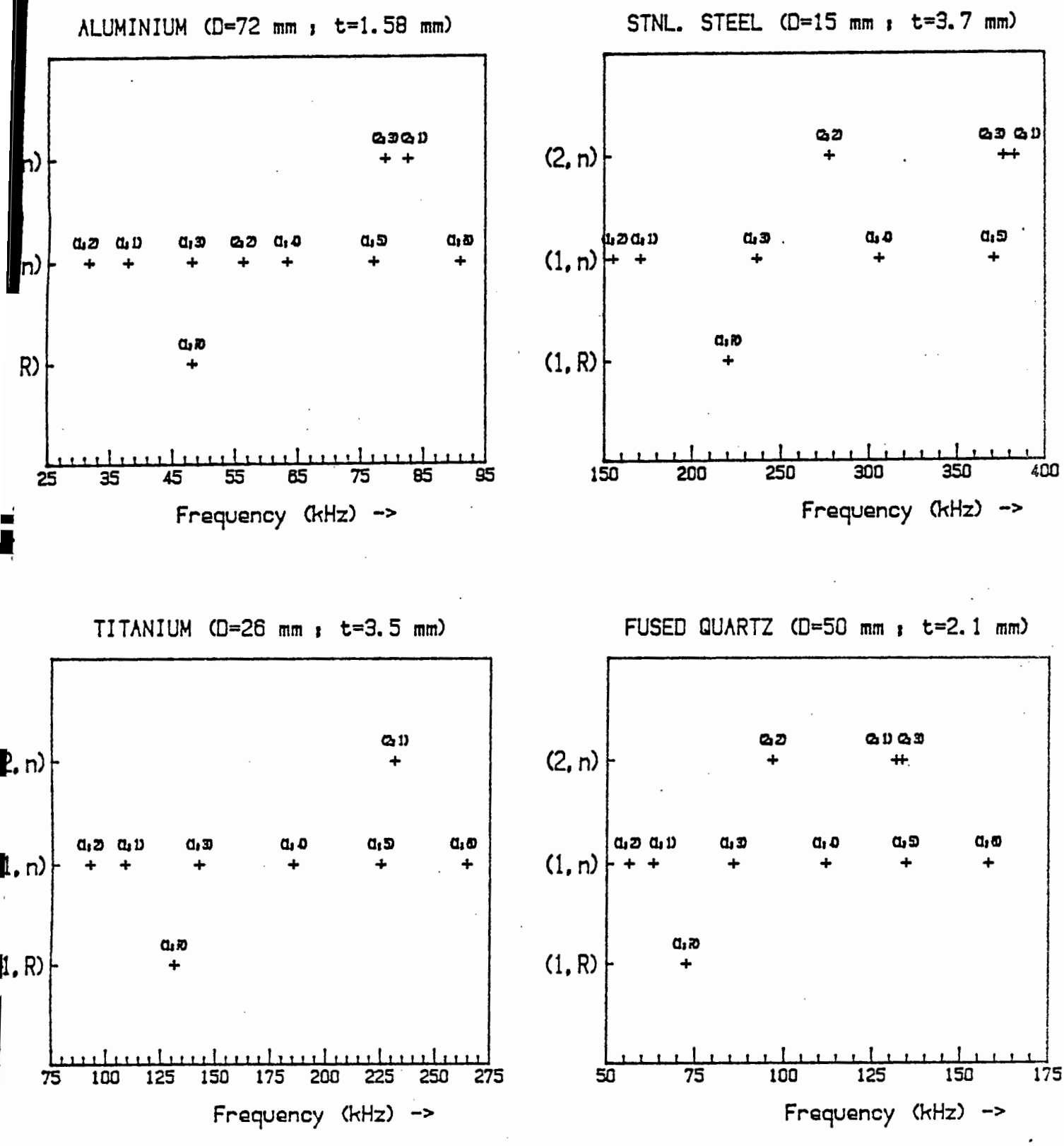

Figure 2.14: In-plane resonance spectra of four disks of various materials. The (1,R) or "breathing" mode is plotted on a seperate line to emphasize its position as it is the only one which exhibits piezoelectric coupling.

The elastic constants of the four materials used can be calculated from their in-plane resonance spectra. The next section describes a method for calculating Young's modulus and Poisson's ratio for a material from the frequencies of certain in-plane modes of a disk of the material of known dimensions.

2.5.3 Material characterisation using the in-plane resonance spectrum

Young's modulus and Poisson's ratio for a material can be determined experimentally from the in-plane resonance spectrum of a thin disk of the material of known dimensions. Certain modes of in-plane vibrations exhibit different dependencies on Poisson's ratio to other modes. This is illustrated graphically in Figure 2.15 where the K values for compound and radial modes are plotted as functions of Poisson's ratio. Clearly, the (1,R), (2,1) and (2,R) modes behave differently to the others with respect to σ, and thus, by looking at the ratio of the K values of these modes to the K values of the others, Poisson's ratio can be determined.

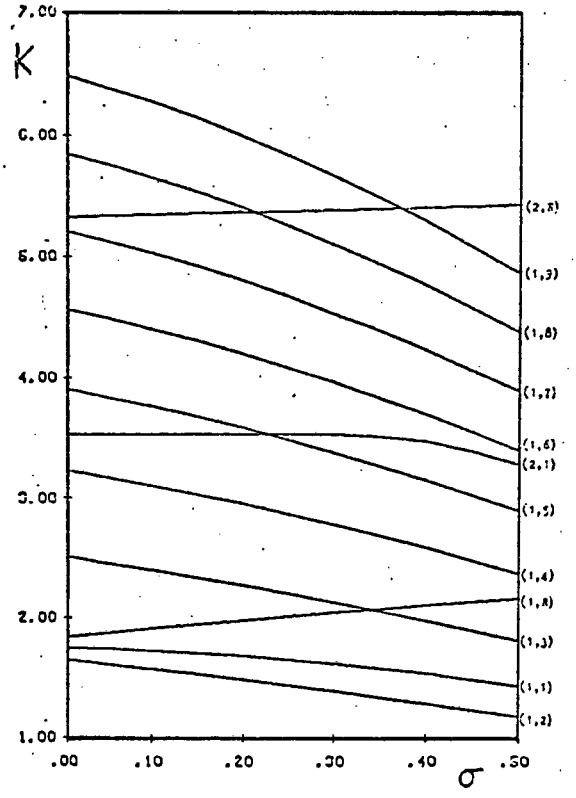

Figure 2.15: Graph showing variation of K-values with σ. The (1,R), (2,1) and (2,R) modes behave differently to the other modes.

in Figure 2.14. The results are then tabulated in the next section together with those obtained using longitudinal and flexural resonance spectra.

2.6 Experimental data on various materials

The elastic constants of the various materials used in the study of disk and rod vibrations have been calculated by a number of different techniques, each technique using the resonance spectrum of a different mode of disk or rod vibration. Table 2.4 lists the experimental data obtained for these materials. In some cases where a material has been characterised by more than one method, e.g. aluminium, the isotropic nature of the material can be verified by checking whether the values obtained for a constant by different methods are consistent with one another. Aluminium and stainless steel prove to be reasonably isotropic while titanium does not.

The acoustic impedances of the materials have also been calculated as they constitute an important parameter in ultrasonic transducer design. The epoxies and resins are characterised by approximately the same values for acoustic impedance as seen from Table 2.4.

Material	Density (p) kg/m^3	Young's Mod. (E) $x10^{10}$ N/m^2			Poisson's ratio (σ)			Acst. Imp $Z=(Ep)^{1/2}$ $x10^6$ Pas/m
		(i)*	(ii)	(iii)	(i)*	(ii)	(iii)	
Aluminium	2700	7.14	6.90	6.70	0.33	0.35	0.34	13.7
Stainless Steel	7720	18.8	19.4	19.0	0.27	0.28	0.28	38.3
Titanium	4540	11.0	12.2	12.2	0.33	0.27	0.27	22.8
P-graphite	1760	1.16			0.25			4.52
Bill. ball	1770	0.60			0.40			3.25
Perspex	1150	0.56	0.50		0.30	0.36		2.54
Fused Quartz	2150		10.6	7.70		0.17	0.16	15.1
M-Resin	1158	0.48						2.36
Polyester Resin FB366	1187	0.69						2.87
Casting Resin FB9007	1179	0.65						2.76
Epoxy FB 816	1164	0.63						2.70
PVC	1400	0.64						3.00

Table 2.4: Elastic constants of various materials determined experimentally by three different methods.

* (i): Longitudinal resonance spectrum
(ii): Flexural resonance spectrum
(iii): In-Plane resonance spectrum

CHAPTER 3

RADIATION CHARACTERISTICS OF THICKNESS MODE TRANSDUCERS

3.1 Introduction

The radiation characteristics of thickness-mode ultrasonic transducers are analysed firstly in terms of the radiation impedance of the loading medium and, secondly, in terms of the beam characteristics of the transducer. Radiation impedance is that parameter which is representative of the energy that is transferred from the transducer to the medium and is therefore a measure of the acoustic coupling between the transducer and the medium. The beam characteristics on the other hand describe the physical features of the beam of ultrasound generated by the transducer. The extent of the near-field and the directionality of the beam are two examples of beam characteristics.

Both the radiation impedance and the beam characteristics of a transducer are related to the ratio of the diameter of the radiating surface of the transducer to the wavelength of the acoustic wave in the medium, i.e. the D/λ ratio. Analytical relationships are derived theoretically for the simple case of a circular piston vibrating in a fluid [13]. It is found that radiation impedance has both a resistive and a reactive component, the magnitudes of which depend on the D/λ ratio of the transducer. Similarly, the extent of the near-field and the beamwidth of a transducer are direct functions of the D/λ ratio.

Transducer geometry is therefore an important consideration when designing transducers for a particular application. Depending on the constraints imposed on the transducer, the appropriate D/λ ratio must be selected. In broadband applications, strong coupling between the transducer and the loading medium is the main design criterion. In other applications, high directionality may be desirable. After identifying the operational requirements of the transducer, its

dimensions are chosen so as to give the appropriate D/λ ratio over the frequency range concerned.

A study of radiation impedance as a function of D/λ is carried out over two ranges of frequencies. The first range extends from 37 kHz to 92 kHz with the D/λ ratio varying between 0.30 and 0.76. This is implemented by the use of composite thickness-mode transducers operating in water. The second frequency range is centered around 2 MHz, extending over a 1 MHz interval. In this case, the D/λ ratio varies between 7 and 53. Four PZT disks of various diameters operating in water are used for this purpose. The resistive and reactive components of radiation impedance are evaluated by obtaining admittance circle diagrams for each transducer operating in air (considered to be a vacuum) and in water. These are then plotted against D/λ and the trends are compared with theory.

The beam characteristics of thickness-mode transducers are analysed qualitatively in terms of their diameter to wavelength ratios. Four PZT5A disks of resonant frequency 2 MHz and diameters varying between 5 and 40 mm are excited in pulse-echo mode and their beam patterns are determined by recording the echo amplitudes for different transducer-reflector distances. A plot of echo amplitude versus reflector position gives a picture of the beam profile that is generated by the transducer. The directionality of the beam can also be inferred qualitatively from the plot.

3.2 Radiation Impedance as a function of D/λ

3.2.1 Theory

The radiation impedance of a fluid acting on a transducer is derived theoretically by Morse [10] for the case of a baffled circular piston radiating in a fluid of density p and sound velocity c. This section outlines the important equations and presents theoretical plots of the resistive and reactive components of radiation impedance.

A general expression for the radiation impedance Z_{rad} of a fluid is given as:

$$Z_{rad} = R_{rad} + j\, X_{rad} \quad \ldots\ldots\ldots\ldots\ldots\ldots \quad (3.1)$$

where R_{rad} and X_{rad} are the radiation resistance and reactance respectively. A positive X_{rad} indicates an inductive or mass loading, while a negative one indicates a capacitive or stiffness loading. In the case of a thickness-mode transducer, the surrounding medium always contributes mass loasing and, thus, X_{rad} is positive.

The theoretical equations obtained for R_{rad} and X_{rad} for the case of a baffled circular piston of diameter D are expressed in terms of the D/λ ratio as follows:

$$R_{rad} = \pi(D/2)^2 pc \;.\; R_1(2\pi D/\lambda) \quad \ldots\ldots\ldots\ldots \quad (3.2)$$

$$X_{rad} = \pi(D/2)^2 pc \;.\; X_1(2\pi D/\lambda) \quad \ldots\ldots\ldots\ldots \quad (3.3)$$

where $R_1(x) = 1 - 2J_1(x)/x$

and $X_1(x) = (4/\pi).[\, x/3 - x^3/(3^2.5) + x^5/(3^2.5^2.7)\ldots]$

Equations (3.2) and (3.3) can be rewritten as:

$$R_{rad} = k.R_1(2\pi D/\lambda) \quad \ldots\ldots\ldots\ldots\ldots\ldots \quad (3.4)$$

$$X_{rad} = k.X_1(2\pi D/\lambda) \quad \ldots\ldots\ldots\ldots\ldots\ldots \quad (3.5)$$

where k is a constant whose value depends on the diameter D of the transducer and the acoustic impedance pc of the fluid.

R_{rad} and X_{rad} are plotted against $2\pi D/\lambda$ for the case k=1 as shown in Figure 3.1 below. Note that the independent variable $2\pi D/\lambda$ is proportional to the D/λ ratio.

The R_{rad} curve indicates that the resistive component of radiation impedance reaches a steady value as D/λ increases to infinity, while the reactive component vanishes to zero. This means that for a piston where the radiating surface is large compared to the wavelength being generated, the reactive component is negligible and the radiation impedance is purely resistive. Furthermore, for values of $2\pi D/\lambda$ lower than 2.5, the reactive component is larger than the resistive component

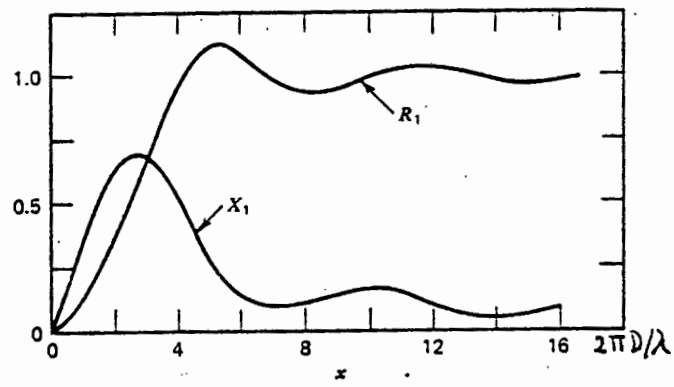

Figure 3.1: Resistive and Reactive components of the radiation impedance of a circular piston plotted as functions of $2\pi D/\lambda$.

and reaches a peak at $2\pi D/\lambda = 2.5$ (or $D/\lambda = 0.4$). Above this value, the resistive component becomes more significant with a maximum at $2\pi D/\lambda = 5$ (or $D/\lambda = 0.8$).

To illustrate the importance of the above curves, consider the case where a transducer must be designed to be frequency stable when operating in a variety of fluids, each fluid characterised by a different sound velocity c. To achieve frequency stability, it is necessary that the reactive component of radiation resistance is constant, irrespective of D/λ . From the X_{rad} curve of Figure 3.1, it is evident that this condition is satisfied for high values of D/λ . Thus, if a transducer is to exhibit frequency stability, its dimensions must be such that $2\pi D/\lambda > 12$ (or $D/\lambda > 2$) over the frequency range of interest.

If in another application, the transducer is to exhibit strong acoustic coupling to the loading medium, then the resistive component of radiation impedance must be maximised. From the R_{rad} curve of Figure 3.1, it is seen that $2\pi D/\lambda$ must be greater than 4, i.e. $D/\lambda > 1.3$. A transducer of lower D/λ ratio will be characterised by a lower radiation resistance and will consequently exhibit poorer coupling to the loading medium.

3.2.2 Experimental set-up: The Admittance Circle Plotter

The resistive and reactive components of the radiation impedance of a fluid acting on a transducer are determined by a technique which makes use of the admittance circle diagrams of the resonating transducer operating in air and in the fluid. A description of the technique is given in the next section. Here, the hardware used for drawing the admittance circle diagrams of a piezoelectric resonator operating in a given medium is described.

A block diagram of the system for obtaining admittance circle diagrams is given in Figure 3.2. The essential features of the system are described as follows:

(i) The admittance circle diagram plotter outputs two voltages proportional to the conductance G and susceptance B of the transducer under test as the frequency of the input signal to the plotter varies. The susceptance and conductance signals are then connected to the X and Y inputs of an XY-Plotter as shown to produce the admittance circle diagram of the transducer.

(ii) The oscillator provides a sinusoidal voltage at variable frequency and amplitude which is used as the input signal to the admittance circle diagram plotter. The digital frequency meter (DFM) measures the frequency of the signal.

(iii) An anechoic tank, into which the transducer under test is immersed, consists of a glass vessel whose sides and bottom are lined with foam. Any energy radiated in the tank is absorbed, thereby eliminating the formation of standing waves.

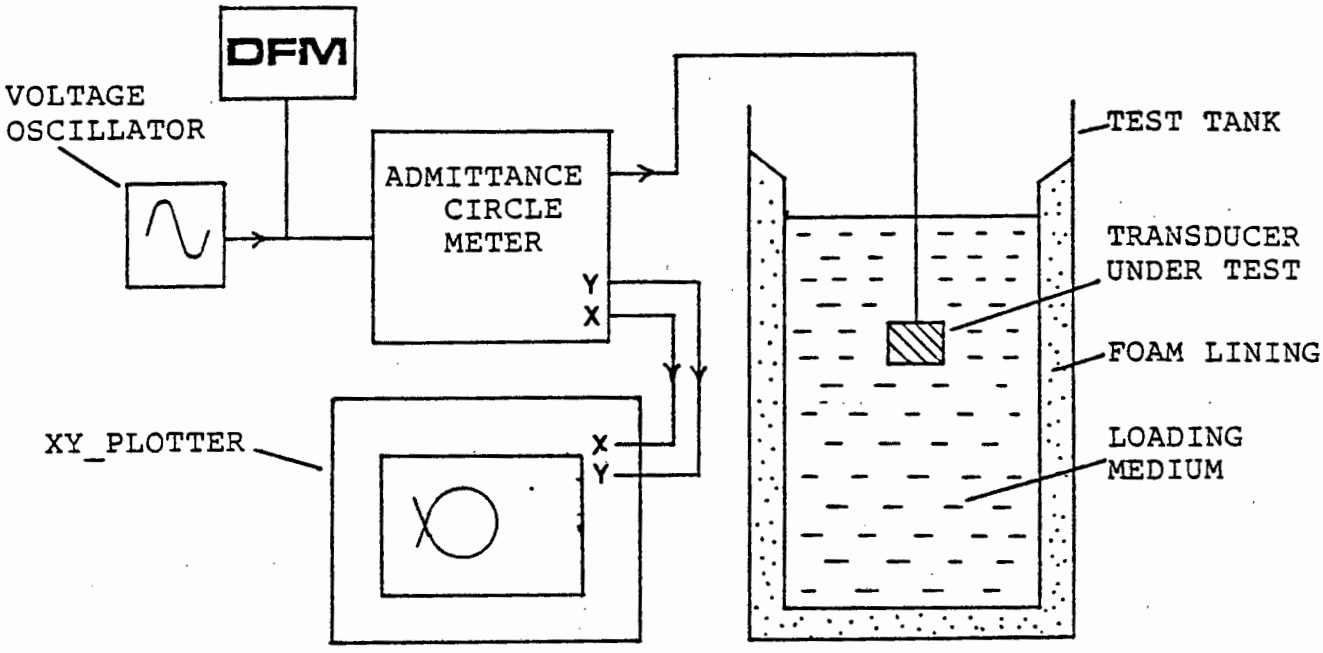

Figure 3.2: Schematic diagram of the Admittance Circle Diagram Plotter.

3.2.3 Evaluation of Radiation Impedance

The resistive and reactive components of the radiation impedance of a fluid acting on a transducer are evaluated by obtaining admittance circle diagrams of the transducer operating in air (considered to be a vacuum) and in the fluid. The simple electrical model for thickness-mode piezo-electric transducers is then used to derive expressions for the radiation resistance R_{rad} and radiation reactance X_{rad} in terms of measurable parameters on the admittance circle diagram.

The simple electrical model for a thickness-mode piezoelectric transducer operating in a vacuum is given in Figure 3.3 with its corresponding admittance circle diagram. In this model, the series RLC branch of the circuit represents the mechanical part of the transducer. R_l is the component which is responsible for energy dissipation both internally and as acoustic radiation.

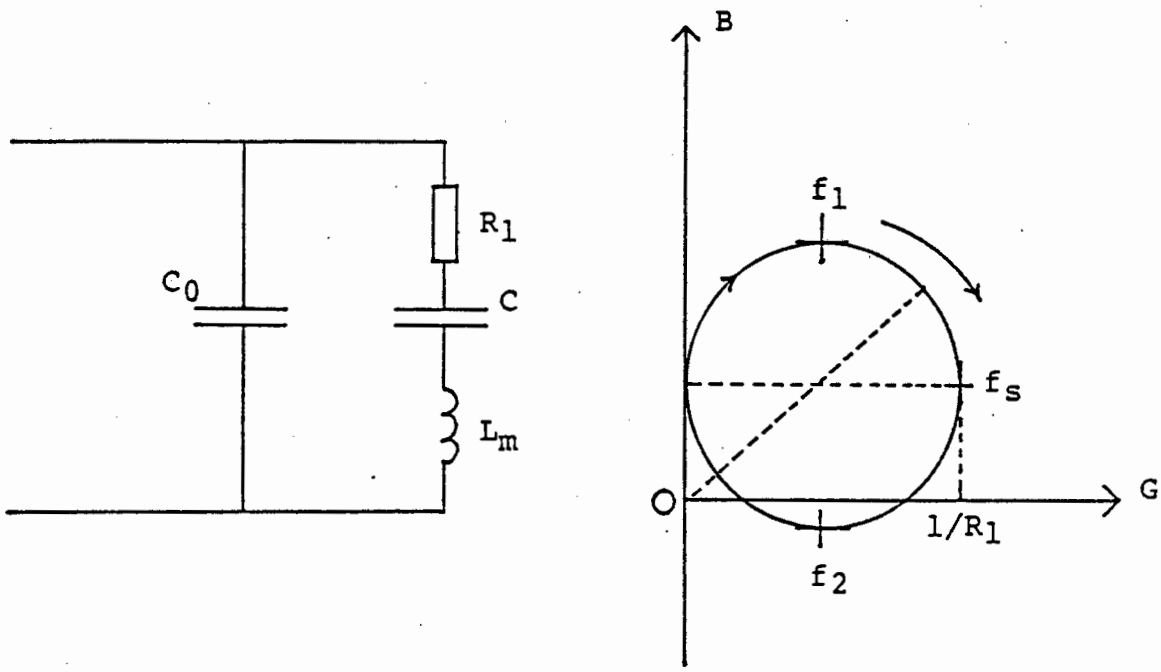

Figure 3.3: Equivalent electrical model of the thickness-mode piezoelectric transducer operating in a vacuum and its corresponding admittance circle diagram. R_1 represents the internal losses in the transducer.

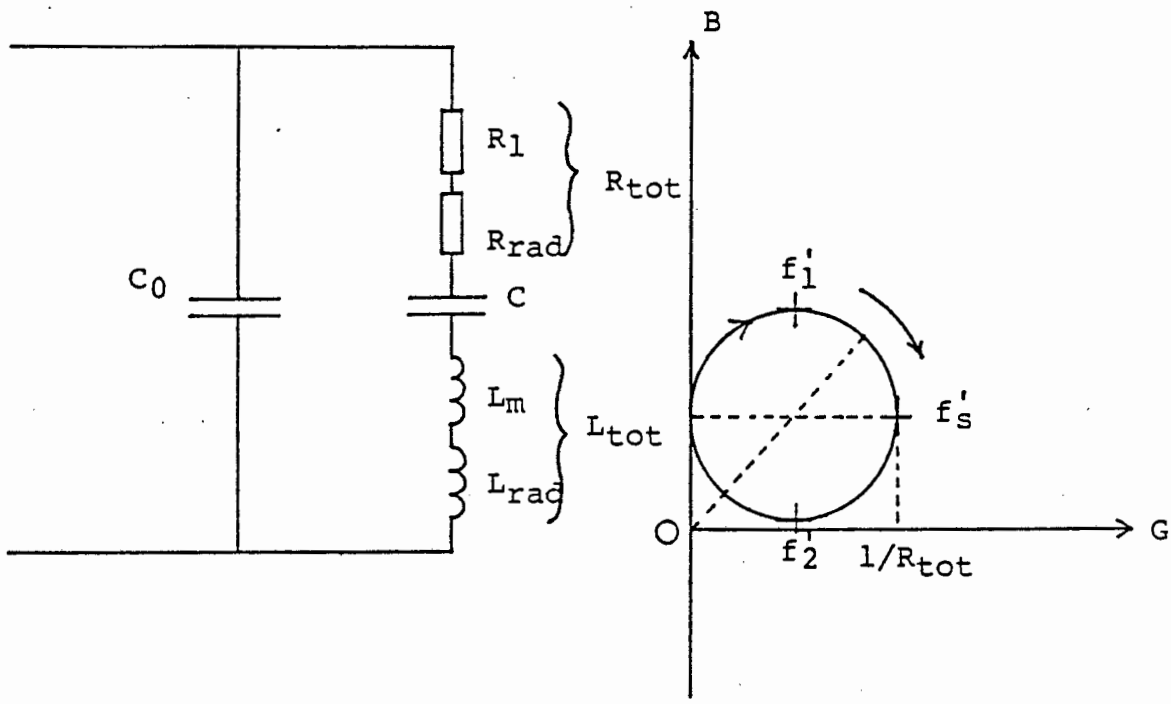

Figure 3.4: Equivalent circuit and admittance circle diagram of piezoelectric transducer vibrating in a fluid. R_{rad} and L_{rad} are the resistive and reactive components of the radiation impedance of the fluid acting on the transducer.

In a vacuum, however, no energy is radiated,and thus, R_l is due solely to internal losses within the transducer. L_m represents the equivalent mass of the vibrating system and C, the stiffness responsible for the restoring force in the system. C_o is the clamped static electrical capacitance of the piezoelectric transducer.

When the transducer is immersed in a fluid, the equivalent electrical model is modified as shown in Figure 3.4. The resistive and mass loading of the fluid, R_{rad} and L_{rad}, appear in the series RLC branch to produce a combined resistance R_{tot} and inductance L_{tot} so that,

$$R_{tot} = R_{rad} + R_l \quad \ldots\ldots\ldots\ldots\ldots\ldots \quad (3.6)$$

$$L_{tot} = L_{rad} + L_m \quad \ldots\ldots\ldots\ldots\ldots\ldots \quad (3.7)$$

The fluid does not contribute any stiffness loading and, thus, C remains unchanged.

The two equivalent circuits of Figures 3.3 & 3.4 have different series resonant frequencies owing to the mass loading of the fluid. Furthermore, their Q-factors also differ in that the model of Figure 3.4 has a lower Q due to the energy radiated in the fluid.

For the transducer model of Figure 3.3, the following equations apply:

$$f_s = 1/2\pi(L_m C)^{1/2} \quad \ldots\ldots\ldots\ldots\ldots\ldots \quad (3.8)$$

$$Q = f_s/(f_2-f_1) = 2\pi f_s L_m/R_l \quad \ldots\ldots\ldots \quad (3.9)$$

where f_s, f_1 and f_2 are the series resonant and half-power frequencies respectively obtained from the admittance circle diagram as shown. R_l is also obtained from the plot and represents the internal losses within the transducer.

From equation (3.9), an expression for L_m is derived. Thus,

$$L_m = R_l/2\pi(f_2-f_1) \quad \ldots\ldots\ldots\ldots\ldots\ldots \quad (3.10)$$

For the case of the transducer model of Figure 3.4 where the transducer radiates energy in a fluid, the series resonant frequency is expressed as:

$$f_s' = 1/2\pi(L_{tot}C)^{1/2} \quad \ldots\ldots\ldots\ldots\ldots\ldots \quad (3.11)$$

Substituting for C from equation (3.8) and rewriting the above equation;

$$L_{tot} = L_m \, (f_s/f_s')^2 \quad \ldots\ldots\ldots\ldots\ldots\ldots \quad (3.12)$$

Thus, the two components of radiation impedance can be calculated from the following expressions:

$$L_{rad} = L_{tot} - L_m = L_m \, [\, (f_s/f_s')^2 - 1 \,]$$

Substituting for L_m,

$$Lrad = R_1 \, [(f_s/f_s')^2 - 1]/ \, 2\pi(f_2-f_1) \ldots\ldots \quad (3.13)$$

$$R_{rad} = R_{tot} - R_1 \quad \ldots\ldots\ldots\ldots\ldots\ldots\ldots \quad (3.14)$$

To illustrate the use of this technique for evaluating R_{rad} and L_{rad}, an example is given where the radiation impedance of a composite transducer of resonant frequency 43.5 kHz in water is evaluated.

The admittance circle diagrams for the transducer operating in air and in water are given in Figure 3.5. From these, the following parameters are obtained:

In air: series resonant frequency, $f_s' = 46.72$ kHz
1^{st} 3-dB frequency, $f_1 = 46.51$ kHz
2^{nd} 3-dB frequency, $f_2 = 46.93$ kHz
Resistive component, $R_1 = 1/G_1 = 3.50$ kΩ

In water: series resonant frequency, $f_s' = 43.48$ kHz
Resistive component, $R_{tot} = 1/G_{tot} = 15.6$ kΩ

By substituting these values in equations (3.13) and (3.14),

the components of the radiation impedance of water acting on the transducer are evaluated. Thus,

$$R_{rad} = 12.1\ k\Omega$$
$$L_{rad} = 0.21\ H$$

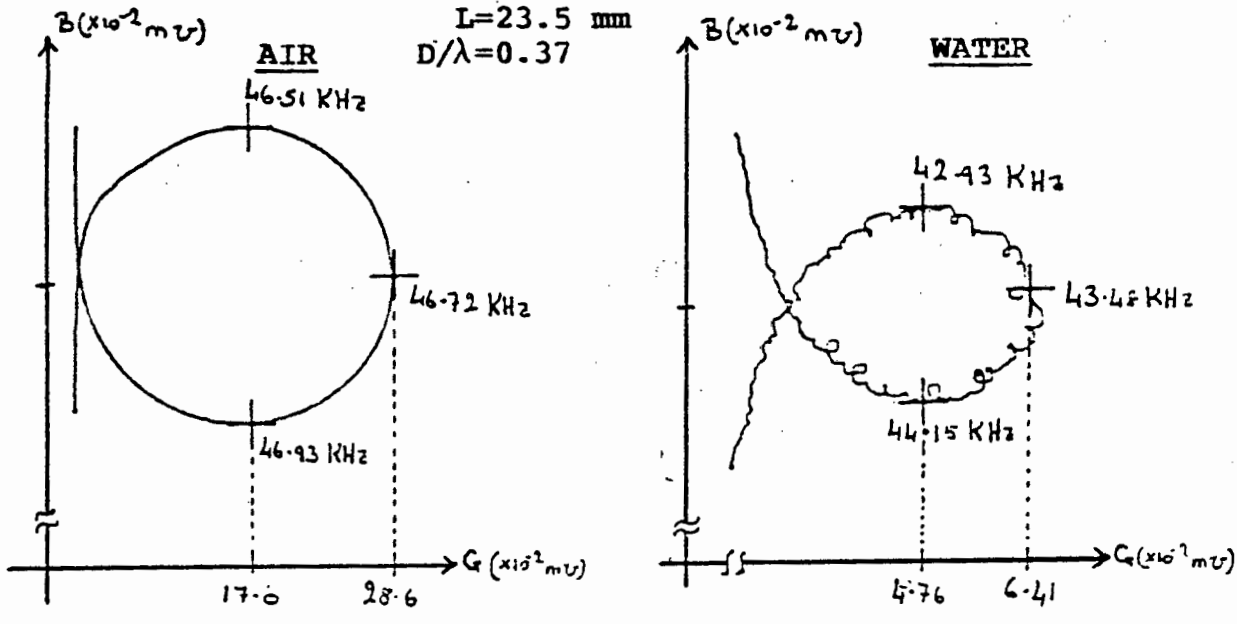

Figure 3.5: Admittance circle diagrams of composite transducer operating in air and in water. The jagged nature of the circle in water is due to the formation of standing waves in the medium.

3.2.4 Design and Construction of Transducers

To investigate the relationship between radiation impedance and the diameter to wavelength ratio of a transducer, two types of transducers are used. The first type covers a frequency range of 37 to 92 kHz while the second one extends in the megahertz region.

When designing the low frequency transducers, care is taken to ensure that the radiation impedance of the surrounding medium contributes substantially to the mechanical impedance of the transducer. To achieve this, it is necessary that the effective acoustic impedance of the transducer is of the same order as

that of the medium, so that the two are well matched, thereby making the radiation impedance Z_{rad} high. In order to implement this, the transducer is constructed in a way so as to make its effective density low. Since acoustic impedance is directly proportional to density, a lowering of the density of the transducer will result in the lowering of its acoustic impedance.

Figure 3.6 is a schematic diagram of the transducer constructed for the lower frequency range. Its composite structure consists of a PZT disk as its driving element bonded to a length of thin aluminium tubing. The transducer vibrates in its longitudinal mode at a frequency determined by the length L of the structure and by the elastic properties of the material. By using a tube instead of a rod,the effective density of the transducer is reduced, thereby reducing the impedance mismatch and improving the acoustic coupling between the transducer and the medium.

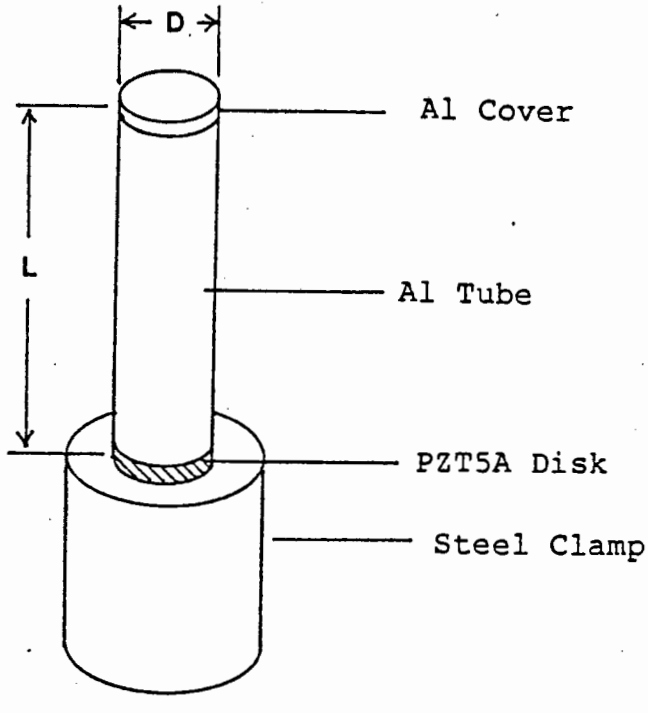

Figure 3.6: Composite thickness-mode transducer clamped at one end. The resonant frequency and, therefore, the D/λ ratio are varied by reducing the length L of the aluminium tube.

The D/λ ratio of the above transducer is varied by machining down the length of the aluminium tube. As the length L is reduced, the longitudinal resonant frequency of the composite

transducer goes up and, therefore, a shorter wavelength is generated in the medium. The diameter D of the radiating surface remains unchanged. Note that the transducer is clamped at one end, and so its fundamental mode of longitudinal vibration will be the "quarter-wavelength" mode. Furthermore, as the D/λ ratio of the transducer is varied, the internal losses within the bonding layers and the PZT disk remain unchanged. This is an attractive feature since any change in the resistive and reactive components of the acoustic impedance of the transducer can be considered to be due to changes in the radiation impedance Z_{rad} only.

Transducers in the higher frequency region are implemented by using four PZT5A disks vibrating in thickness-mode. Their resonant frequencies lie between 1.5 and 2.5 MHz and their diameters are 5, 10, 25, 40 mm respectively. The wavelength of a 2 MHz acoustic wave in water is 0.75 mm and, thus, for all four transducers, the D/λ ratio is large compared to the case of the composite transducers. In this case, the D/λ ratios for the four transducers vary between 6 and 67.

3.2.5 Experimental Results

In the lower frequency range, the length of the composite transducer of Figure 3.6 is gradually machined down and, at every length L, admittance circle diagrams are obtained for the transducer operating firstly in air and then in water. The components of radiation impedance are then calculated by the method described in section 3.2.3.

As discussed previously, the components of radiation impedance R_{rad} and L_{rad} are combined with the components of the mechanical impedance of the transducer, R_l and L_m, to produce R_{tot} and L_{tot}. To assess the true contribution of the radiation impedance to the total impedance of the transducer, the relative increase in inductive and resistive loading due to L_{rad} and R_{rad} must be evaluated, i.e. the percentage changes in L_{tot} and R_{tot} due to L_{rad} and R_{rad} are calculated.

Six sets of admittance circle diagrams are obtained for six lengths L of the composite transducer. These are shown in Figure 3.7 (i)&(ii). From these circle diagrams, the resistive and reactive components of radiation impedance are calculated and the relative changes in resistive and inductive loading are tabulated in Table 3.1 below.

L(mm)	D/λ	$(f_s-f_s')/f_s$ %	R_{rad}/R_{tot} %	L_{rad}/L_{tot} %
31.6	0.30	5.0	88.0	9.7
27.7	0.33	5.9	72.8	11.6
23.5	0.37	6.9	72.4	13.4
21.5	0.40	8.6	87.8	16.7
16.9	0.42	26.5	92.8	48.5
13.4	0.45	31.5	94.4	58.7

Table 3.1: Relative values of resistive and inductive components of radiation impedance measured for various values of D/λ . L_{rad}/L_{tot} and R_{rad}/R_{tot} give the relative changes in inductive and resistive loading respectively.

The two components of radiation impedance, namely R_{rad}/R_{tot} and L_{rad}/L_{tot}, are plotted against D/λ as shown in Figure 3.8 for values listed in Table 3.1 above. The resistive component R_{rad}/R_{tot} initially drops as D/λ increases and then rises to a plateau as D/λ increases further. The high percentage value of R_{rad}/R_{tot} (≈90%) indicates that most of the energy losses in the transducer are due to radiation. Internal losses within the transducer are consequently small (typically 10%).

The inductive component of radiation impedance L_{rad}/L_{tot} increases as the D/λ ratio increases and becomes particularly significant for values of D/λ greater than 0.40 as can be seen from the plot of Figure 3.8(ii). This large inductive loading of the medium is responsible for the change in the resonant frequency of the transducer as it is moved from air to the medium.

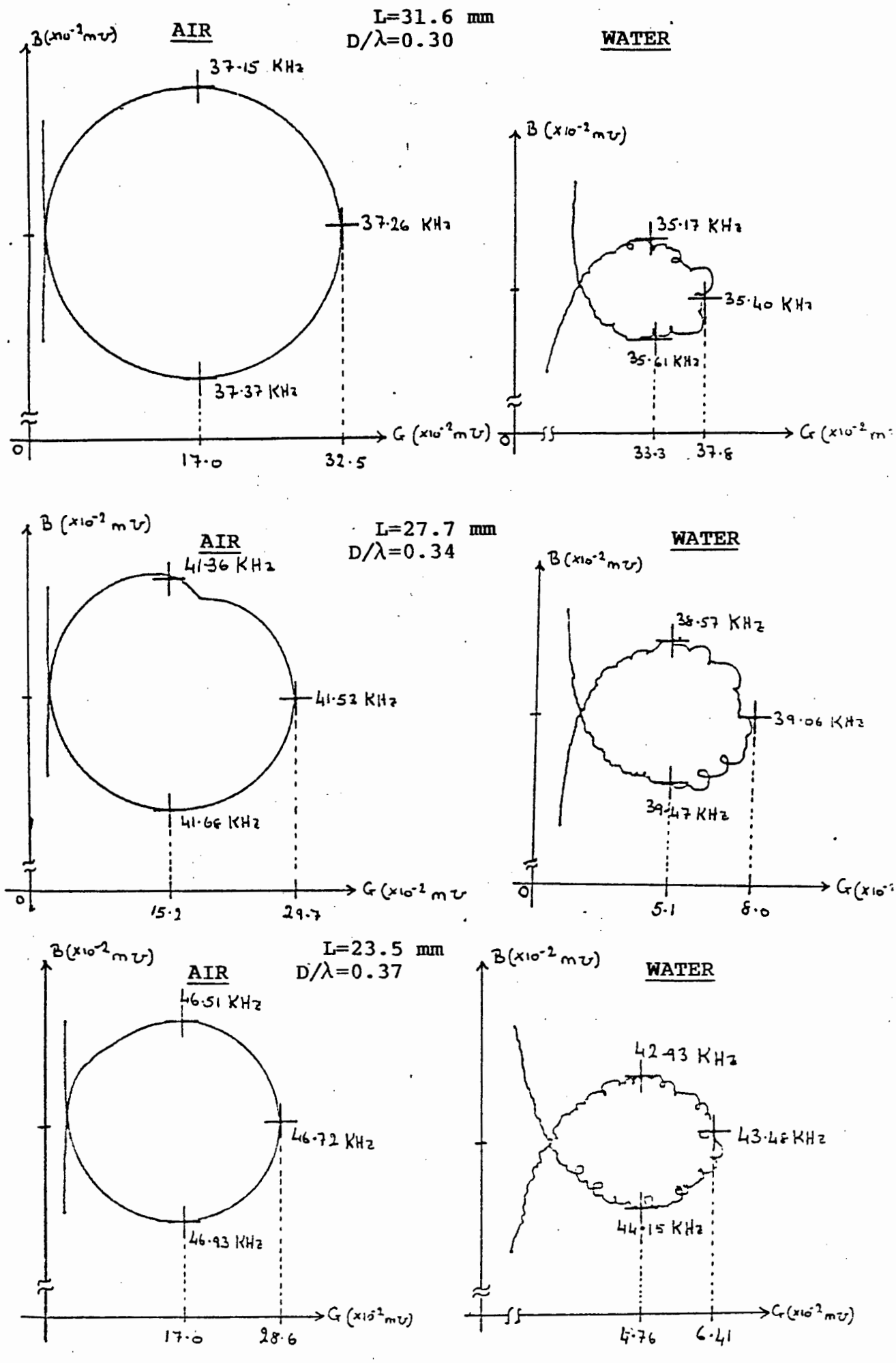

Figure 3.7 (i): Admittance circle diagrams for different lengths L and D/λ ratios of composite transducer operating in air and in water.

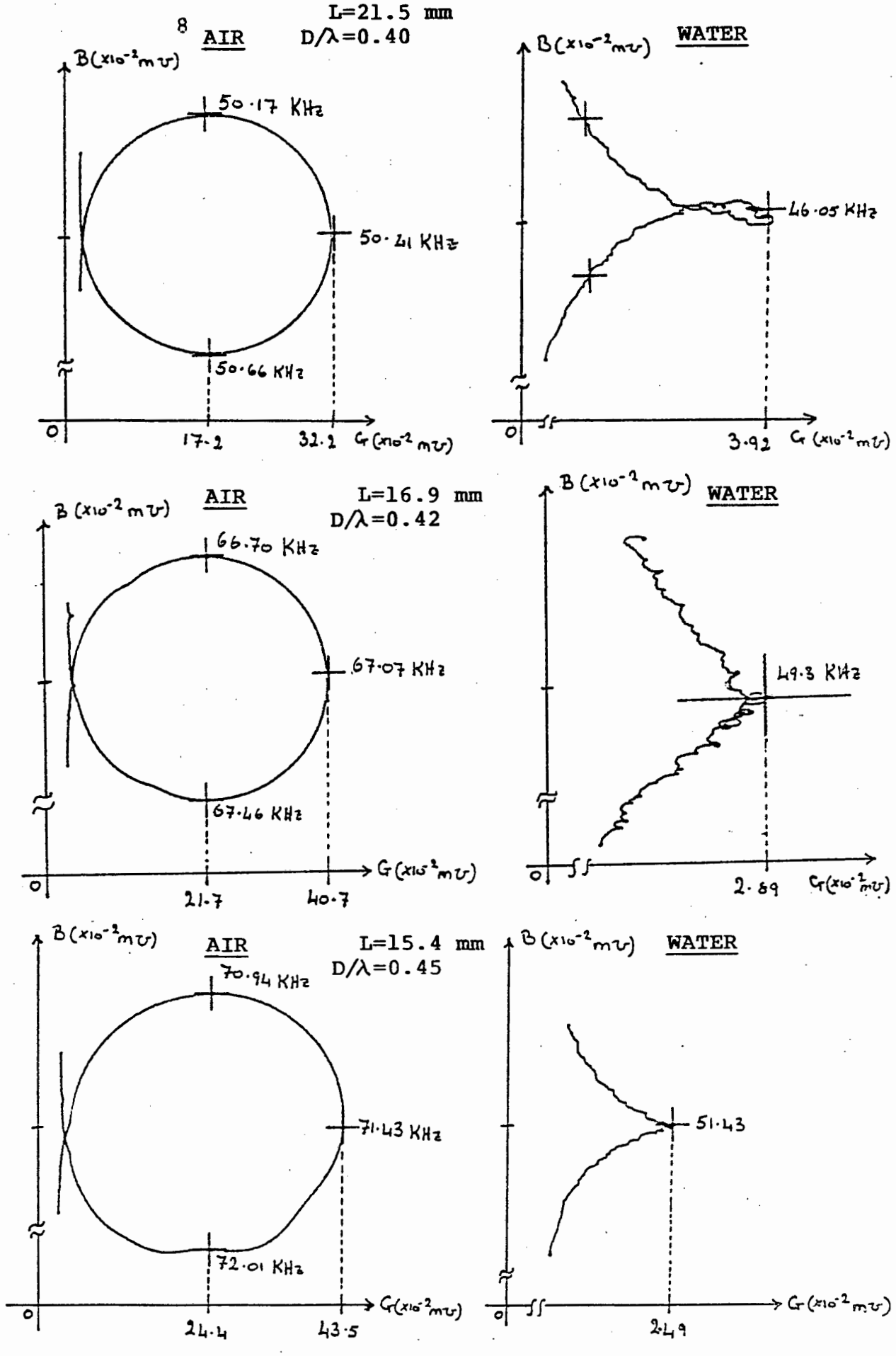
8
AIR
L=21.5 mm
D/λ=0.40
B(x10⁻²mU)
50·17 KHz
50·41 KHz
50·66 KHz
0
17·2
32·2
G (x10⁻²mU)
WATER
B(x10⁻²mU)
46·05 KHz
0
3·92
G (x10⁻²mU)
AIR
L=16.9 mm
D/λ=0.42
B (x10⁻²mU)
66·70 KHz
67·07 KHz
67·46 KHz
0
21·7
40·7
G (x10⁻²mU)
WATER
B (x10⁻²mU)
49·3 KHz
0
2·89
G(x10⁻²mU)
AIR
L=15.4 mm
D/λ=0.45
B (x10⁻²mU)
70·94 KHz
71·43 KHz
72·01 KHz
0
24·4
43·5
G(x10⁻²mU)
WATER
B (x10⁻²mU)
51·43
0
2·49
G (x10⁻²mU)

Figure 3.7 (ii)

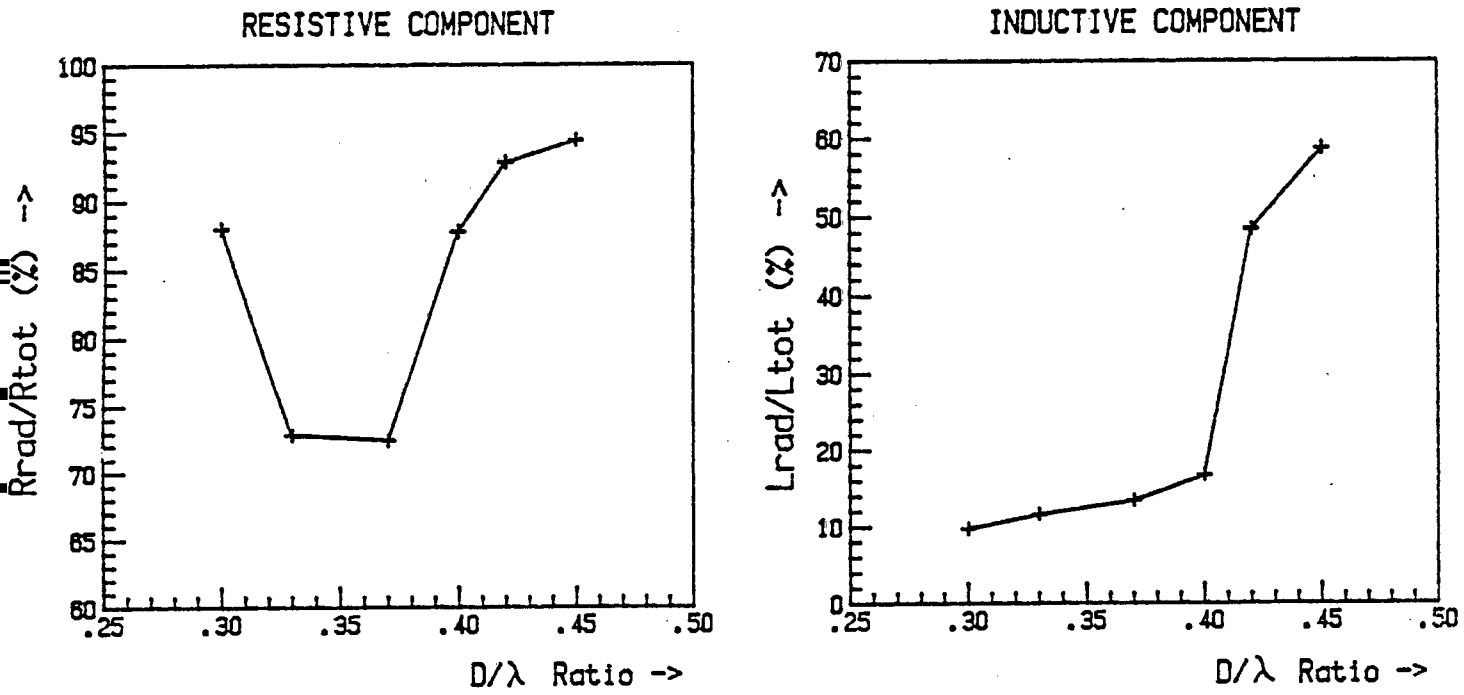

Figure 3.8: Experimental curves of the resistive and reactive components of radiation impedance for a longitudinal mode composite transducer operating in water.

A comparison of the experimental curves of Figure 3.8 with those of Figure 3.1 indicates that there is reasonable agreement with regards to the general trends of R_{rad} and L_{rad} over the range of the experimental D/λ ratios. In the case of L_{rad}, theory predicts that as D/λ increases, L_{rad} goes through a maximum at $D/\lambda = 0.47$ and then decreases to zero for large values of D/λ. Over the experimental range of the D/λ ratio, i.e. for D/λ ranging from 0.30 to 0.45, it is seen that L_{rad}/L_{tot} increases as D/λ increases, thus agreeing with theoretical predictions. Similarly for the case of radiation resistance R_{rad}, the theoretical curve of Figure 3.1 indicates that R_{rad} increases as D/λ increases and then reaches a plateau for large values of D/λ. The general trend as observed from the experimental curve of Figure 3.8(i) agrees with theory in that R_{rad}/R_{tot} also increases as D/λ increases from 0.30 to 0.45.

In the higher frequency region, i.e. between 1 and 3 MHz, the radiation impedance of a thickness-mode transducer is analysed as a function of D/λ by means of four PZT5A disks of the same thickness but of different diameters operating in water. The resonant frequencies lie between 1 and 3 MHz and their D/λ ratios range from 6 to 67. These values of frequency and D/λ ratios are particularly relevant to the study of broadband ultrasonic transducers since they are of the same order as those encountered with piezoceramic disks used in the construction of ultrasonic transducers for operation in the 0.1-10 MHz range.

The admittance circle diagrams obtained for the four transducers operating in air and in water are given in Figures 3.9 (i) to (iv). Note that the resonant frequency of any particular transducer is the same in air and in water. This implies that the radiation impedance of the transducer is purely resistive and thus the inductive component L_{rad} is zero. This observation is in agreement with theory which predicts that L_{rad} vanishes as D/λ becomes large. The resistive component relative to the total mechanical resistance, i.e. R_{rad}/R_{tot}, is obtained from measurements on the circle diagrams and tabulated as a percentage in Table 3.2 below.

D(mm)	f_s(MHz)	D/λ	R_{rad}/R_{tot} %
40	2.50	67	21
25	1.71	28	26
10	1.98	13	80
5	1.92	6	64

Table 3.2: Relative values of the resistive component of radiation impedance for four piezoceramic transducers of various D/λ ratios. Acoustic coupling is strongest when $D/\lambda = 13$.

The highest value of resistive loading determined experimentally occurs when the D/λ ratio of the thickness-mode transducer is equal to 13. The behaviour of the radiation resistance as D/λ increases is such that it initially

PZT5A DISK: D=40 mm, t=1 mm, D/λ =67

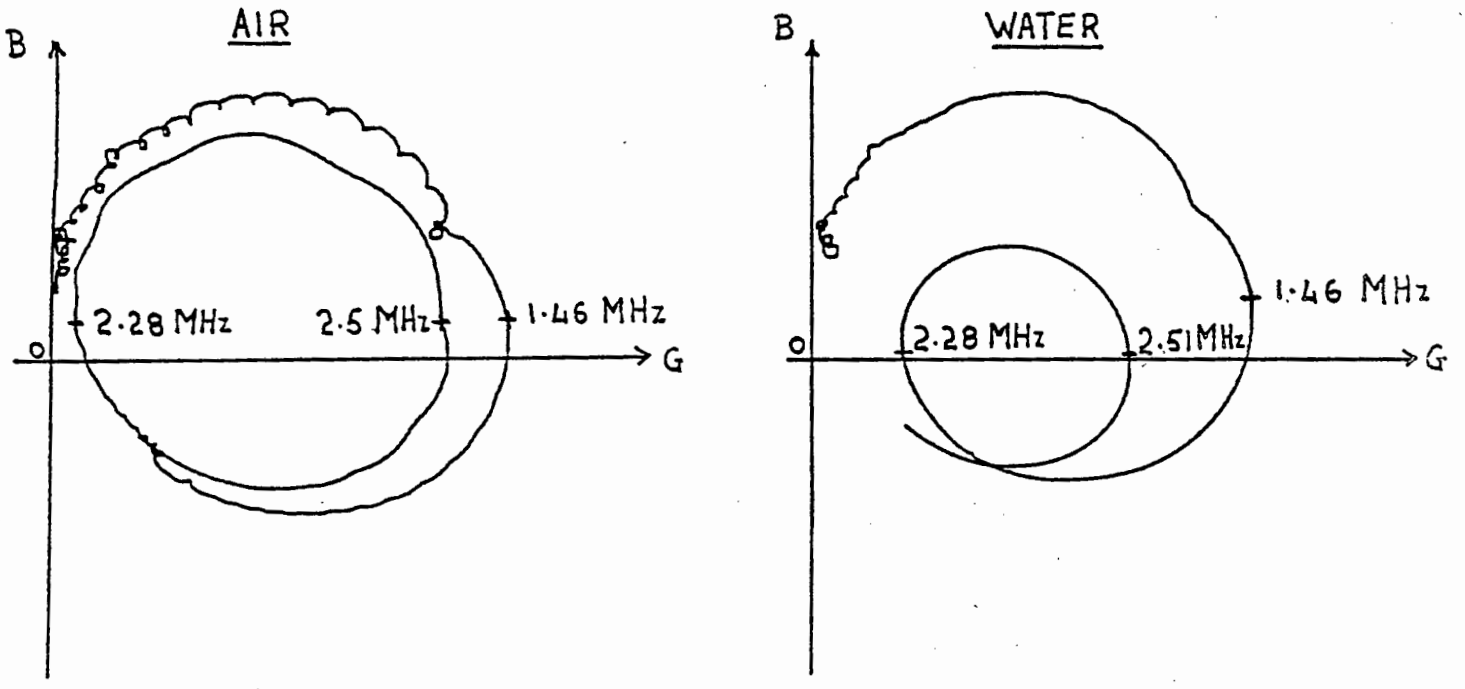

Figure 3.9(i): Admittance Circle diagrams of 2 MHz PZT5A transducer of diameter 40mm operating in air and in water. Note that the same scale is used for both cases.

PZT5A DISK: D=25mm, t=1mm, D/λ =28

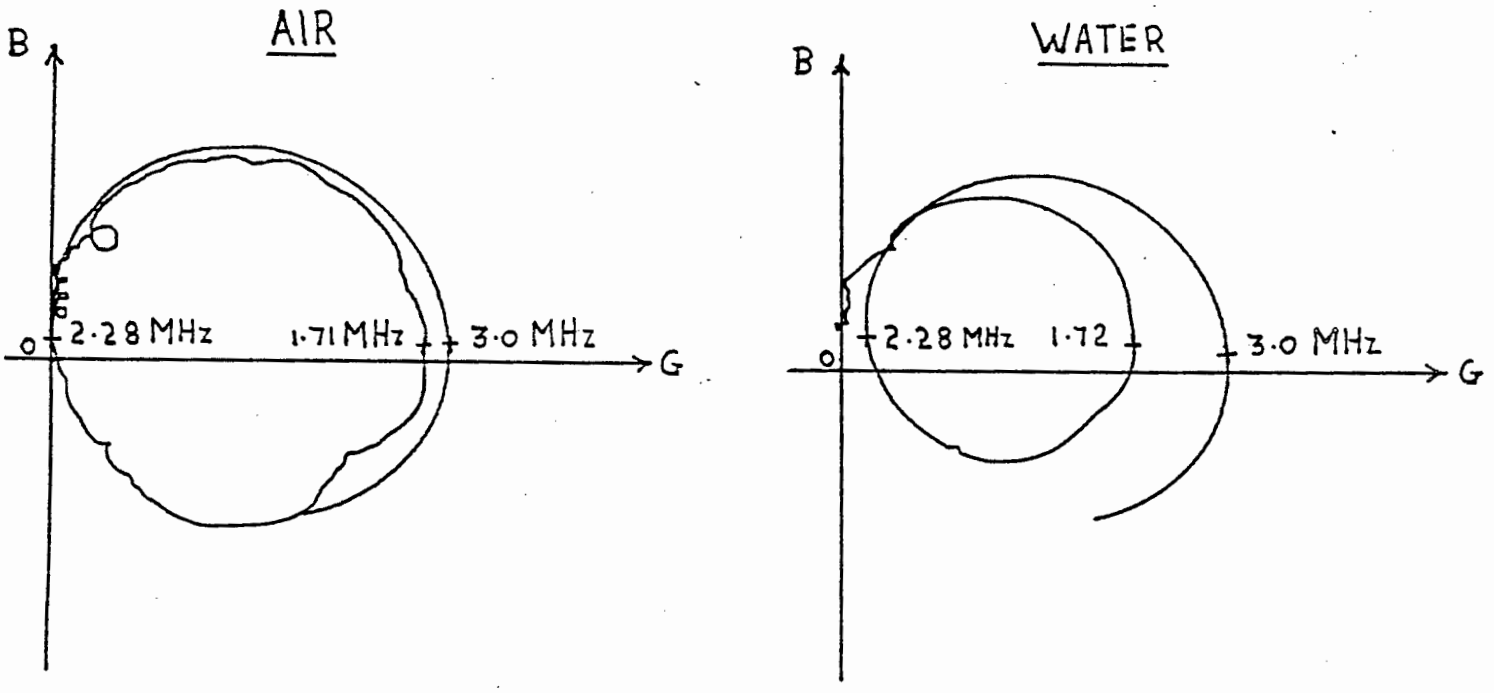

Figure 3.9(ii): Admittance circle diagrams of 2 MHz transducer of diameter 25 mm radiating in air and water media

PZT5A DISK: D=10 mm, t=1 mm, D/λ =13

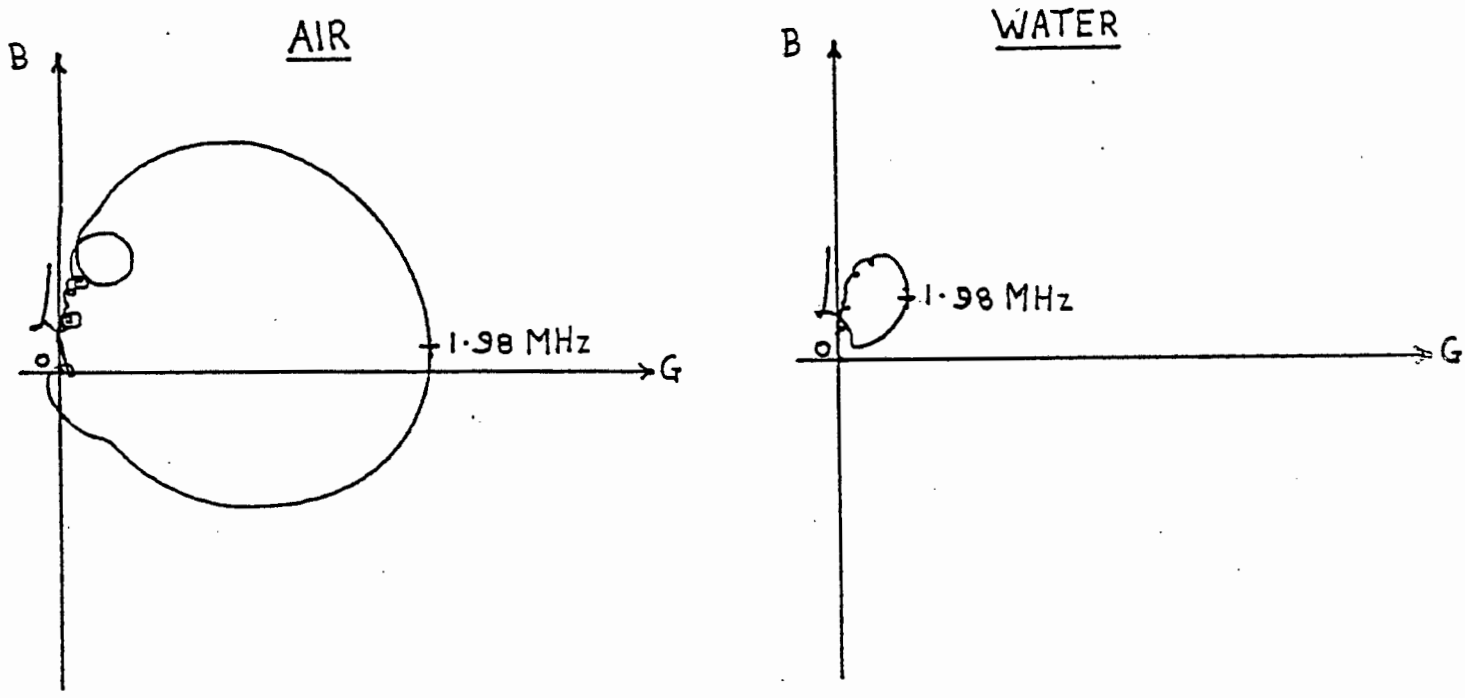

Figure 3.9(iii): Admittance circle diagrams of 2MHz PZT5A transducer of diameter 10 mm operating in air and in water. Note the strong acoustic coupling of the transducer with the loading water medium.

PZT5A DISK: D=5 mm, t=1 mm, D/λ =7

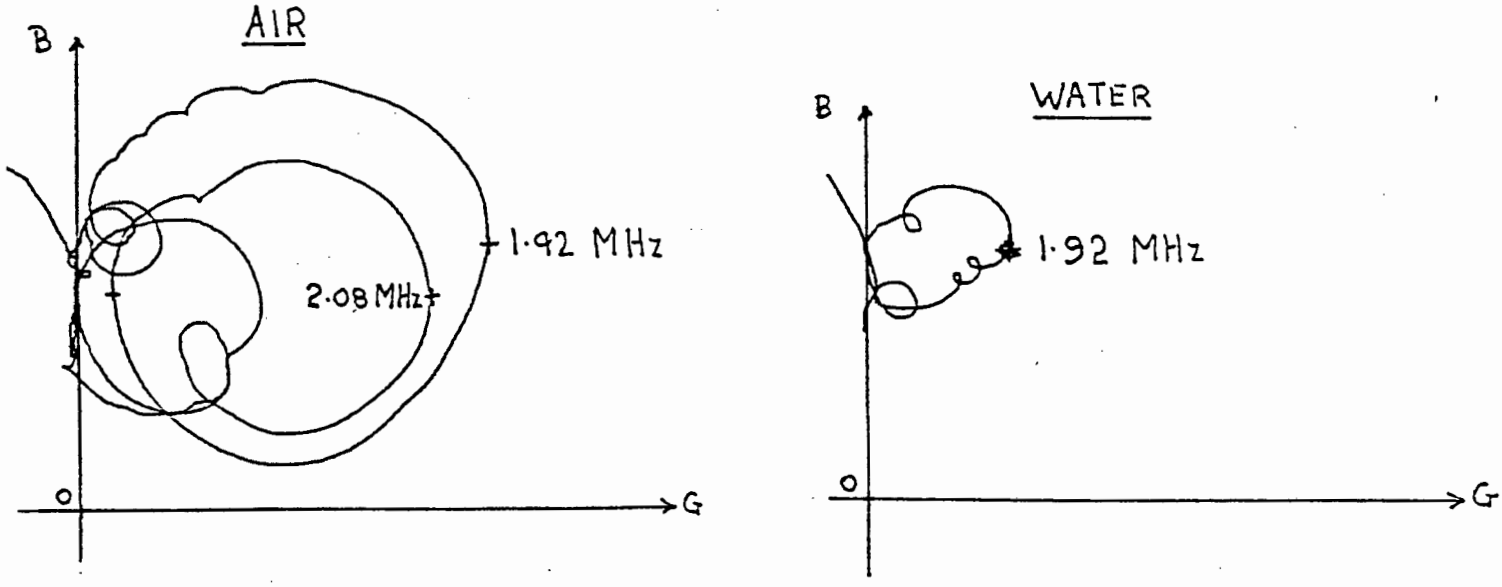

Figure 3.9(iv): Admittance circle diagrams of 2 MHz PZT5A transducer of diameter 5 mm operating in air and in water.

increases, reaches a maximum and then decreases as D/λ increases further. This behaviour does not agree with the theoretical curves of Figure 3.1 which indicate that the resistive component of radiation impedance reaches a plateau at $D/\lambda \approx 2$ and remains constant thereafter. A possible explanation for this observed difference is that the thickness mode is degenerate, i.e. the radiating surface is characterised by a number of profiles which are unresolvable from the principal piston-like vibration. This experimental observation is important as it suggests that there exists an optimum value of D/λ for maximising the radiation resistance of a transducer and, hence, its acoustic coupling to the loading medium.

3.3 Beam characteristics as a function of D/λ .

3.3.1 Theory

The two aspects of beam characteristics considered in this chapter, namely, extent of near-field and directivity, are analysed theoretically in various textbooks [10,13] in terms of the geometry of the source and the wavelength of the acoustic wave in the medium. This section does not give a detailed description of the theory but mérely outlines the pertinent equations to illustrate the effects of the diameter to wavelength ratio, D/λ, on the beam characteristics of a transducer.

The presence of a near-field and a far-field region in the beam of a transducer arises from interference effects in the sound pressure response along the axis of the transducer. These interferences give rise to a fluctuating pressure field in the immediate vicinity of the transducer, while in the far-field, the pressure distribution becomes smooth and free of interference patterns. Figure 3.10 shows the theoretical and measured axial sound pressure curves for a 5 MHz quartz transducer operating in water [18]. From this graph, the near-field/far-field boundary is located at the point where the relative sound pressure stops fluctuating and starts decaying smoothly, i.e. at 7.5 cm from the transducer.

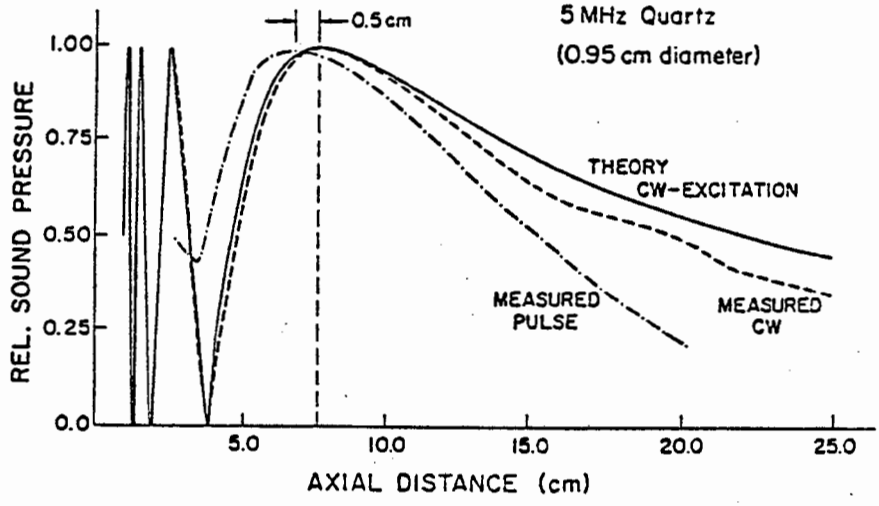

Figure 3.10: Theoretical and experimental axial sound pressure curves of a 5 MHz quartz transducer operating in water. The extent of the near-field as obtained from these curves is about 7.5 cm.

For a reasonably directive source of simple geometry, the extent of the near-field can be estimated from the size and geometry of the source and the frequency of excitation. For the case of a flat pistonlike source, the criterion used for the boundary of the near-field is that the distance from any point on the source to a point on the acoustic axis must not differ by more than half a wavelength. A diagramatic representation of this criterion is given in Figure 3.11 below.

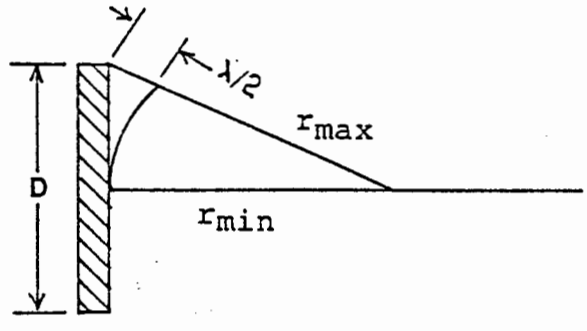

Figure 3.11: Geometry used in estimating the extent of the near-field of a flat circular pistonlike source.

Thus, the extent of the near-field, L_N, can be expressed in terms of the diameter of the source and the wavelength as follows:

$$L_N = D^2/4\lambda \quad \ldots\ldots\ldots\ldots\ldots\ldots \quad (3.15)$$

The directivity of a transducer is a function of the beamwidth of the main lobe of the radiation pattern of the transducer. The beam pattern for a circular plane piston of D/λ equal to 1.6 is computed theoretically [13] and plotted as shown in Figure 3.12 below. The angle subtended by the major lobe in this case is 45^{o}. Note that the larger the beamwidth of the radiation pattern, the lower the directivity of the transducer.

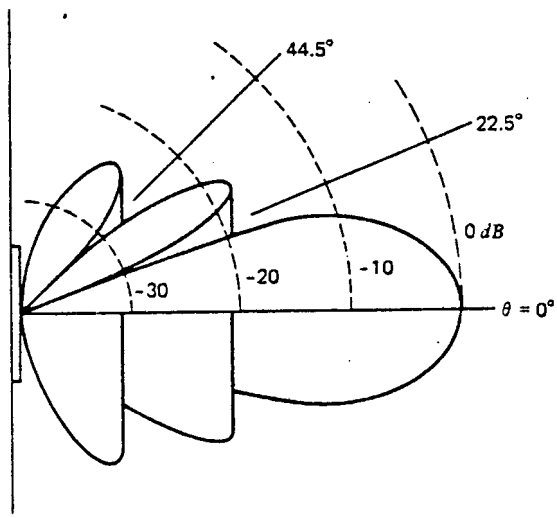

Figure 3.12: Theoretical beam pattern of a circular plane piston of D/λ ratio 1.6.

In order to estimate the beamwidth of a transducer, use is again made of the geometry and size of the transducer and the wavelength in the medium. The criterion used in this case is that a null occurs when half of the source elements on the radiating surface of the transducer are out of phase with the other half. This is represented diagramatically in Figure 3.13.

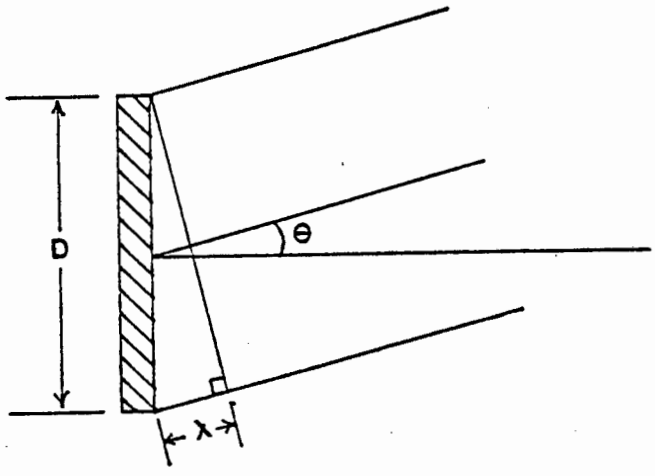

Figure 3.13: Geometry used for estimating beamwidth

Thus the beam angle subtended by the major lobe is given by:

$$\text{Sin } \theta = \lambda/D$$

For small θ, i.e. for a highly directional beam, the above equation can be approximated as

$$\theta = \lambda/D \quad \text{radian}$$

Therefore, the beamwidth in degrees is given by

$$\theta_B = 2\theta = (180/\pi).2\,\lambda/D \quad \ldots\ldots\ldots\ldots\ldots\ldots \quad (3.16)$$

3.3.2 Practical implications of directivity and extent of near-field.

A knowledge of the directivity of a transducer is particularly important in applications where the transducer operates in pulse-echo mode or through-transmission mode. In both modes, the beam generated by the source is directed towards either a reflector or a receiver. The amplitude of the received signal depends on the directivity of the beam and on the alignment of the reflector/receiver relative to the transmitter. Furthermore, the directivity of a beam generated by a transducer varies with distance along the axis of the

transducer. In the near-field, the directivity of the beam is higher than in the far-field.

To illustrate the implications of directivity on the performance of a pulse-echo system, consider the two cases of Figure 3.14. In case (i), a slight misalignment of the reflector causes the reflected beam to miss the transducer and thus no echo is received. In case (ii), the transducer produces a wider beam which, after reflection from the same misaligned reflector, still produces an echo. Thus, a highly directional transducer has the disadvantage of being more sensitive to reflector alignment than a lowly directional one. However, if the reflector is properly aligned, the former will produce better echoes than the latter.

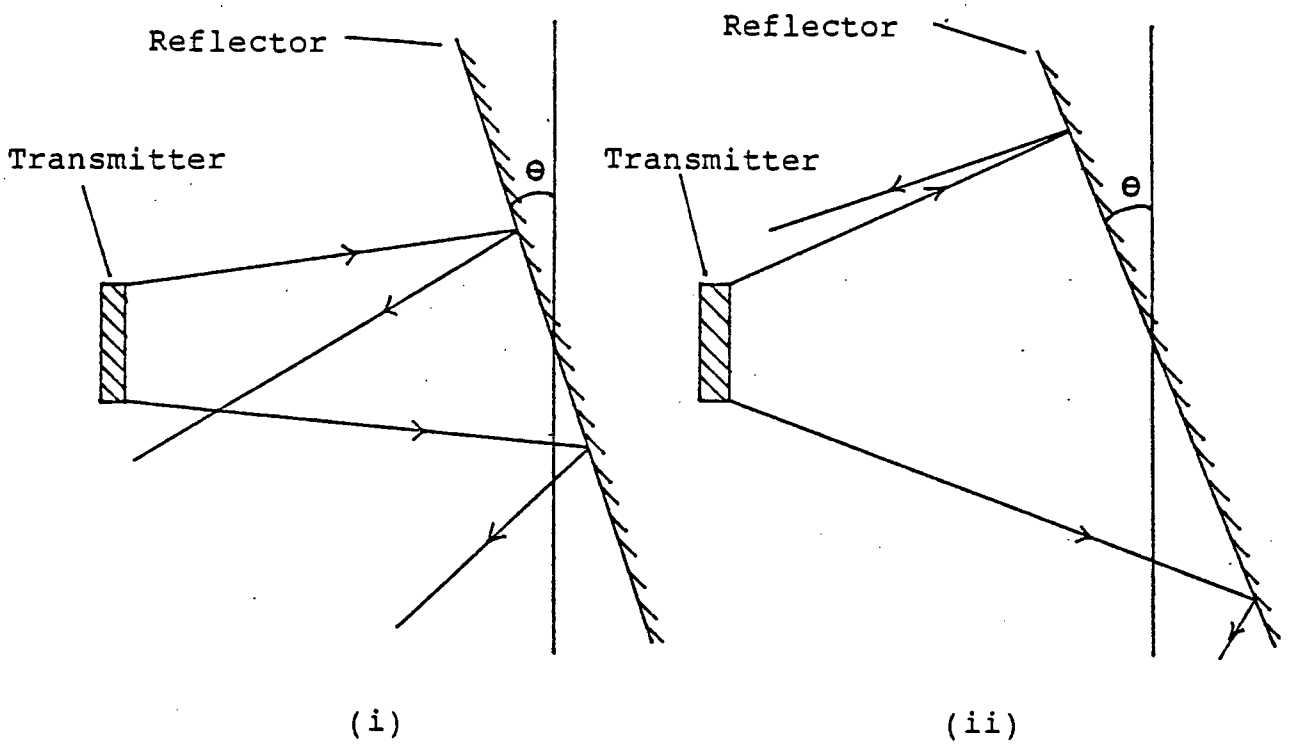

Figure 3.14: Effect of beamwidth and reflector alignment on the performance of a pulse-echo system.

The relationship between directivity and the extent of the near-field is illustrated in Figure 3.15 where the field pattern of a 2.25 MHz transducer in water is measured interferometrically [18]. The beamwidth reaches a minimum at about 2 cm from the transducer and then widens further along the axis.

For this particular transducer, the theoretical near-field limit as calculated from equation (3.15) is 3.7 cm. Thus, the directivity of this transducer is a maximum in the near-field.

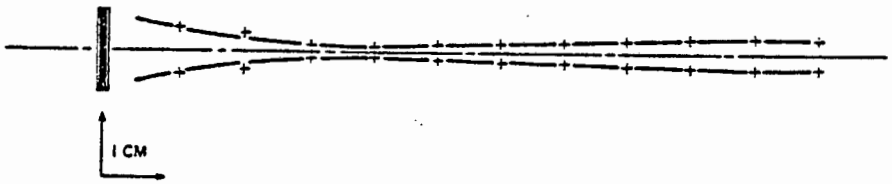

Figure 3.15: Actual field pattern of a 2.25 MHz transducer operating in water measured by an interferometric technique. The theoretical near-field limit of this transducer is 3.7 cm.

In a pulse-echo system, the directivity of the beam is determined firstly by the D/λ ratio of the transducer and secondly by the distance between the transducer and the reflector. A transducer of high D/λ ratio will be highly directional and its near-field limit will be far from the transducer. Therefore, a reflector placed in the near-field of such a transducer will result in an arrangement which is highly sensitive to the alignment of the reflector. However, strong echoes will be received if the reflector is aligned properly. On the other hand, if a transducer of low D/λ ratio is used, the directivity of the beam will be low and the extent of the near-field small. Such a transducer will be relatively insensitive to reflector alignment but will have the disadvantage of producing very weak echoes. Thus, for a given application, the optimum D/λ ratio must be chosen for the transducer so as to produce the required directivity for a given transmitter/reflector distance.

3.3.3 Experimental procedure

A qualitative measurement of the directivity and beamwidth of a ttansducer is performed by driving the transducer in pulse-echo mode and recording the echo amplitude as the distance between the transducer and reflector is varied. Throughout the

experiment, the transducer is excited by a burst of constant amplitude and frequency, the frequency being equal to the resonant frequency of the transducer. Figure 3.16 below shows a schematic diagram of the apparatus used.

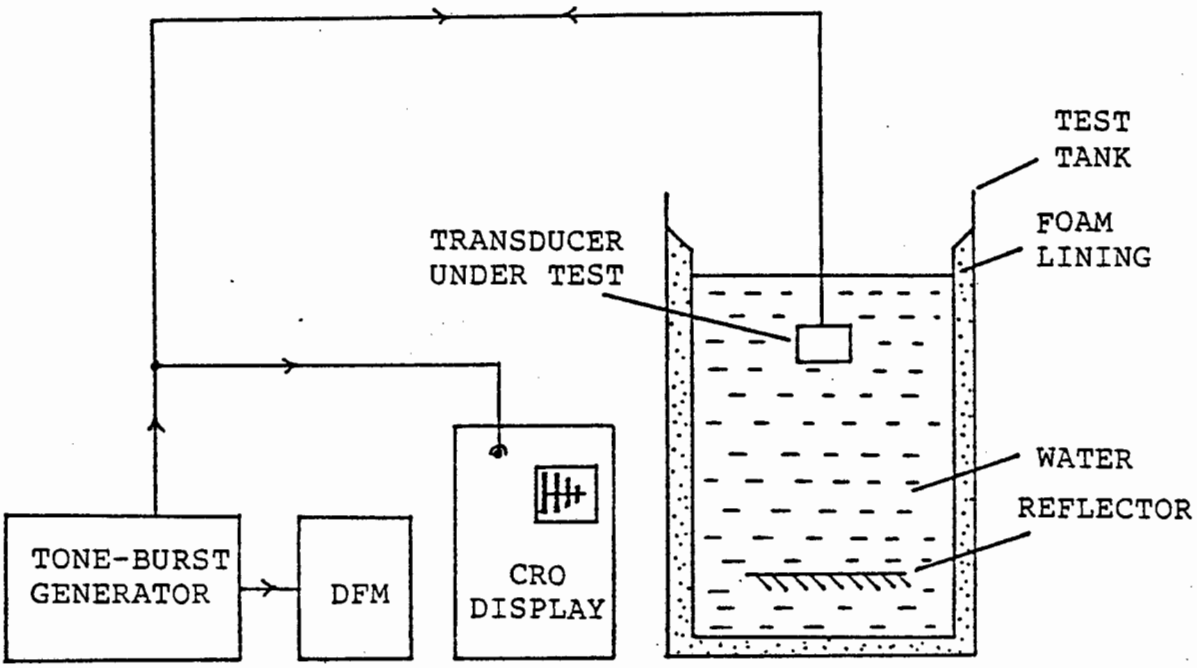

Figure 3.16: Laboratory set-up used for the qualitative evaluation of the beamwidth of a transducer as a function of D/λ .

The transducer under test is excited by a burst of oscillations derived from the tone-burst generator and an echo is produced after reflection from the reflector. The amplitude of the echo is measured directly on the oscilloscope display. The distance between the transducer and the reflector is then changed and the new echo amplitude recorded. Before every measurement, the reflector and the transducer are aligned by adjusting the orientation of the reflector so that the largest echo signal is obtained.

3.3.4 Experimental results

Four piezoceramic disks of thickness 1.0 mm and diameters 5, 10, 25 and 40 are excited in pulse-echo mode in water and their echo amplitudes are recorded for various transducer-reflector distances by means of the laboratory set-up of Figure 3.16. The four transducers have a resonant frequency of approximately 2 MHz with their D/λ ratios varying between 6 and 55. Thus, the extent of the near-field L_N will be different for each transducer as this is proportional to D^2/λ as seen from equation (3.15). Similarly, their beamwidths will differ since, from equation (3.16), these are inversely proportional to D/λ. Using these two equations, theoretical values for the extent of the near-field and the beamwidth are obtained for each transducer operating in water at a resonant frequency of 2 MHz and tabulated below.

D (mm)	D/λ	Near-field L_N (mm)	Beamwidth $\theta_B{}^\circ$
5.0	6.7	8	17.0
10.0	13.4	33	8.5
25.0	33.3	208	3.5
40.0	53.3	533	2.0

Table 3.3: Beamwidth and extent of near-field calculated for four 2 MHz transducers operating in water.

Thus a transducer of small diameter has a short near-field range while one of larger diameter is characterised by a narrower beam and a more extensive near-field.

Table 3.4 lists the measurements of echo amplitudes and corresponding transducer-reflector distances for the four transducers used. Note that the reflector position is expressed as a ratio of the actual distance d to the length of the near-field limit, L_N, i.e. as d/L_N .

D = 40.0 mm		D = 25.0 mm		D = 10.0 mm		D = 5.0 mm	
d/L_N	$V_{echo}(V)$	d/L_N	$V_{echo}(V)$	d/L_N	$V_{echo}(V)$	d/L_N	$V_{echo}(V)$
0.03	2.5	0.07	2.6	0.45	2.5	1.8	0.94
0.04	2.4	0.10	2.5	0.67	2.7	2.6	0.72
0.06	2.4	0.14	2.4	0.91	2.7	3.6	0.53
0.07	2.3	0.18	2.3	1.15	2.6	4.6	0.49
0.08	2.3	0.21	2.4	1.33	2.5	6.3	0.35
0.11	2.3	0.29	2.2				

Table 3.4: Echo amplitudes of four thickness-mode transducers measured at various positions of the reflector along the axis of the transducer. The reflector position is normalised with respect to the extent of the near-field L_N.

The above results are plotted on the same set of axes as shown in Figure 3.17. A logarithmic scale is used on the d/L_N axis so as to cover the entire range of values, and the echo amplitudes are normalised with respect to the largest echo obtained for each transducer. A distinguishing feature of this graph is the sharp decrease in the amplitude of the echo signal as the reflector is moved from the near-field to the far-field region. This is due to the beamwidth of the transducer becoming larger in the far-field and therefore less energy is reflected back to the transducer.

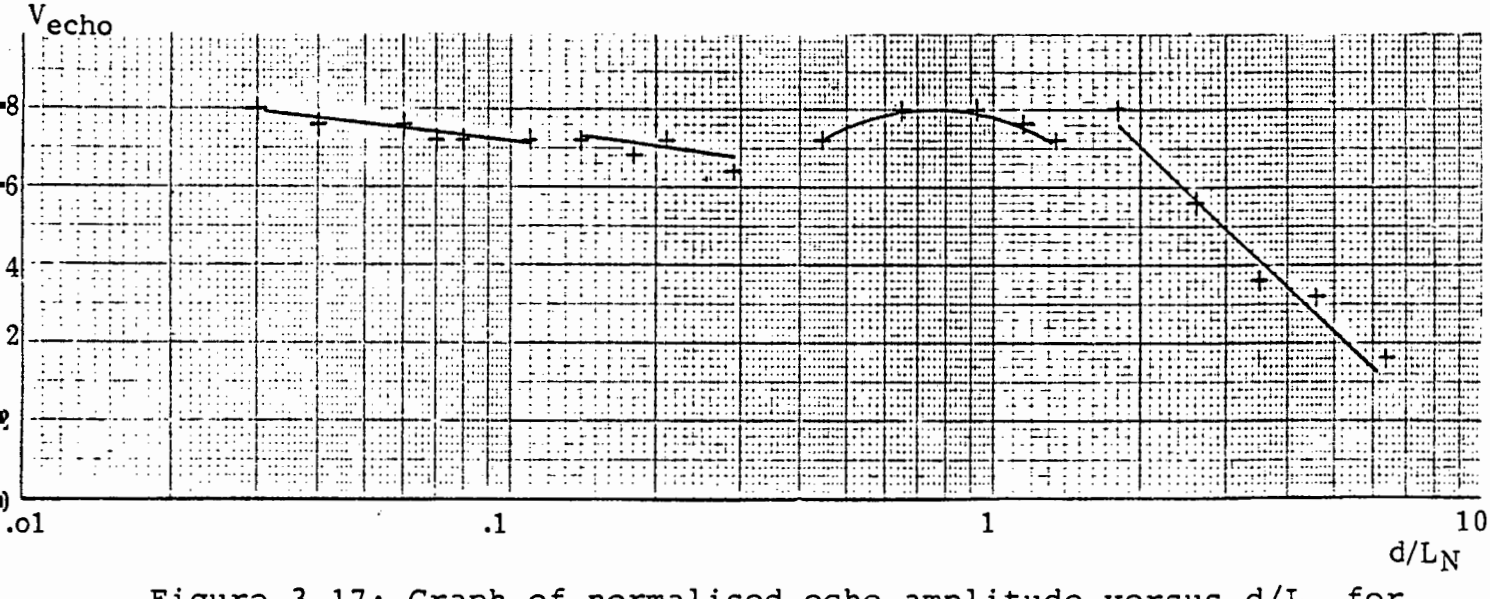

Figure 3.17: Graph of normalised echo amplitude versus d/L_N for four 2 MHz thickness-mode transducers.

When a transducer operates in the pulse-echo mode, the amplitude of the received signal depends on the position of the reflector and on the cross-sectional area of the beam at the reflector position. For a given reflector position, the following relationship holds:

$$V_{echo}^2 \propto 1/A$$

or $$V_{echo}^2 \propto 1/R^2$$

where A is the cross-sectional area of the beam and R is the radius. Thus, the radius of the cross-section of the beam at any point along the axis of the transducer is inversely proportional to the amplitude of the echo obtained when the reflector is placed at that point, i.e.,

$$R \propto 1/V_{echo}$$

The beam profile of a transducer can therefore be mapped by plotting the inverse of the echo amplitude against the corresponding reflector position. The results of Table 3.4 are used to map the beam profile of a circular thickness-mode transducer by plotting the normalised reciprocal of echo amplitude versus the corresponding normalised reflector position, d/L_N, as shown in Figure 3.18 below.

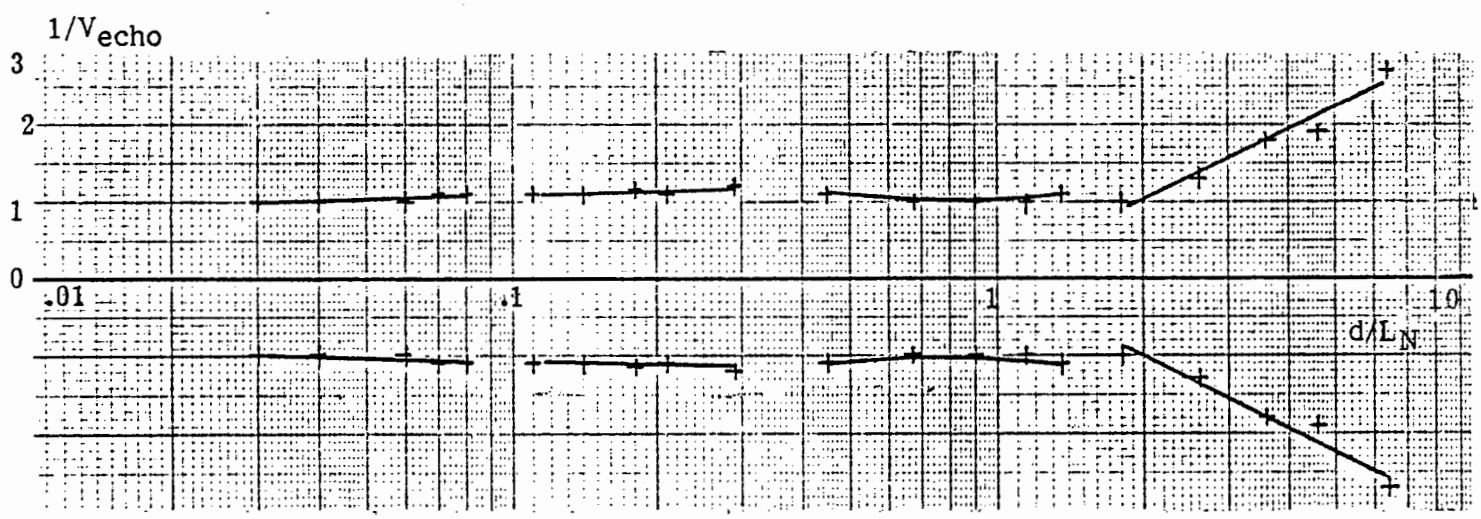

Figure 3.18: Beam profile of a circular thickness-mode transducer obtained by plotting $1/V_{echo}$ versus d/L_N for the four 2 MHz transducers.

The experimental beam profile depicted above has similar characteristics to the one of Figure 3.15 in that they both converge slightly in the near-field region and then diverge with an increasing beamwidth in the far-field.

3.4 Discussion of results

Radiation impedance has been investigated as a function of the D/λ ratio over two frequency ranges. The first extended from 37 kHz to 92 kHz with D/λ ranging from 0.30 to 0.45 whereas the second one went from 1 to 3 MHz with D/λ varying between 6 and 67. In the lower frequency range, the radiation impedance possessed both a resistive and a reactive component. The general trends observed experimentally agreed favourably with theory which predicts that over the D/λ range covered, both components of radiation impedance increase with increasing D/λ However, in the higher frequency range, the behaviour of the resistive component did not agree with theory. While theory predicts that the radiation resistance per unit area is constant for values of $D/\lambda > 3$, experiment showed that it is a maximum at $D/\lambda \approx 13$. This means that the mechanical coupling between a thickness-mode transducer and its surrounding medium is a maximum at that point. Transducers with large D/λ ratios, i.e. tranducers whose diameters are much larger than their thicknesses, were shown to be characterised by relatively low radiation resistances and hence poor acoustic coupling.Thus, when designing a broadband ultrasonic transducer, the D/λ ratio should be chosen to be between 10 and 15 so as to maximise coupling to the loading medium.

As far as beam characteristics of thickness-mode transducers are concerned, experiment showed that the beamwidth and hence the directivity of the beam varied with distance from the transducer. In the near-field, the beamwidth was small, while in the far-field, it diverged and became less directional. Furthermore, it was found that the beamwidth was inversely proportional to the D/λ ratio, i.e. a disk of large diameter and small thickness produced a narrow beam and was therefore highly directional. As mentioned previously, a highly directional source is not always desirable

in a pulse-echo or through transmission application due to the critical role of the alignment of the reflector/receiver. From the experimental beam profile of a circular thickness-mode transducer of Figure 3.18, it is seen that the beam becomes divergent at $d/L_N \approx 1$, i.e. at the beginning of the far-field region. At this point, the beam changes from a highly directional one to one of lower directivity. To reach the right balance between echo amplitude and alignment sensitivity, it becomes apparent that the reflector should be placed in this region. In applications where the distance between the source and the reflector/receiver is of the order of 10 cm and the frequency of operation is of the order of 1 MHz, it was found that the transducer which gave the best compromise between echo amplitude and alignment sensitivity had a D/λ ratio lying between 10 and 15. The same result can be reached by using Figure 3.10 and arguing that the last maximum represents the optimum distance in terms of a balance between directivity and signal strength. For an operating distance of 10cm this approach also yields a D/λ value of 13. Since, for the case of the radiation impedance of a transducer operating in the megahertz region, the optimum D/λ was also found to lie in the same range, i.e. between 10 and 15, it is important that this constraint on the D/λ ratio be satisfied when designing broadband ultrasonic transducers.

CHAPTER 4

ELECTRICAL IMPEDANCE MATCHING ON PZT5A TRANSDUCERS

4.1 Introduction

Techniques for enhancing the bandwidth and efficiency of thickness-mode piezoelectric transducers include the implementation of impedance matching sections at both the electrical and acoustic ports of the transducer. Electrical impedance matching consists of matching the electrical impedance of the transducer to the output impedance of the voltage source driving it in order to optimise energy transfer between the two. This is implemented via the use of an impedance transformer and a tuning component. The component values of the electrical matching section determine to a certain extent the shape of the frequency response of a transducer and thus, depending on the performance requirements placed on the transducer, it is important that the appropriate matching section be selected.

The first part of this chapter is devoted to a theoretical analysis of the effects of various electrical matching circuits on the frequency responses of thickness-mode piezoelectric transmitters and receivers. This is achieved by the use of a computer program which simulates the frequency responses of the simple equivalent electrical models for piezoelectric transmitters and receivers when terminated by various matching networks at their electrical ports. In the case of a transducer operating in pulse-echo mode, its frequency characteristics are analysed by considering the combined effect of the transmitter and receiver frequency responses.

A design procedure for broadening the bandwidth of a thickness-mode piezoelectric transducer operating in pulse-echo mode is developed and implemented on a number of PZT5A disks of resonant frequencies 500 kHz and 2 MHz. Their frequency responses are then measured in water by exciting them with an electrical tone burst of variable frequency and recording the

echo amplitude after reflection from a thin metal plate placed in front of the transducers. The electrically matched transducers are then compared with the unmatched ones in terms of bandwidth and efficiency.

4.2 Theoretical analysis of electrical impedance matching on thickness-mode piezoelectric transducers

4.2.1 The transducer equivalent model

Various eqiuvalent electrical models have been developed for thickness-mode piezoceramic transducers, some of which are based on a transmission line formalism, e.g. the KLM model [2], and others on a lumped-element circuit configuration such as the widely used Mason model [1]. These models have the advantage of allowing a transducer to be analysed with different acoustic loads on either side of the transducer. They also enable the effects of one or more acoustic impedance matching sections on the frequency characteristics of the model to be analysed. However, when studying the effects of electrical impedance matching, it is found that the simple electrical models of Figure 4.1 are adequate. Besides their simplicity, these models lend themselves to analysis by software simulation for a variety of electrical matching sections.

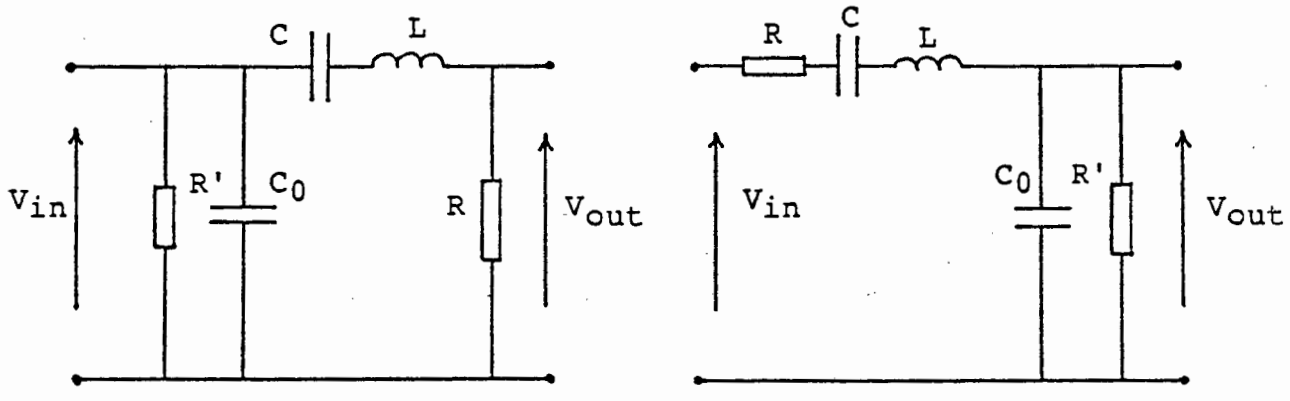

(i) Transmitter (ii) Receiver

Figure 4.1: Equivalent electrical models for a thickness-mode piezoelectric transmitter and receiver.

In both circuits the series RLC branch is the electrical analogue of the mechanical components of the vibrating transducer near its resonant frequency, and the parallel $R'C_o$ branch represents the actual electrical characteristics of the transducer when viewed from its electrical port under static conditions. In the case of the transmitter, the input voltage is applied across the electrical terminals of the transducer while the output appears as a voltage across the resistive component of the RLC branch. In reality however, the transmitter output is a force or pressure signal radiated in the loading medium. In the receiver model, the inputs and outputs are interchanged as shown, i.e. the input pressure signal appears as a voltage source in the series RLC branch while the output appears as a voltage across the electrical terminals of the transducer.

Using the analogy between oscillatory mechanical and electrical systems, it follows that in the case of a transmitter, the resistive component R in the RLC branch is representative of the total energy lost both internally and by radiation in the loading medium, C is the electrical analogue of the stiffness component of the vibrating system and L represents its mass or inertia. C_o is the static electrical capacitance inherent to piezoelectric transducers and R' is the electrical leakage resistance across the terminals of the transducer. Thus, a transducer which couples strongly to its loading medium will radiate a lot of energy in the medium and will consequently be characterised by a high value of R and a low mechanical Q-value. Conversely, weak coupling will be accompanied by a low radiation efficiency and a low R.

The frequency response of a piezoelectric transmitter or receiver can be determined from their respective equivalent models by assigning realistic values to the components of the models and calculating the amplitude of the output voltage as the frequency of the input voltage is varied. A plot of output amplitude versus frequency yields the frequency response of the transducer. When a matching circuit is inserted at the electrical port, the corresponding frequency response is computed in the same manner.

The effects of inductive and capacitive tuning and impedance matching on the frequency response of both a piezoelectric transmitter and receiver are analysed in the following sections for a number of different conditions by means of a computer program which computes the frequency responses of the models of Figure 4.1 with various electrical terminations.

4.2.2 Effect of Inductive Tuning

(i) Transmitter

In this analysis the leakage resistance R' of the piezoelectric transducer is neglected since it is very large compared to X_{Co} over the frequency range of interest. In addition, the voltage source V_{in} is assigned an output impedance R_o of 50Ω to obtain a realistic model of a standard signal generator. Figure 4.2(i) shows the equivalent electrical model of a PZT5A transducer of resonant frequency 1 MHz operating in water. The components of the model are assigned realistic values and the tuning inductor L_o is chosen such that L_oC_o=LC, i.e. the parallel resonant frequency f_p is equal to resonant frequency of the series RLC branch, f_s. The frequency responses for the tuned and untuned cases are obtained by computing the voltage across R as the frequency of the voltage source of constant amplitude is varied. These are plotted as shown in Figure 4.2(ii).

Inductive tuning appears to have had negligible effect on the frequency characteristics of this particular transducer model as illustrated by its response curves.

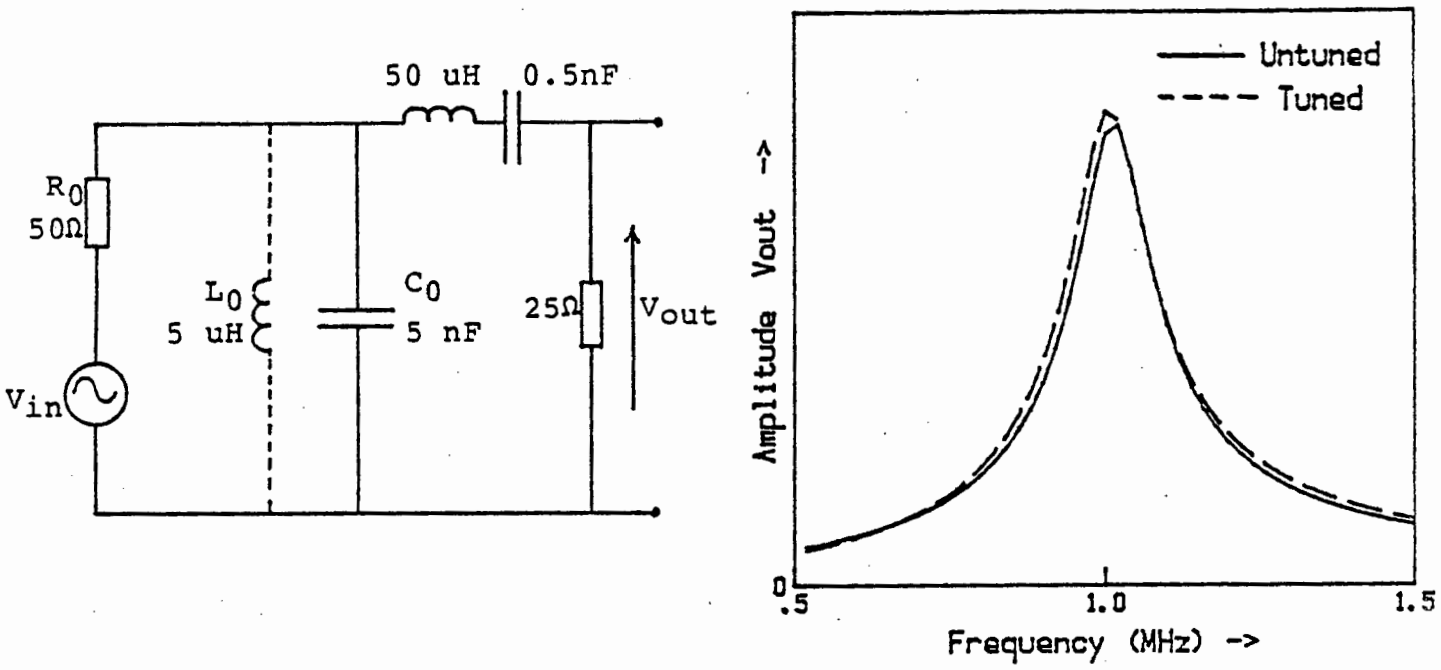

Figure 4.2: (i) Equivalent circuit of an inductively tuned 1-MHz thickness-mode PZT5A transducer driven by a voltage source of 50Ω output impedance.
(ii) Frequency responses of model with and without the presence of L_o.

(ii) Receiver

The effect of inductive tuning on the frequency response of a piezoelectric receiver is analysed using the same component values as those of the transmitter. The equivalent circuit and the corresponding frequency responses with and without inductive tuning are displayed in Figure 4.3 below. Note that in the case of a receiver, the resistance R_o appears in parallel with L_o and C_o.

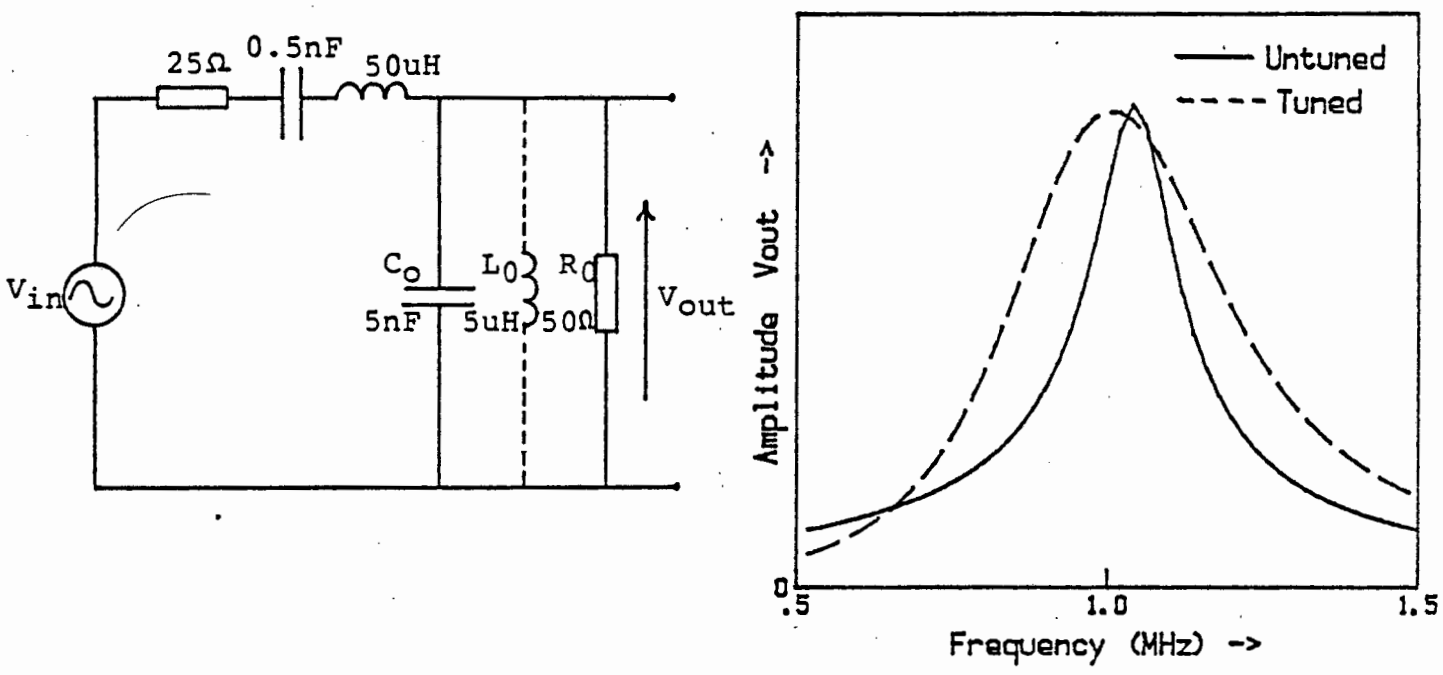

(i) (ii)

Figure 4.3: (i) Equivalent model of 1 MHz PZT5A Receiver implemented with inductive tuning.
(ii) Frequency responses of model with and without inductive tuning.

In this case, a significant improvement in bandwidth is noted. Thus, if this transducer is used in pulse-echo, the overall bandwidth will be enhanced by the implementation of inductive tuning.

4.2.3 Effect of Capacitive Tuning

The effect of the capacitance C_o on the frequency response of a PZT5A transducer is particularly significant in the case of a receiver terminated by a high impedance network, i.e. $R_o=\infty$, or a transmitter driven by a source of zero output impedance, i.e. $R_o=0$ Ω. Figure 4.4(i) shows the equivalent circuit of a 1 MHz PZT5A operating in water and terminated by an open circuit at its electrical port. The frequency response of the model is then calculated for two different values of C_o and plotted as shown in Figure 4.4(ii) below.

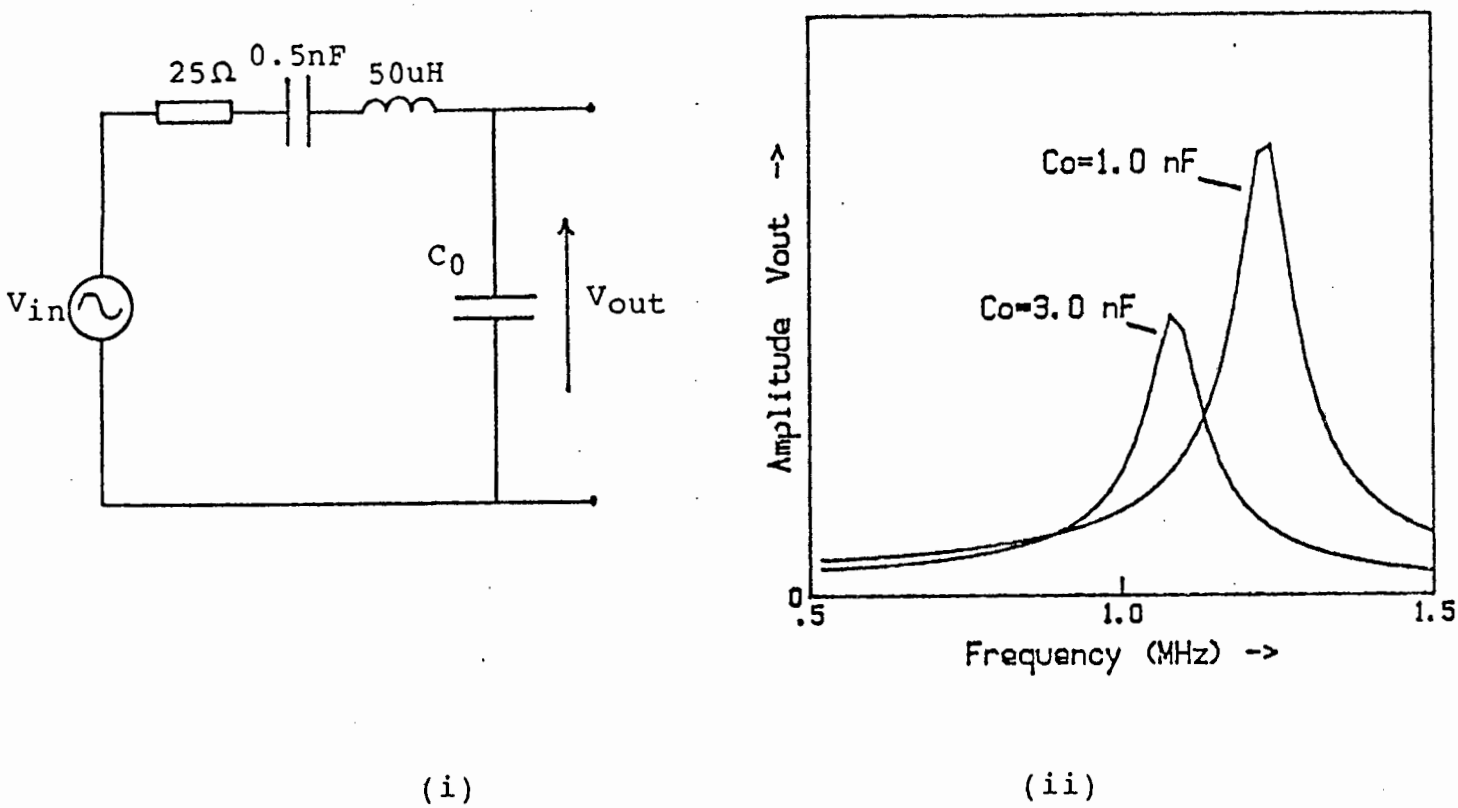

Figure 4.4: (i) Equivalent model of a 1 MHz PZT5A Receiver terminated by an open circuit.
(ii) Frequency responses of model for two values of static capacitance C_o.

Here, the important property common to both responses of Figure 4.4(ii) is that the peak value of each curve does not occur at the series resonance of the RLC branch but instead occurs at the parallel resonant frequency of the circuit, i.e. at f_p. As C_o increases, f_p approaches f_s as shown and a drop in sensitivity is noted. However, if a PZT transmitter is driven by a source of zero output impedance, the peak of its response will occur at series resonance f_s. At this frequency, the impedance of the series RLC branch is a minimum, causing the current flowing through R, and hence the voltage across it, to be a maximum.

4.2.4 Effect of Electrical Impedance Matching and Source Impedance R_o

The frequency response of a PZT5A thickness-mode transducer depends to a large extent on the value of the external

resistance R_o at the electrical port of the transducer. For a transmitter, R_o is the output impedance of the source driving the transducer, whereas in a receiver, R_o is the input impedance of the terminating network. The equivalent models for a piezoelectric transmitter and receiver are analysed for various values of R_o and the corresponding frequency responses are plotted.

(i) Transmitter

The equivalent model of a 1 MHz PZT5A transmitter driven by a voltage source of output impedance R_o is shown in Figure 4.5(i). The frequency response of the model is calculated for two values of R_o, namely R_o=3Ω and R_o=30Ω, and plotted on the same set of axes as shown in Figure 4.5(ii). Note that the radiation resistance R of the transmitter model is 30Ω. Therefore, in the first case, R_o is low compared to R (R_o=R/10) while in the second, it is of the same magnitude, i.e R_o=R.

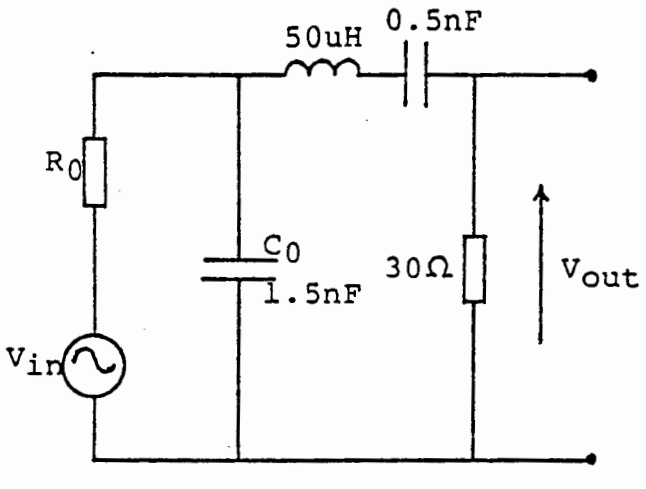

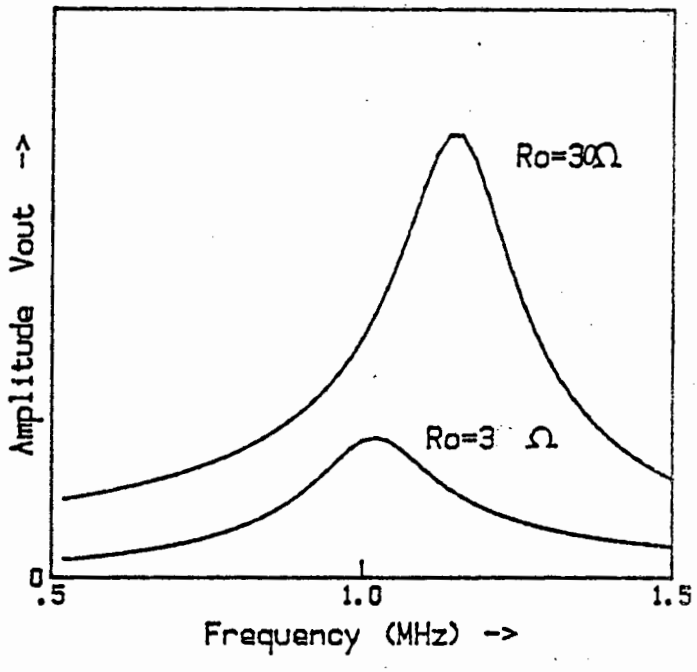

(i) (ii)

Figure 4.5: (i) Equivalent model of a 1 MHz PZT5A transmitter driven by a source of output impedance R_o.
(ii) Frequency responses of model corresponding to two values of R_o.

The two curves above indicate that the value of R_o affects the frequency characteristics of the transducer. As R_o increases, the peak shifts to the right, resulting in an enhancement in bandwidth and efficiency.

(ii) Receiver

The effect of R_o on the frequency response of a 1 MHz PZT5A receiver model operating in water is illustrated in Figure 4.6 below where the response of the model is calculated for two values of R_o. As in the case of the transmitter, the frequency characteristics of the receiver model are also affected by R_o. Here, as the value of R_o increases, the peak of the response shifts to the right towards f_p while the bandwidth decreases and the efficiency is enhanced.

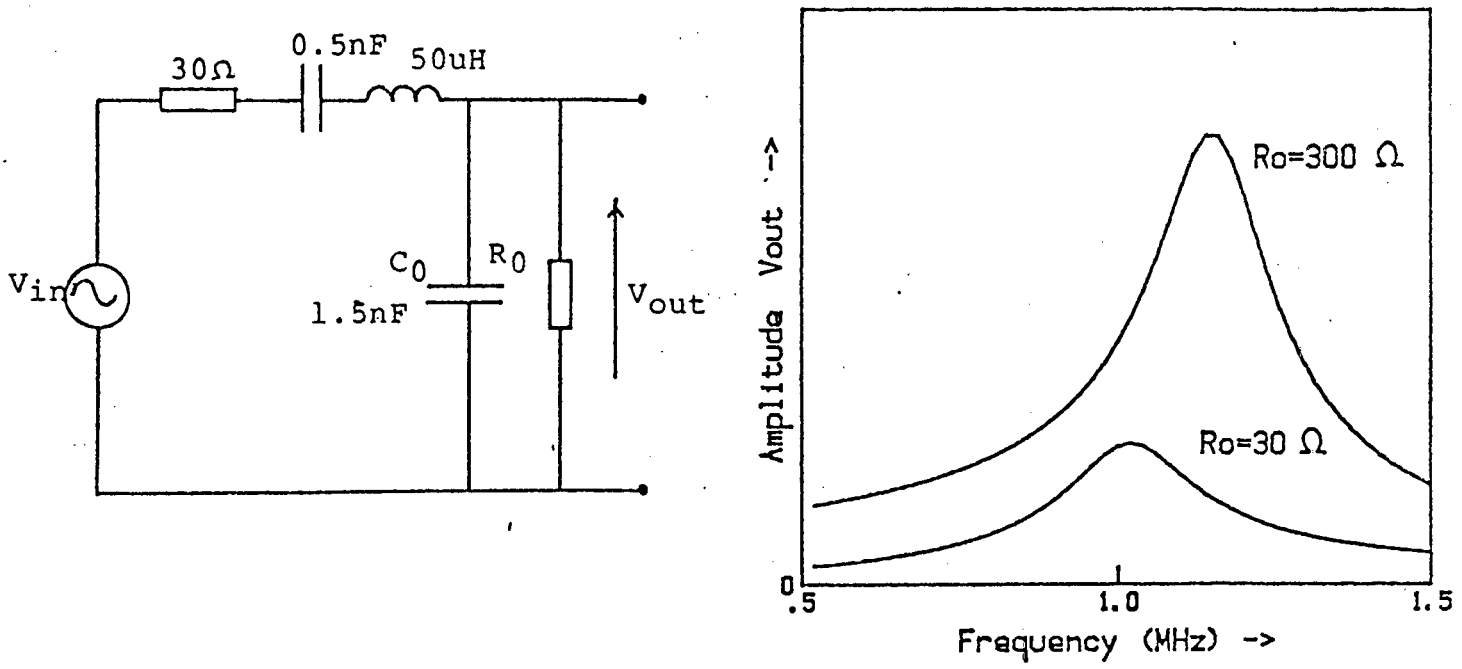

Figure 4.6: (i) Equivalent model of a 1 MHz PZT5A Receiver terminated by a network of input impedance R_o.
(ii) Frequency responses of receiver model computed for two values of R_o.

In practice, the values of R_o and R in a given transmitter or receiver system are fixed by external factors such as the acoustic coupling between the transducer and the loading medium and the terminating impedance at the electrical port of the transducer. If, for matching purposes, these values need to be changed relative to one another, use is made of an impedance transformer placed at the electrical port of the transducer as shown in Figure 4.7.

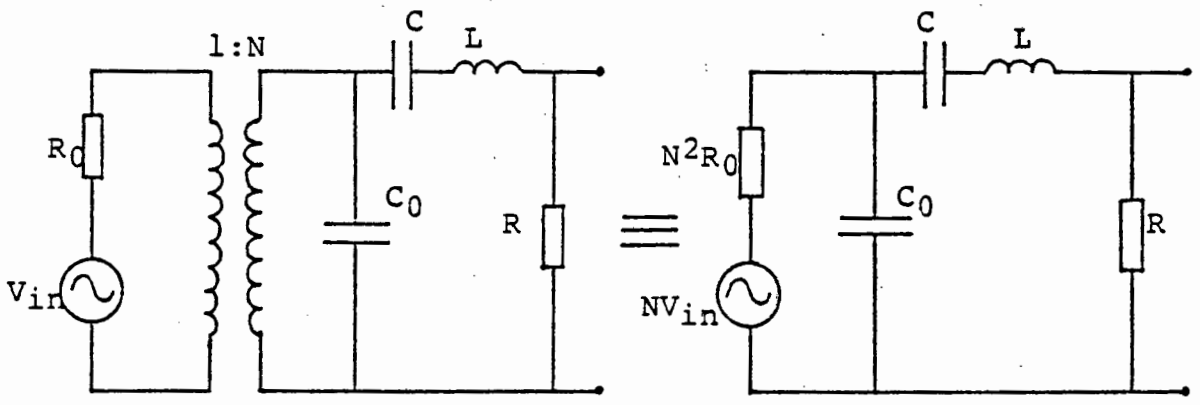

Figure 4.7: Piezoelectric transmitter implemented with an electrical impedance matching transformer. The source impedance R_o is transformed to a new value N^2R_o where N is the transformer turns ratio.

The resistance R_o, when viewed from the secondary side of the transformer, appears as a new resistance N^2R_o, where N is the turns ratio of the transformer. This change in the value of R_o alters the frequency response of the transducer as illustrated by the curves of Figures 4.5 & 4.6. Thus, impedance matching consists of transforming the souce impedance R_o by means of an impedance transformer so that its value, when viewed from the electrical port of the transducer, is such that the transducer exhibits optimum bandwidth and efficiency.

4.2.5 Pulse-Echo and Transmitter-Receiver Systems

Pulse-echo transducers and transmitter-receiver systems are analysed theoretically by considering the responses of the transmitter and receiver models separately. The two curves are then combined to produce the overall response of the transmitter-receiver system. Thus, the bandwidth of a pulse-echo or through-transmission system is determined, firstly, by the bandwidth of the individual responses and, secondly, by their position relative to one another.

In the previous section, it was found that a transmitter driven by a source of output impedance $R_o \approx R$ had its peak at series resonant frequency f_s while a receiver terminated by a resistance $R_o >> R$ had maximum sensitivity near parallel resonance f_p. This is illustrated in Figure 4.8 below where the transmitter and receiver responses are computed from their equivalent models.

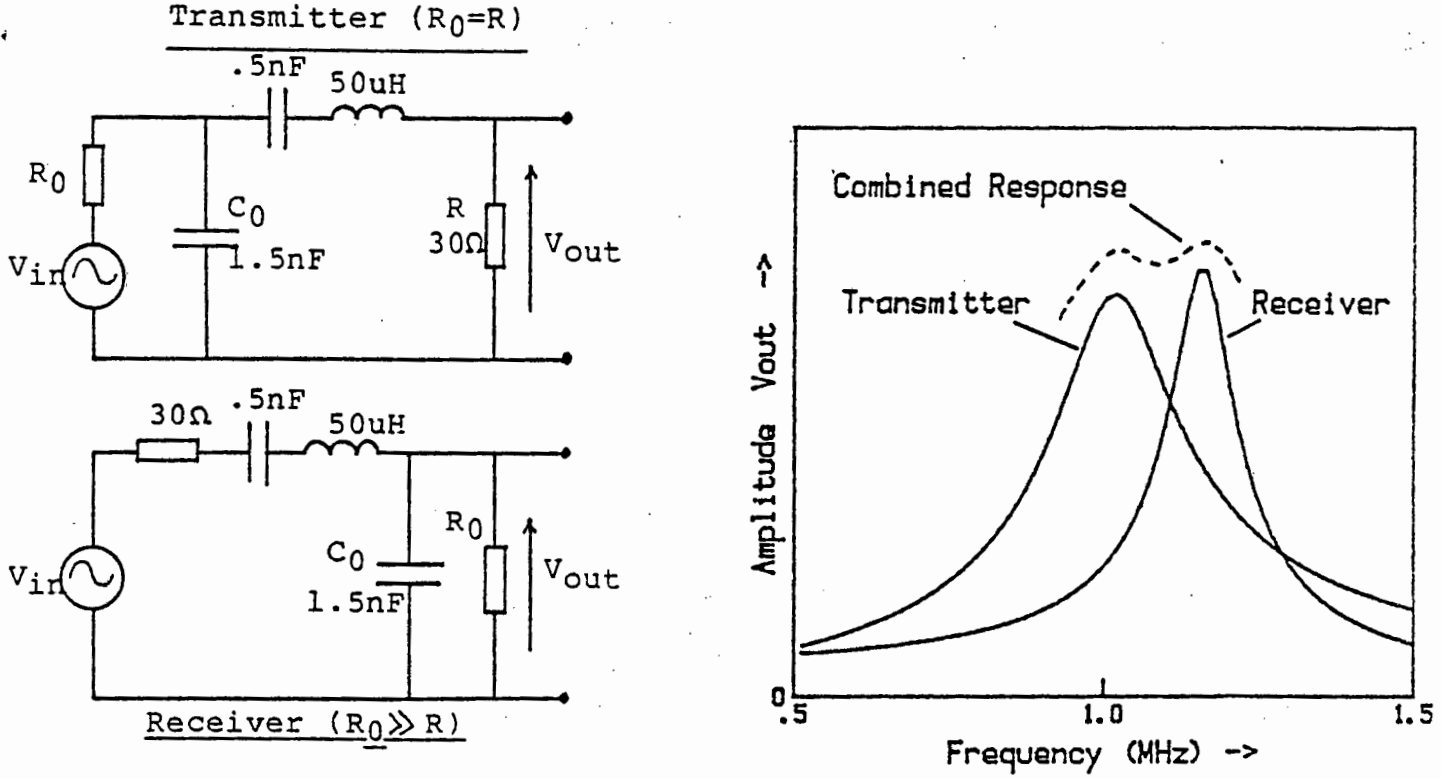

Figure 4.8: Equivalent models for a piezoelectric transmitter and receiver with different electrical matching conditions and their corresponding frequency responses.

If these electrical terminating conditions were to be realised on a pulse-echo or transmitter-receiver system, the overall bandwidth of the system would be broadened by the combined effect of the two individual responses as shown above. In a transmitter-receiver system, the desired electrical termination can be easily implemented since two transducers are used. In pulse-echo mode however, the same transducer is used to transmit and receive, and thus, both modes share the same electrical termination. A technique to overcome this limitation will be described in a later section.

A further analysis of pulse-echo transducers consists of implementing inductive tuning on the transmitter and receiver models. Their responses are then computed and plotted as shown in Figure 4.9 below.

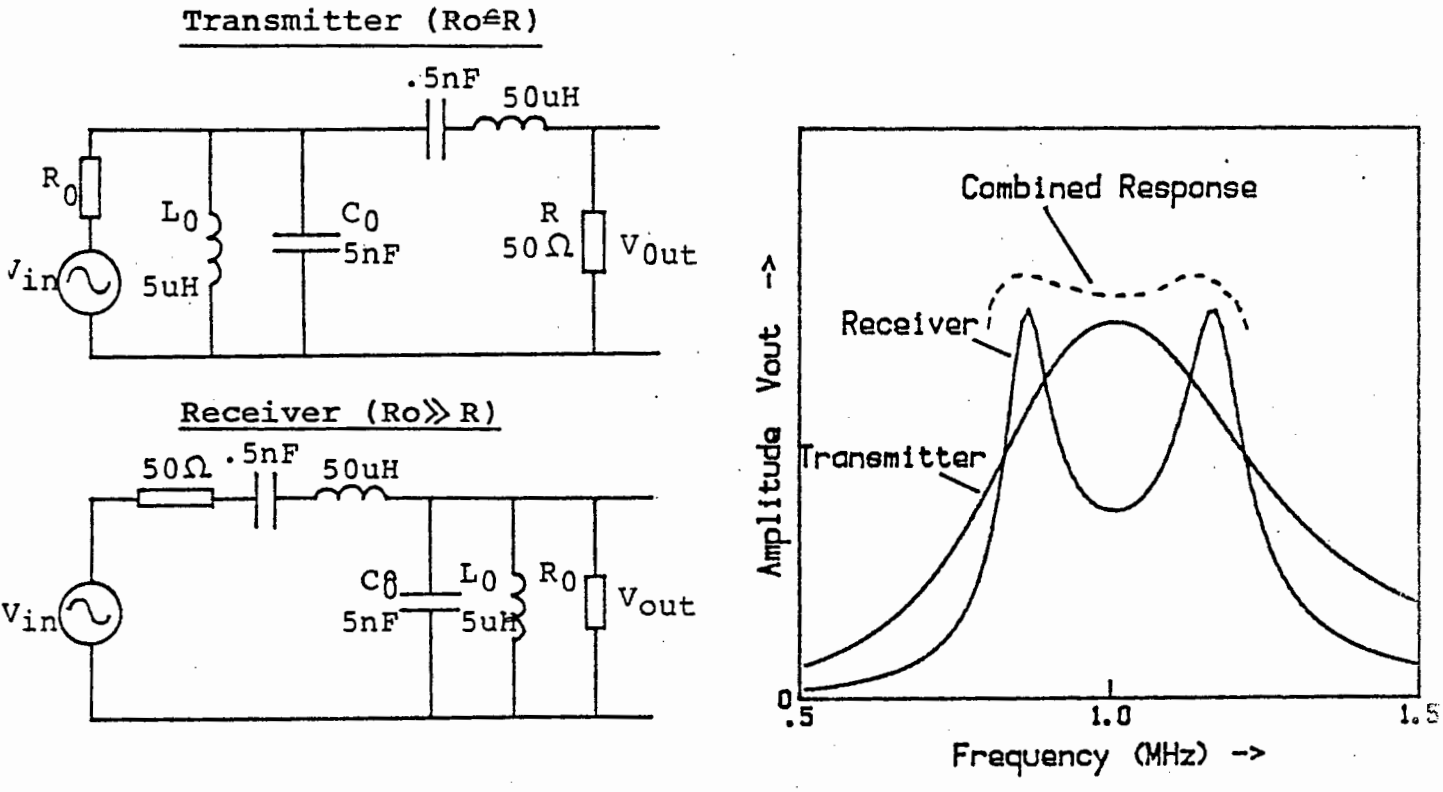

Figure 4.9: Frequency responses of transmitter and receiver models inductively tuned and terminated by different values of R_o at their respective electrical ports.

The transmitter response exhibits a peak at series resonance f_s while the receiver is characterised by a double peak also centred about f_s as shown. The overall response, which is obtained by combining the two curves, will have a larger bandwidth than either of the two responses considered individually. Thus, if these terminating conditions are implemented at the electrical port of a pulse-echo transducer, its bandwidth will be enhanced. A technique which enables these terminating conditions to be realised simultaneously on a pulse-echo transducer is described in the following section.

4.3 Design of a wideband pulse-echo transducer

The analysis of pulse-echo transducers carried out in the previous sections indicates that in order to obtain wide bandwidths, the external resistance R_o at the electrical port of the transducer must be different in the transmit and receive modes. In transmit mode, the condition is that $R_o \approx R$ while in the receive mode $R_o >> R$. To realise these terminating requirements simultaneously, the matching circuit shown in Figure 4.10 below is proposed.

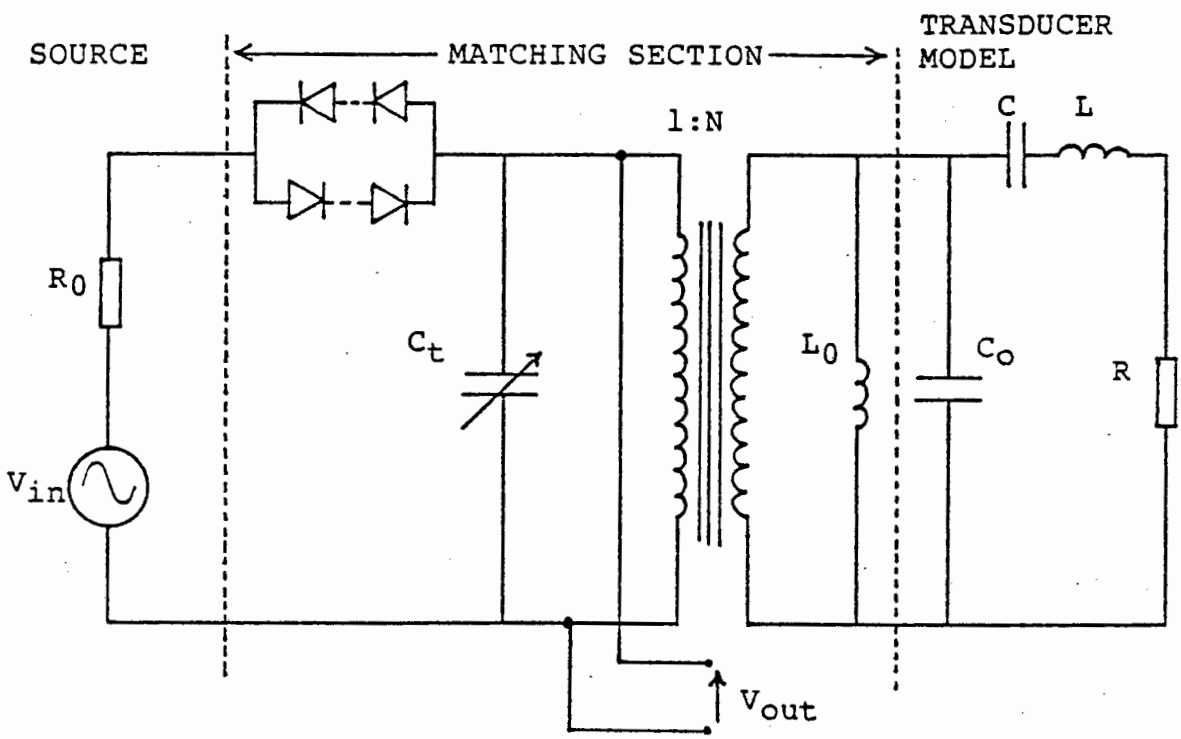

Figure 4.10: Matching circuit configuration to enhance the bandwidth of a pulse-echo transducer.

The main features of this matching section are:

(i) A set of voltage limiting diodes ensures that the transducer, when in the receive mode, sees a high impedance at its electrical port. The diodes act as an open circuit to an echo signal as long as its amplitude lies within the limiting range of the diodes. In the transmit mode however, the driving voltage is well beyond the diodes limiting range and, thus, the diodes become transparent to the source.

(ii) An impedance transformer of turns ratio 1:N is used to match the radiation impedance R to the source impedance R_o so that as a transmitter the transducer is most efficient at series resonant frequency f_s.

(iii) The tuning inductor L_o is chosen so that $L_oC_o=LC$, i.e. $f_p=f_s$. In receive mode, the tuning inductor is responsible for the double-peak feature of the curve of Figure 4.9, thereby enhancing the bandwidth of the pulse-echo transducer. The tuning capacitor C_t is used to smoothen the response of the transducer by virtue of its shifting effect on the peak position as illustrated in Figure 4.4.

4.4 Experimental Results

4.4.1 500 kHz PZT5A Transducer

A PZT5A disk of resonant frequency 500 kHz and diameter 40mm is electrically matched to its source by a technique described in the previous section. The frequency response of the transducer is then determined by means of the apparatus of Figure 3.16 for the case of the transducer operating in pulse-echo mode with both faces loaded by the surrounding water medium. Note that the echo is derived from the reflection of the pulse emanating from only one face of the transducer.

For comparison purposes, the transducer is first calibrated when it is driven directly by a source of 50Ω output impedance, i.e. without the presence of the matching section. Figure 4.11(i) shows the unmatched transducer in circuit with the source and the corresponding echo response over the frequency range of interest. A useful measurement for the design of electrical matching sections is the variation of the actual voltage driving the transducer versus frequency as shown by the "drive" curve. This voltage, measured directly across the transducer terminals, is a function of the matching between the external impedance R_o and the input impedance Z_{in} of the transducer. If at resonance $Z_{in}>>R_o$, the "drive" curve exhibits a slight trough in the resonance region. However, if $Z_{in}<<R_o$, the trough is accentuated since the voltage drop across R_o becomes more significant.

A matching section consisting of a diode pair, a step-up transformer of turns ratio N=2 and a parallel tuning inductor is implemented on the 500 kHz PZT5A transducer. Its frequency response is then measured in pulse-echo mode and plotted as shown in Figure 4.11(ii).

The step-up transformer in this case has the effect of converting the input impedance of the transducer to a lower value on the primary side , i.e. $Z_{in}'=Z_{in}/2^2$. As a result, the trough of the "drive" curve is accentuated as shown, thereby increasing the bandwidth of the echo response. This enhancement in bandwidth is also accompanied by a significant drop in efficiency as shown by the curves above. Note that the amplitude of the source voltage V_{in} is the same for both the matched and unmatched cases.

Table 4.1 lists the performance values of the 500 kHz PZT5A transducer with and without the inclusion of the matching section.

500 kHz PZT5A TRANSDUCER: D=40 mm ; D/λ =13

Performance Parameters	Unmatched	Matched
3-dB Bandwidth (kHz)	45	115
10-dB Bandwidth (kHz)	84	250
Q-value	11.0	4.4
Relative Insertion Loss (dB)	0	11

Table 4.1: Performance values of 500 kHz PZT5A transducer operating in pulse-echo mode in water with and without electrical matching.

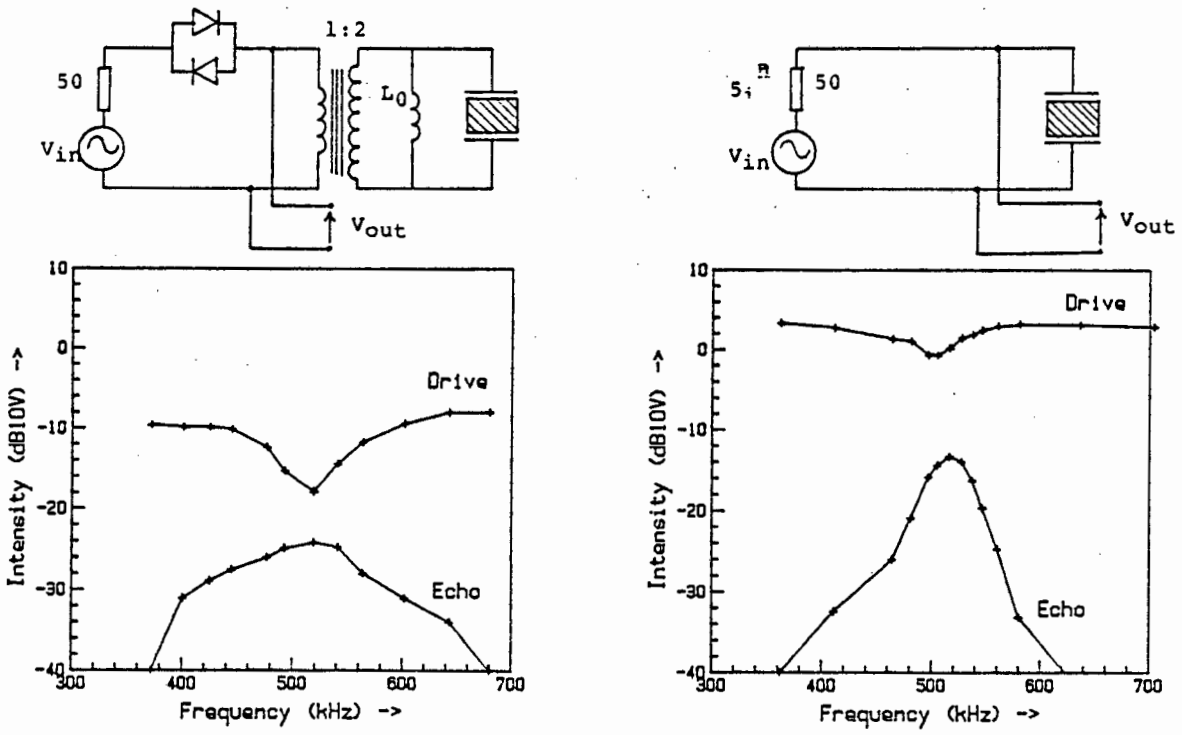

(i) Unmatched (ii) Matched

Figure 4.11: 500 kHz PZT5A transducer calibrated in pulse-echo mode with and without the presence of an electrical matching section.

4.4.2 2-MHz PZT5A Transducers

Four PZT5A disks of resonant frequency 2 MHz and diameters 5, 10, 25 and 40 mm respectively are electrically matched for bandwidth enhancement. The use of four transducers of different diameters but same resonant frequency enables the effect of the D/λ ratio on the frequency characteristics of a pulse-echo transducer to be investigated. The four D/λ ratios are 7, 13, 33, 53. A study of the acoustic coupling as a function of D/λ performed in the previous chapter revealed that a ratio of 13 provided the strongest coupling to the loading medium.

The apparatus of Figure 3.16 is used to determine the frequency responses of the four pulse-echo transducers operating in water. The transducers are first calibrated without matching,i.e. they are driven directly by a 50Ω voltage source. Electrical matching sections consisting of an impedance transformer, a pair of diodes and tuning capacitors and inductors are then implemented on the transducers and their echo responses measured. For each transducer, the components of the matching sections are chosen so as to give maximum bandwidth.

Figures 4.12 to 4.15 show the echo responses of the four transducers for both the matched and unmatched cases. The amplitude of the driving voltage across the transducer is also measured for each case and plotted versus frequency. This measurement is used in conjunction with the unmatched echo response to determine the configuration of the matching section to be used for bandwidth enhancement. In some cases, e.g. with $D/\lambda = 13$, a step-up transformer is used while in other cases, a step-down transformer is more appropriate.

The performance values of the four PZT5A transducers as obtained from the curves of Figures 4.12 to 4.15 are listed in Table 4.2.

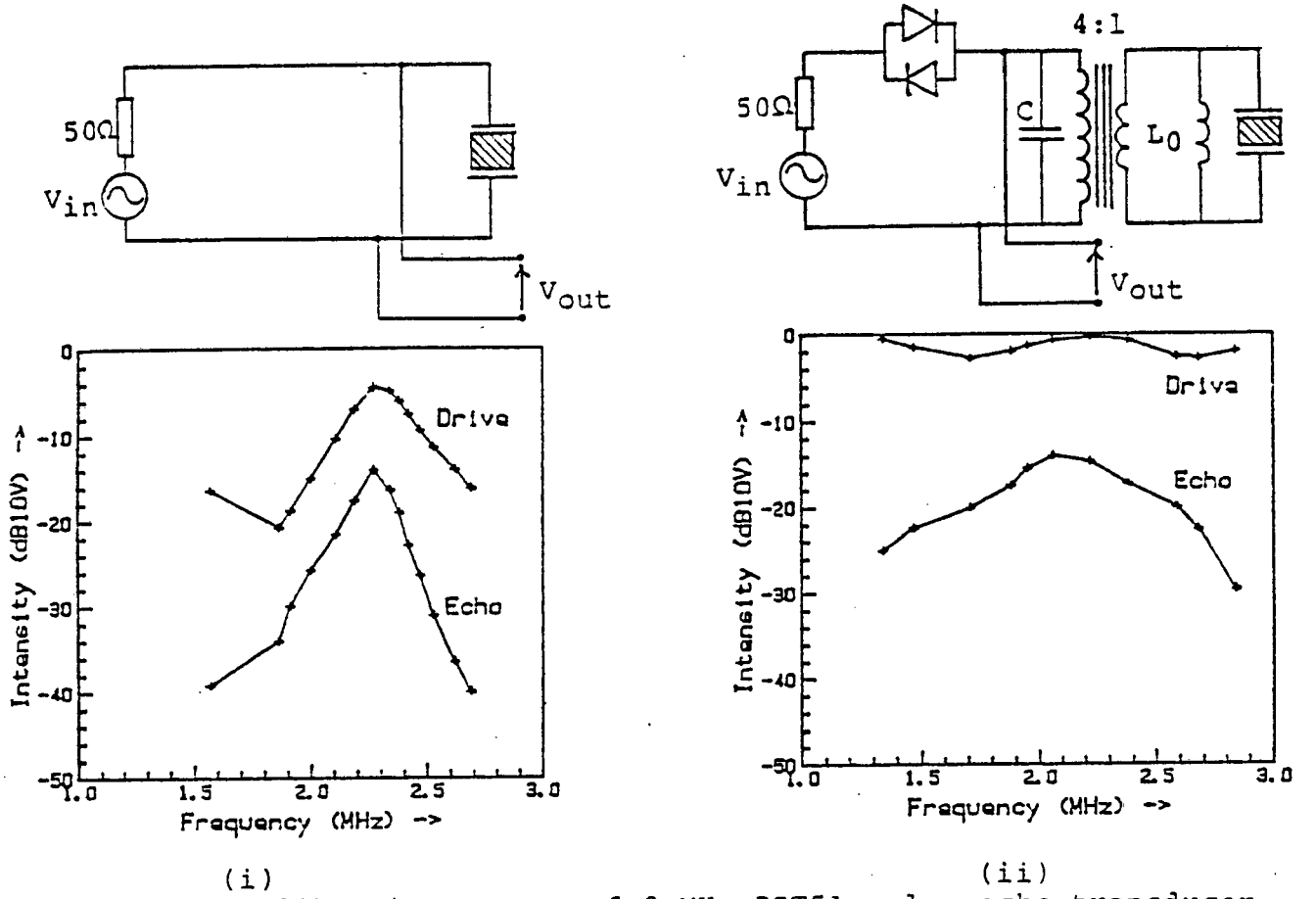

Figure 4.12: Calibration curves of 2 MHz PZT5A pulse-echo transducer with D=40mm and D/λ =53: (i) Unmatched, (ii) Matched.

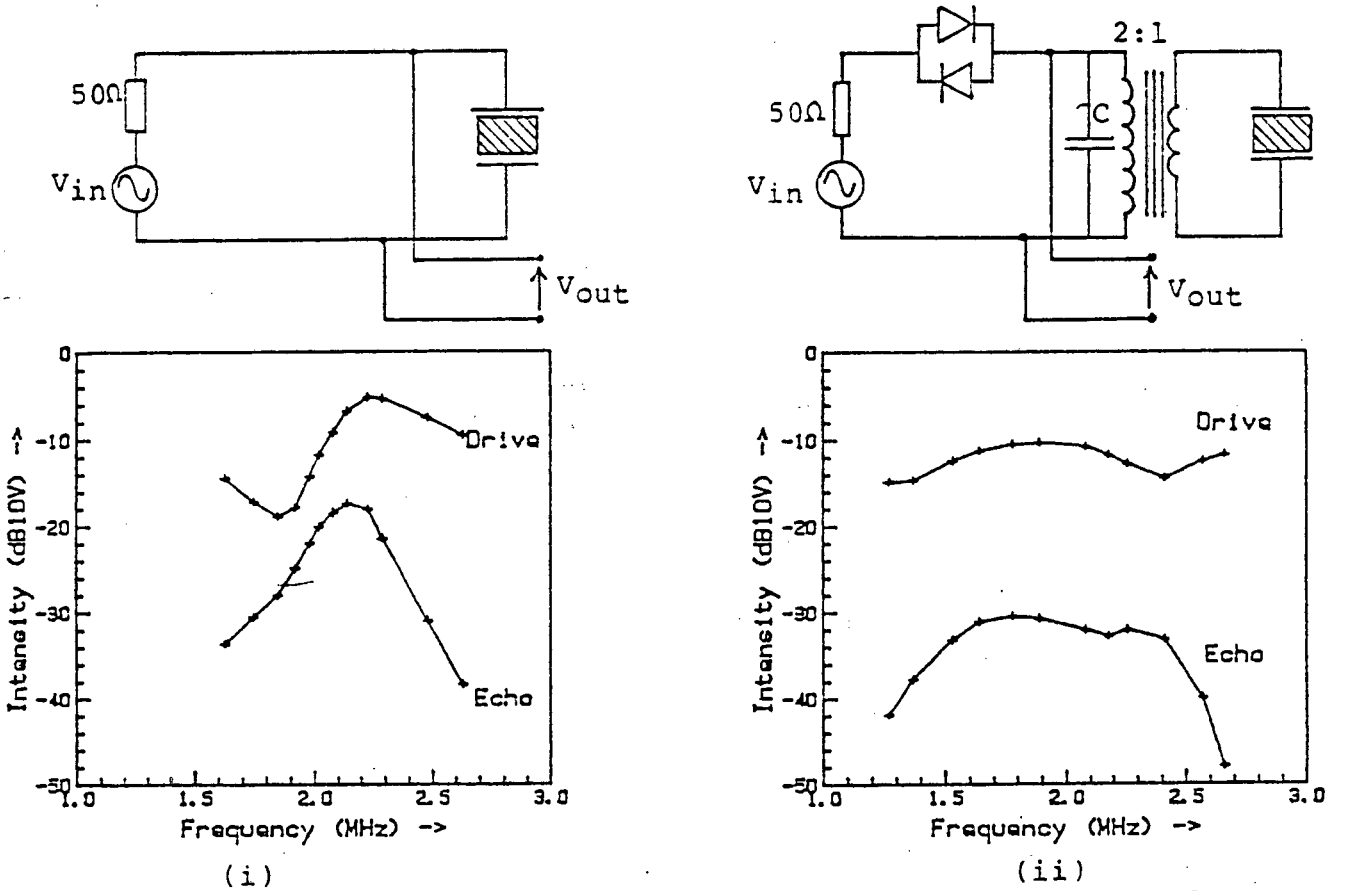

Figure 4.13: Calibration curves of 2 MHz PZT5A pulse-echo transducer with D=25mm and D/λ =33: (i) Unmatched, (ii) Matched.

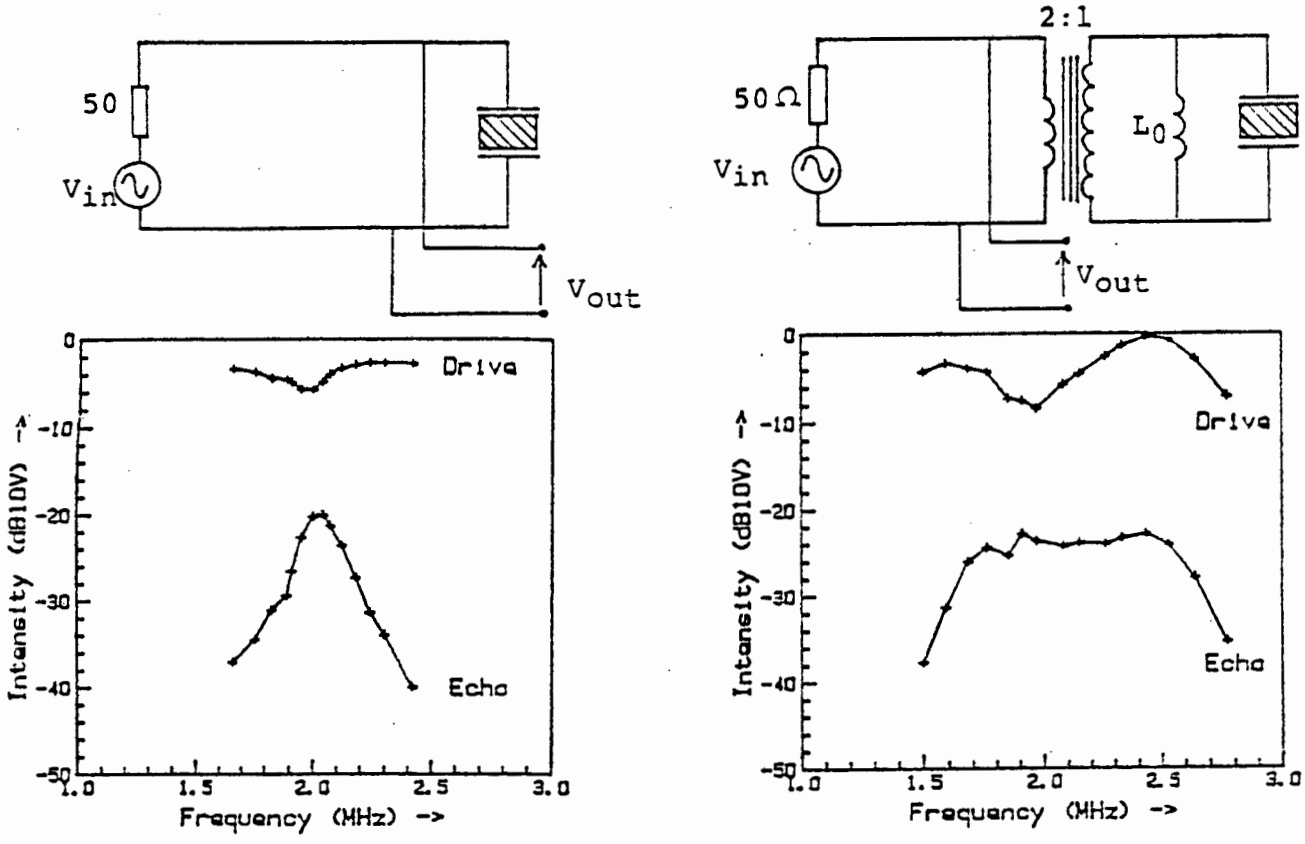

Figure 4.14: Calibration curves of 2 MHz PZT5A pulse-echo transducer with D=10mm and D/λ =13: (i) Unmatched, (ii) Matched.

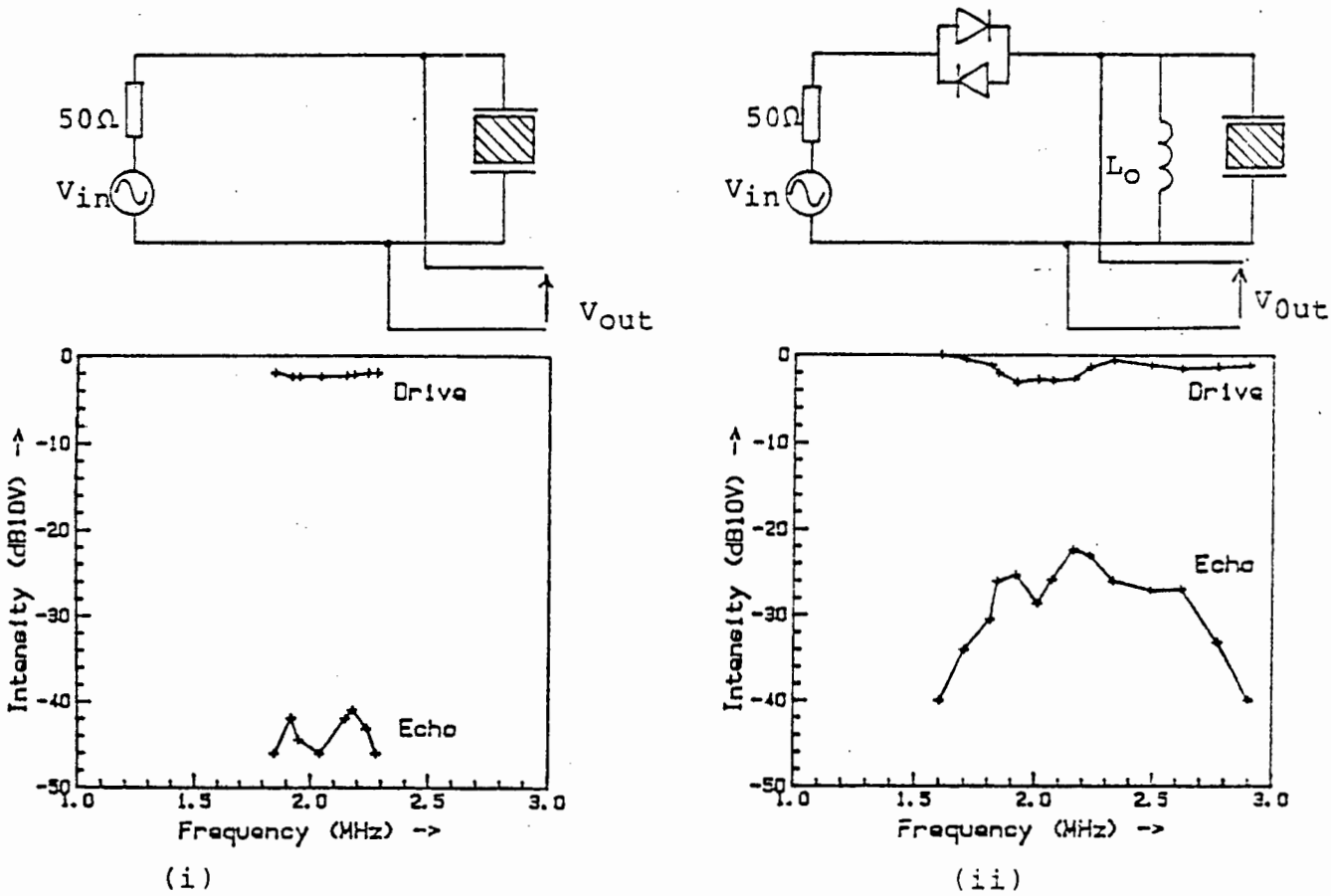

Figure 4.15: Calibration curves of 2MHz PZT5A pulse-echo transducer with D=5mm and D/λ =7: (i) Unmatched, (ii) Matched.

4.5 Discussion of Results

The implementation of electrical impedance matching on a number of PZT5A transducers operating in pulse-echo mode in water produced significant improvements in bandwidth as illustrated by the curves of Figures 4.11 to 4.15. In the case of the 500 kHz transducer, the 3-dB bandwidth increased from 45 kHz to 115 kHz, i.e. by a factor of 2.6, with a corresponding loss of 11 dB in echo amplitude. At 2 MHz, all four transducers showed improved bandwidths, the most notable one being that of diameter 10 mm and D/λ ratio 13 whose 3-dB bandwidth increased from 0.17 MHz to 0.89 MHz with an accompanying loss of 3 dB in echo amplitude.

2-MHz PZT5A TRANSDUCERS

D(mm)	D/λ	Performance Parameters	Unmatched	Matched
5	7	3-dB Bandwidth (MHz)	0.17	0.24
		10-dB Bandwidth (MHz)	-	1.00
		Q-value	11.8	8.3
		Relative Ins. Loss (dB)	0	-18.6
10	13	3-dB Bandwidth (MHz)	0.17	0.89
		10-dB Bandwidth (MHz)	0.38	1.18
		Q-value	11.7	2.2
		Relative Ins. Loss (dB)	0	3.0
25	33	3-dB Bandwidth (MHz)	0.28	0.89
		10-dB Bandwidth (MHz)	0.56	1.24
		Q-value	7.1	2.2
		Relative Ins. Loss (dB)	0	12.7
40	53	3-dB Bandwidth (MHz)	0.16	0.45
		10-dB Bandwidth (MHz)	0.40	1.33
		Q-value	12.5	4.4
		Relative Ins. Loss (dB)	0	0.0

Table 4.2: Performance values of four 2 MHz PZT5A pulse-echo transducers of different D/λ ratios operating in water with and without the presence of an electrical impedance matching section.

The effects of the D/λ ratio on the frequency characteristics of a transducer are demonstrated by the curves of the four 2 MHz transducers as shown in Figures 4.12 to 4.15. In the previous chapter, it was found that the acoustic coupling between a transducer and its loading medium and the directivity of the transducer were functions of D/λ . More important, acoustic coupling showed a maximum at D/λ lying in the region between 10 and 15, while the beamwidth became narrower with increasing D/λ . In support of these observations are the very weak echo responses of the transducer of diameter 5 mm and D/λ 7 given in Figure 4.12 which indicate, firstly, that the acoustic coupling coefficient is low and, secondly, that the beam produced by the transducer is wide and, consequently, characterised by energy spreading.

An important feature of the matching section of the 2 MHz transducer of diameter 10 mm and D/λ ratio 13 is the absence of a pair of voltage limiting diodes. It was observed experimentally that there was no appreciable increase in echo amplitude when the diodes were inserted. This constitutes an important advantage over the other matching sections in that there is no upper limit on the amplitude of the echo signal. In addition, this transducer gives the best trade-off between bandwidth and relative Insertion Loss for the matched case. From Table 4.2 it is found that the bandwidth increases by a factor of 5.2 with an accompanying loss of only 3 dB in echo amplitude. It would thus seem that a PZT5A transducer with a D/λ ratio of 13 operating in the region of 2 MHz produces the best broadband characteristics for pulse-echo applications. Furthermore, it was found experimentally in the previous chapter that a transducer with the same value of D/λ , i.e. D/λ =13, produced the strongest acoustic coupling to the loading medium while its directivity was such that the trade-off between sensitivity to reflector alignment and loss in echo amplitude due to beam spreading was the most satisfactory for applications where the distance between the transmitter and reflector/receiver is typically 15 cm.

The above observations suggest therefore that if a PZT5A transducer is to be constructed for broadband pulse-echo applications in the low megahertz region, the diameter of the transducer must be chosen so that its D/λ ratio lies between 10 and 15. On implementation of an appropriate matching section which makes use of passive components only,the bandwidth of the transducer can be increased significantly with minimum loss in echo amplitude.

CHAPTER 5

ACOUSTIC IMPEDANCE MATCHING ON PZT5A TRANSDUCERS

5.1 Introduction

The radiation efficiency of an ultrasonic transducer operating in a given medium depends, amongst other factors, on the matching between the acoustic impedance of the medium and that of the transducer. In the case of a piezoceramic PZT5A disk radiating in water, the acoustic impedance matching is very poor due to the large difference in the acoustic impedances of the two media. The impedance of PZT5A is about 35×10^6 Pa.s/m while that of water is only 1.5×10^6 Pa.s/m. This large mismatch results in a low coefficient of transmission of energy across the solid-liquid interface. Consequently, the transducer is characterised by a low radiation efficiency and narrow bandwidth.

To overcome this acoustic impedance mismatch between PZT5A and water, use is made of quarter-wave matching transformers which take the form of thin disks of various materials bonded to the radiating surface of the transducer. These act as impedance transformers whose effect is to transform the impedance of the loading medium to a higher value so as to reduce the impedance mismatch between the transducer and the load. Consequently, the radiation efficiency of the transducer is improved, resulting in an enhancement of its bandwidth.

The number of quater-wave layers used in the implementation of acoustic matching usually varies between 1 and 3, depending on the application. Although theoretically one can use an infinite number of lossless layers, in practice this is limited to no more than 3 due to the losses associated with each layer. The choice of material for the various layers is determined from design calculations for wideband multisection quarter-wave transformers [19]. If the calculations yield impedance values which are not obtainable using readily available materials, the matching sections are implemented with materials of impedances closest to the theoretical values.

Two PZT5A transducers of resonant frequencies 500 kHz and 1 MHz respectively are acoustically matched to their water loads by the use of 1 and 2 quarter-wave sections. Their frequency responses are then measured in pulse-echo mode and compared with those obtained without the use of acoustic matching. Electrical impedance matching is then implemented on the two acoustically matched transducers to further improve their responses in terms of bandwidth and efficiency.

An alternative method for determining the frequency response of a pulse-echo transducer is described and evaluated in this chapter. It consists of exciting the transducer with a voltage pulse of a certain duration and sampling the corresponding echo signal. This echo signal can be considered to be the impulse response of the transducer if the driving pulse is sufficiently short. The frequency response of the pulse-echo transducer is then obtained by performing a Fast Fourier Transform (FFT) operation on the sampled echo. The validity of this technique is verified by using it to determine the frequency responses of a number of transducers and comparing them with those obtained by direct measurement. The FFT technique is especially attractive in a computer controlled environment since it lays more emphasis on software whilst simplifying the hardware requirements of the system. In an application where the frequency response of a pulse-echo or through transmission system is used to obtain information about the medium itself, e.g. the measurement of graphite concentration in pulp, the FFT technique has the advantage of yielding the frequency response at one point in time. This is not true of the direct measurement method where the echo amplitude is measured at various frequencies over a finite time interval. Finally, to illustrate an application of the FFT technique, the acoustic absorption of glycerine is investigated as a function of temperature and frequency.

5.2 Theoretical Analysis of Acoustic Impedance Matching

5.2.1 The KLM Model for a Thickness-Mode Piezoelectric Transducer

To understand the principle of acoustic impedance matching on thickness-mode piezoelectric transducers, it is necessary to use an electromechanical equivalent model which consists of a 3-port network - 1 electrical port and 2 acoustic ports. The front and back surfaces of the transducer constitute the 2 acoustic ports, while the metallic electrodes deposited on both surfaces constitute the electrical port. Several such models have been developed, some of which are based on a lumped element configuration such as the Mason model [1], and others using transmission line formalism, e.g. the KLM model [2]. The latter model is used here because it leads more easily to an understanding of the physical processes involved when one or more quarter-wave matching layers are implemented on the radiating surface of the transducer.

Figure 5.1 shows the KLM model for a thickness-mode piezoelectric transducer vibrating in its fundamental mode. A distinguishing feature of this model is the transmission line representation of the mechanical part of the transducer. Each half of the disk is modeled by a section of transmission line of length t/2 and characteristic impedance Z_o equal to the acoustic impedance of the transducer. The electrical port is tapped from the centre of the transmission line via a frequency dependent transformer of turns ratio ø as shown.

In transmit mode, electrical energy is generated at the electrical port by a voltage source placed across the terminals. By the effect of piezoelectricity, a fraction of this energy is converted to mechanical energy in the form of a longitudinal strain wave propagating along the two sections of the acoustic transmission line. The efficiency of the conversion from electrical to mechanical energy and vice versa is dictated by the piezoelectric coupling coefficient k_T^2 which is included in the transformer turns ratio ø.

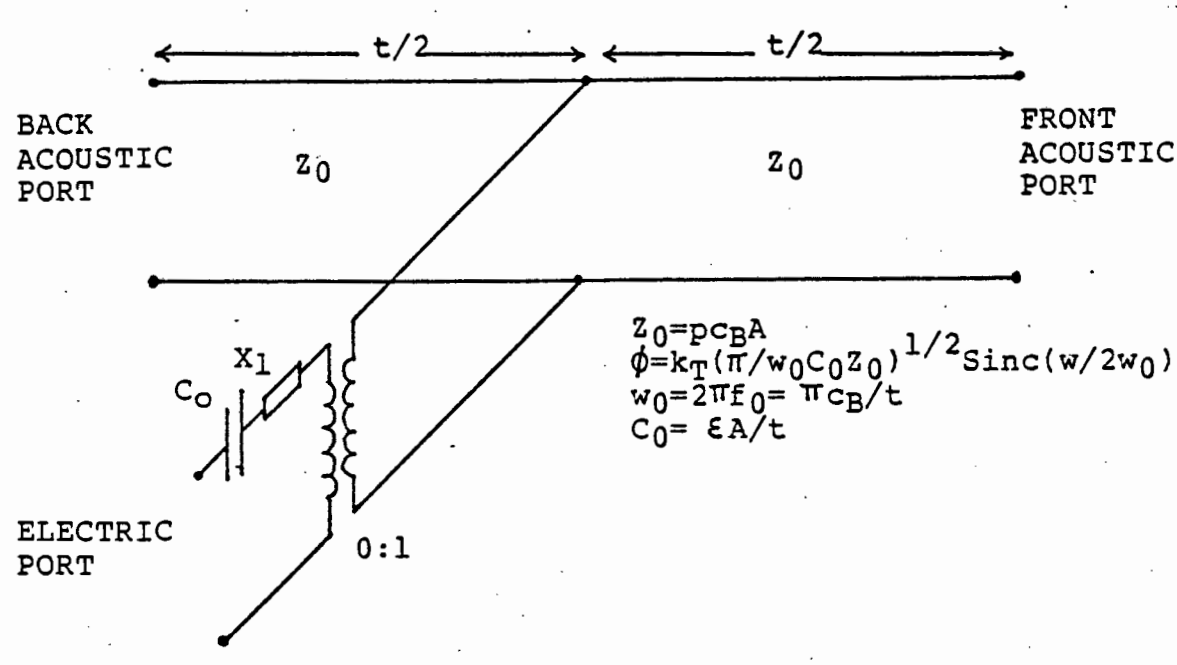

Figure 5.1: KLM equivalent model of a thickness-mode piezoelectric transducer.

The amount of energy which is radiated from both the front and back acoustic ports depends on the acoustic impedances of the two media on either side of the transducer, Z_B and Z_F. From transmission line theory, the intensity transmission and reflection coefficients, T and R, at the end of a lossless transmission line of characteristic impedance Z_o when terminated by a load impedance Z_L are given by:

$$T = 4\, Z_L Z_o/(Z_L+Z_o)^2 \quad \ldots\ldots\ldots\ldots\ldots\ldots \quad (5.1)$$

$$R = [\ (Z_L-Z_o)/(Z_L+Z_o)\ ]^2 \quad \ldots\ldots\ldots\ldots\ldots \quad (5.2)$$

If in the above equations, Z_o is fixed and Z_L is varied, it is found that when $Z_L=Z_o$, the transmission coefficient T reaches a maximum and the reflection coefficient R is reduced to zero. This condition where all the energy propagating down the line is transferred to the load corresponds to a perfect impedance match.

From the transducer model of Figure 5.1, it becomes apparent that for the two acoustic ports to exhibit perfect matching, the two load impedances Z_F and Z_B must be equal to the acoustic impedance Z_o of the transducer. Under these conditions, the

energy radiated from the front and back surrfaces into their respective loads is a maximum and thus the acoustic Q of the transducer, Q_a, is a minimum. Consequently, the bandwidth is a maximum under these loading conditions.

However, in the case of an air-backed PZT5A transducer operating in water, the acoustic impedances Z_o, Z_F and Z_B are fixed parameters whose values are:

$$Z_o = 35 \times 10^6 \text{ Pa.s/m}$$
$$Z_F = 1.5 \times 10^6 \text{ Pa.s/m}$$
$$Z_B = 0 \text{ Pa.s/m}$$

Substituting these values in equation (5.1), the transmission coefficients T_F and T_B at the front and back ports are evaluated as:

$$T_F = 0.16$$
$$T_B = 0$$

These values indicate that the transfer of energy from the transducer to the loading medium and vice versa is very poor. As a result, the acoustic Q-value, Q_a, is high and the transducer is characterised by a low radiation efficiency and a narrow bandwidth.

If a PZT5A transducer is to be constructed with wideband low loss properties for operation in a medium of acoustic impedance similar to that of water, the impedance mismatch at the solid-liquid interface is overcome by the use of one or more quarter-wave matching transformers. These take the form of thin disks of various maaterials bonded to the radiating surface of the transducer. A description of the operation of acoustic quarter-wave transformers in broadbanding applications is given in the next section.

5.2.2 Acoustic Multisection Quarter-Wave Transformers

From transmission line theory, a load impedance Z_L at the end of a section of lossless transmission line of length one quarter of a wavelength and characteristic impedance Z_o assumes

a different value when viewed from the other end of the line. This transformer effect is illustrated in Figure 5.2 where the input impedance Z_{in} of a given network is changed from Z_L to Z_o^2/Z_L when a quarter-wave section of a lossless transmission line of characteristic impedance Z_o is inserted between the input terminals and the network.

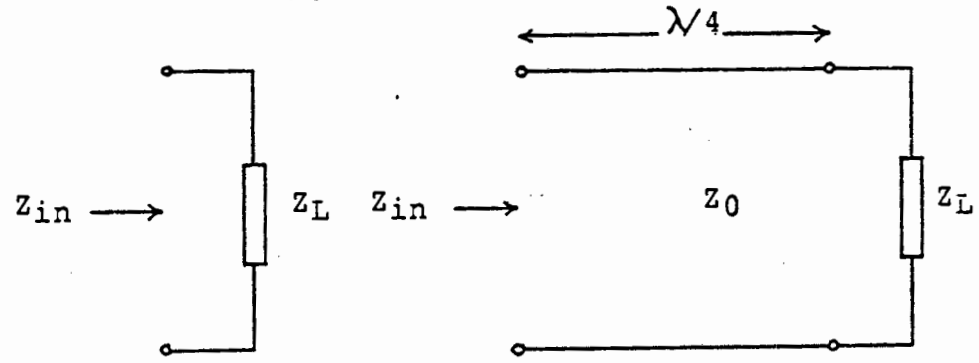

(i) $Z_{in} = Z_L$ (ii) $Z_{in} = Z_o^2/Z_L$

Figure 5.2: Transformer effect of a section of a lossless transmission of length a quarter wavelength and of characteristic impedance Z_o.

The quarter-wave transmission line can therefore be considered as an impedance transformer of turns ratio Z_o/Z_L since Z_{in} can be rewritten as:

$$Z_{in} = (Z_o/Z_L)^2 \cdot Z_L$$

Acoustically, a transmission line takes the form of a block of some material through which propagates an acoustic wave. The acoustic impedance of the material corresponds to the characteristic impedance of the line. Therefore, an acoustic quarter-wave transformer consists simply of a sample of some material whose length corresponds to one quarter of a wavelength at the operating frequency. Standard theory derived for electrical transmission lines can then be applied to their acoustic counterparts for wideband design via the use of multisection quarter-wave transformers.

A general theory of the n-section quater-wave transformer is derived by Collin [19] where he considers two design approaches. The first one consists of providing an impedance match at a single frequency f_o by the use of one or more

transformer sections, each a quarter wavelength long at the operating frequency f_o. A schematic diagram of the n-section transformer terminated by a load Z_L is given in Figure 5.3.

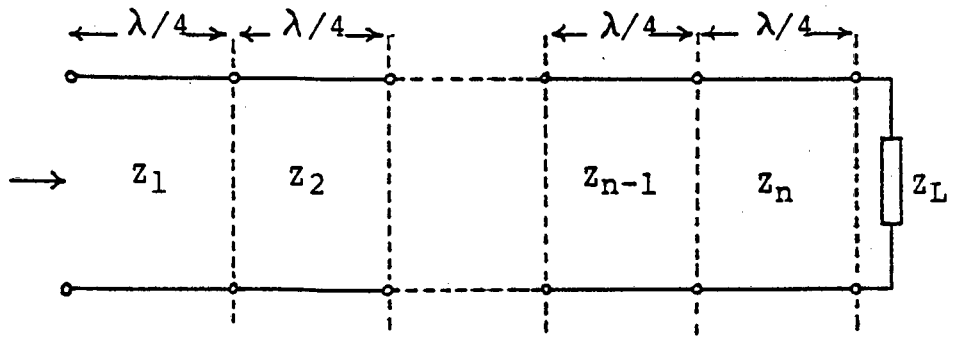

Figure 5.3: Schematic diagram of a n-section quarter-wave transformer terminated by a load impedance Z_L.

The input impedance Z_{in} of the network is determined by successively calculating the resultant impedance at the end of each quarter-wave section, starting from the right. Thus,

$$Z_{in} = \frac{Z_{n-1}^2 Z_{n-3}^2 \ldots\ldots Z_3^2 Z_1^2}{Z_n^2 Z_{n-2}^2 \ldots\ldots Z_4^2 Z_2^2} \cdot Z_L \quad \ldots\ldots(5.3)$$

If for impedance matching purposes, Z_{in} must be made equal to a certain value, the choice of values for $(Z_n, Z_{n-1}, \ldots, Z_1)$ is infinite since there is only 1 equation in n variables. Any one solution satisfying equation (5.3) will perform the required matching at the operating frequency f_o. However, the behaviour of the matching network at frequencies other than f_o varies for every solution $(Z_n, Z_{n-1}, \ldots, Z_1)$, thereby affecting the frequency characteristics of the network.

Collin's second approach to wideband multisection quarter-wave transformers consists of considering not only the impedance match at f_o but also the power loss through the network as a function of frequency. The design technique calls for the transmission line reflection coefficient T of the matching network or, alternatively, the power loss ratio $P_{LR} = 1/(1-T^2)$ to exhibit a Chebyshev response over the desired frequency passband. Larger passbands are obtained by the addition of more transformer sections.

transformer sections, each a quarter wavelength long at the operating frequency f_o. A schematic diagram of the n-section transformer terminated by a load Z_L is given in Figure 5.3.

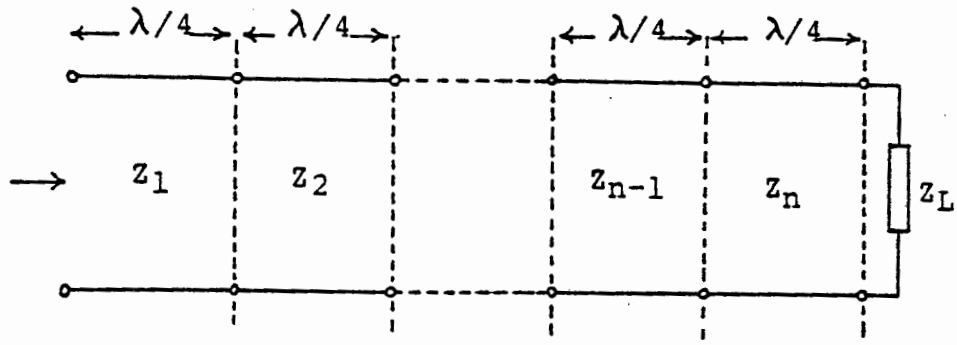

Figure 5.3: Schematic diagram of a n-section quarter-wave transformer terminated by a load impedance Z_L.

The input impedance Z_{in} of the network is determined by successively calculating the resultant impedance at the end of each quarter-wave section, starting from the right. Thus,

$$Z_{in} = \frac{Z_{n-1}^2 \, Z_{n-3}^2 \, \ldots\ldots \, Z_3^2 \, Z_1^2}{Z_n^2 \, Z_{n-2}^2 \, \ldots\ldots \, Z_4^2 \, Z_2^2} \cdot Z_L \quad \ldots\ldots(5.3)$$

If for impedance matching purposes, Z_{in} must be made equal to a certain value, the choice of values for $(Z_n, Z_{n-1}, .., Z_1)$ is infinite since there is only 1 equation in n variables. Any one solution satisfying equation (5.3) will perform the required matching at the operating frequency f_o. However, the behaviour of the matching network at frequencies other than f_o varies for every solution $(Z_n, Z_{n-1}, \ldots, Z_1)$, thereby affecting the frequency characteristics of the network.

Collin's second approach to wideband multisection quarter-wave transformers consists of considering not only the impedance match at f_o but also the power loss through the network as a function of frequency. The design technique calls for the transmission line reflection coefficient T of the matching network or, alternatively, the power loss ratio $P_{LR} = 1/(1-T^2)$ to exhibit a Chebyshev response over the desired frequency passband. Larger passbands are obtained by the addition of more transformer sections.

Table 5.1 gives the matching formulae for 1- and 2-section quarter-wave transformers in terms of the load impedance Z_L and the characteristic impedance Z_o of the transducer. Note that when only one matching section is used, the solution is found from equation (5.3) which has a unique solution for this particular case.

Impedance	Z_1	Z_2
1-section	$Z_o^{1/2}\ Z_L^{1/2}$	-
2-sections	$Z_o^{3/4}\ Z_L^{1/4}$	$Z_o^{1/4}\ Z_L^{3/4}$

Table 5.1: Formulae for calculating the acoustic impedances of matching sections so that the Power Loss ratio of the network exhibits a Chebyshev response.

5.2.3 Design of Matching Sections for PZT5A Transducers

The acoustic impedance mismatch between a PZT5A thickness-mode transducer and its water load can be reduced by the implementation of 1 or 2 quarter-wave sections whose characteristic impedances are determined from Table 5.1. The impedances of the load and the transducer, Z_L and Z_o, required for the calculations are:

PZT5A: $Z_o = 35 \times 10^6$ Pa.s/m
Water: $Z_L = 1.5 \times 10^6$ Pa.s/m

Substituting these values in the expressions of Table 5.1 gives the impedance values of the matching sections as tabulated below:

Impedance	Z_1 ($\times 10^6$ Pa.s/m)	Z_2 ($\times 10^6$ Pa.s/m)
1-section	7.2	-
2-section	16.0	3.3

Table 5.2: Acoustic impedances of quarter-wave matching sections for a PZT5A transducer operating in water.

The impedance values obtained above for the various matching sections ensure that the load impedance Z_L is matched to that

of the transducer Z_o at the resonant frequency f_o. In addition, the power loss ratio of the network for the case of 2 matching layers exhibits a Chebyshev response over a certain frequency passband centred about f_o.

5.3 Experimental Apparatus

5.3.1 Direct Measurement of Frequency Response

The frequency response of a pulse-echo transducer is measured directly by exciting the transducer with a burst of oscillations of variable frequency and recording the echo after reflection from a plate reflector placed in front of the transducer. The 2-way Insertion Loss of the pulse-echo transducer is then calculated relative to the maximum power that can be delivered by the source to a perfectly matched load and plotted versus frequency. Figure 3.16 gives a schematic diagram of the experimental apparatus used for the direct calibration of pulse-echo transducers.

5.3.2 The FFT Technique

An alternative way of determining the frequency response of a pulse-echo or transmitter-receiver system consists of obtaining the impulse response of the system and calculating its Fourier Transform. If a system of transfer function G(jw) is excited by a unit impulse $u(t)=\delta(t)$ so that $U(jw)=1$,, then the output v(t) is the impulse response of the system. In the frequrncy domain, the follwing relationship holds:

$$V(jw) = G(jw) \times U(jw) \quad \ldots\ldots\ldots\ldots\ldots \quad (5.4)$$

If $U(jw) = 1$, then

$$V(jw) = G(jw) \quad \ldots\ldots\ldots\ldots\ldots\ldots\ldots \quad (5.5)$$

Thus, the transfer function of the system can be obtained by calculating the Fourier Transform V(jw) of the impulse response v(t) of the system. A plot of G(jw) versus frequency yields the frequency response of the system.

In certain cases, the hardware requirements for determining the Fourier Transform of a continuous or analogue signal may be difficult to implement. For this reason, the signal is often presented in digital or discrete form by sampling the analogue signal. Its Fourier Transform, known as the Discrete Fourier Transform (DFT), is then computed numerically by software. The relationship between the Continuous Fourier Transform (CFT) and the DFT of the sampled signal is that the DFT is a periodic sampled replica of the CFT as shown in Figure 5.4, provided the sampling time interval is sufficiently short to avoid aliasing.

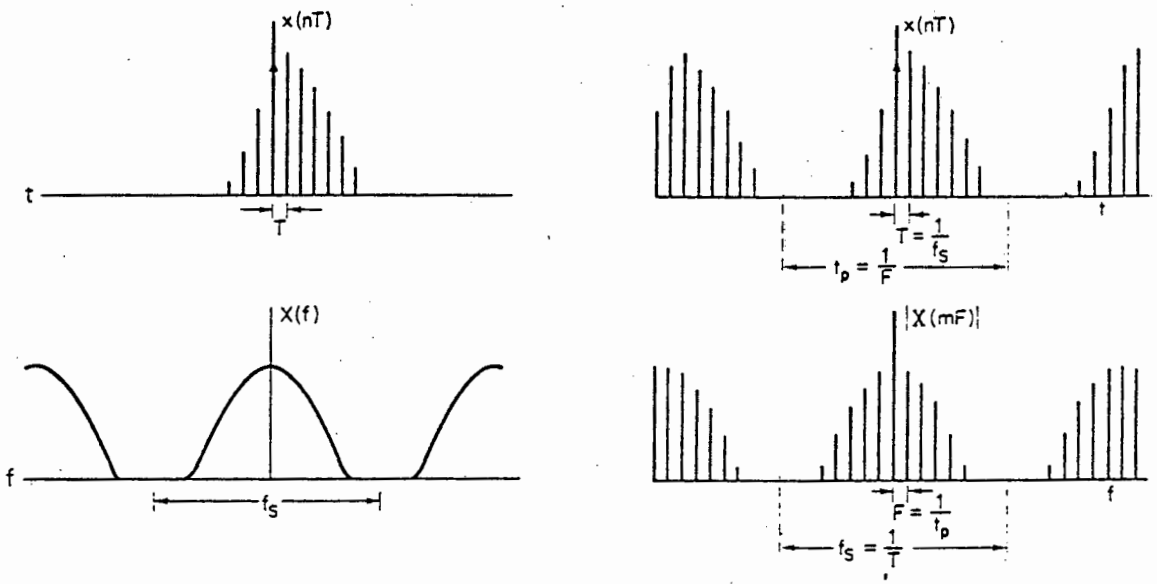

(i) (ii)

Figure 5.4: (i) Continuous Fourier Transform X(f) of non periodic analogue signal x(t).
(ii) Discrete Fourier Transform X(mF) of x(nT), the periodic sampled version of x(t).

Computation of the DFT requires N^2 multiplications for N samples and, therefore, the computation time becomes excessive when N becomes large. For this reason, the Fast Fourier Transform (FFT) algorithm is used which enables one to compute the DFT with a minimum of computation time. Aside from the algorithm itself, the interpretation of the FFT is the same as that of the DFT.

The experimental set-up for determining the frequency response of a pulse-echo transducer by the FFT technique is shown schematically below.

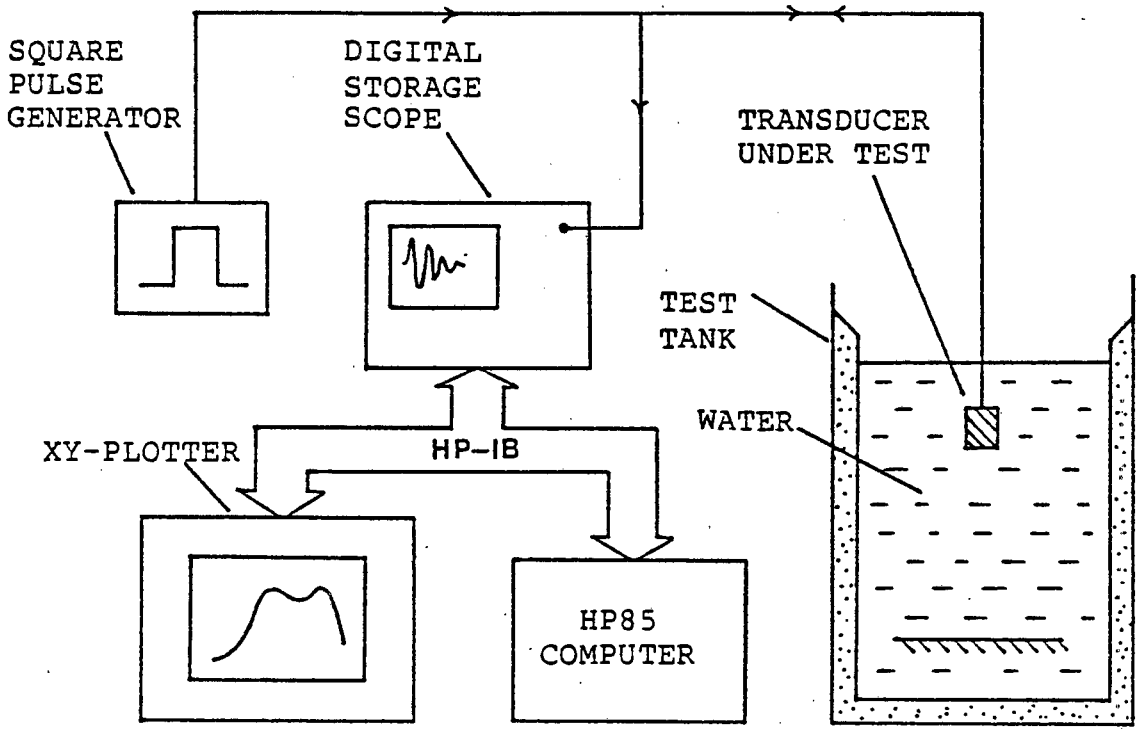

Figure 5.5: Experimental apparatus for determining the frequency response of a transducer by the FFT technique.

The main features of the system are :-

(i) The square-pulse generator produces a periodic square voltage pulse of adjustable duration and frequency. Due to the practical difficulties in generating an impulse, a square pulse of short duration is used instead to excite the transducer under test. The frequency region over which the Fourier Transform of the pulse is flat to within 3 dB is determined by the duration t of the pulse and is approximated by the equation: $f_{3dB} = 1/t$. Thus, a square pulse of duration 1 μs is assumed to have a 3-dB bandwidth of 1 MHz.

(ii) The Digital Storage Oscilloscope plays the dual role of capturing the impulse response of the transducer and thereafter sampling it for transmission to the HP85 computer via the HPIB interface. The sampling rate is controlled by adjusting the time-base setting of the scope. Both the HP85 computer and the scope are equipped with HPIB interfaces and thus the digital samples of the impulse response stored in the scope are transmitted to the computer so that an FFT can be performed on the data.

(iii) The HP85 computer acquires data from the digital storage scope via the HPIB bus and then computes the FFT of the sampled impulse response of the pulse-echo transducer under test. The FFT algorithm used is the one in the HP85 Waveform Analysis Pac [ ], modified slightly to accomodate data file handling. The frequency response of the transducer is then obtained by plotting the FFT of the impulse response.

5.4 Construction of Quarter-Wave Matched Transducers

Two PZT5A transducers, one of frequency 500 kHz and diameter 40 mm and the other of frequency 1 MHz and diameter 20 mm, are each implemented with 1 and 2 quarter-wave matching sections. The transducer assembly used for both transducers is shown schematically in Figure 5.6. The transducer disk is placed in a water-tight perspex casing exposing one face to the loading medium. Wrap-around electrodes on the disks allow connections to be made on one side only. In this exercise, the transducers are air-backed and the loading medium at the front face is water.

(i) 1 Quarter-Wave Matching Section

For a PZT5A transducer operating in water, it was found from section 5.2.3, Table 5.2, that the acoustic impedance of the matching section should be $Z_1=7.2\text{x}10^6$ Pa.s/m. This value is unfortunately not obtainable using common materials - most solids have impedances of above $15\text{x}10^6$ Pa.s/m while epoxies and

plastics have theirs in the region of 2.5×10^6 Pa.s/m as shown in Table 2.4 of Chapter 2.

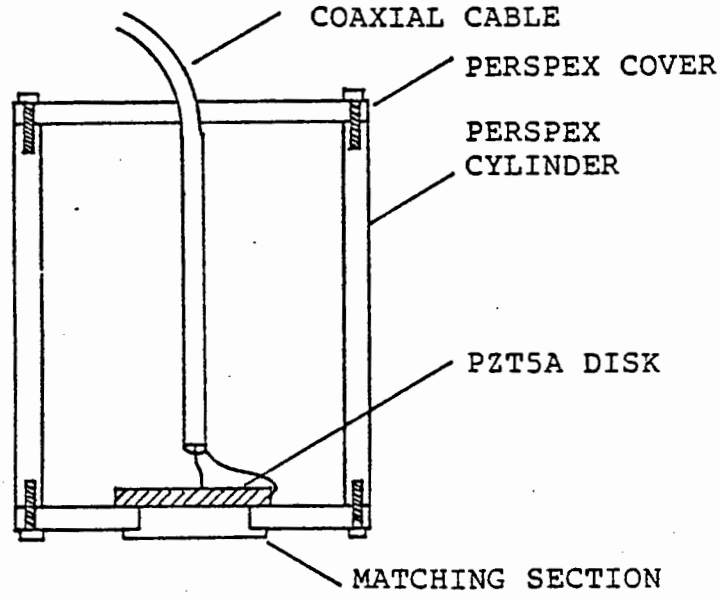

Figure 5.6: Transducer assembly of air-backed PZT5A disk with 1 quarter-wave matching section.

Due to the difficulty in meeting the theoretical impedance requirement for the matching section, a polyester resin made by Fobroglas (FB366) of impedance $Z_1 = 2.9 \times 10^6$ Pa.s/m is used instead. Although its impedance is low, it has the advantage of being in liquid form initially before solidifying on addition of the appropriate hardener. It can be moulded into any shape before being machined to the desired thickness. The acoustic bond between the transducer and the resin layer is also very good.

The thicknesses of the polyester resin matching sections at 500 kHz and 1 MHz are calculated from data given in Table 2.4 as follows:

$$v = (E/p)^{1/2} = 2411 \text{ m/s}$$

At f=500 kHz, $t_1 = v/(4xf) = 1.2$ mm

At f=1 MHz, $t_1 = v/(4xf) = 0.6$ mm

(ii) 2 Quarter-Wave Matching Sections

From Table 5.2, the following impedance values should be used when implementing 2 matching sections on a PZT5A transducer operating in water:

$$Z_1 = 16.0 \times 10^6 \text{ Pa.s/m}$$
$$Z_2 = 3.3 \times 10^6 \text{ Pa.s/m}$$

Again, due to the limited range of acoustic impedances available, the above theoretical values cannot be matched exactly. However, unlike the previous case of 1 matching section, there exists materials in this case whose impedances closely match the theoretival ones. They are aluminium (Z_{Al}=13.7x10^6 Pa.s/m) and polyester resin FB366 (Z_{PR}=2.9x10^6 Pa.s/m) as tabulated in Table 2.4 of Chapter 2.

The thicknesses of the two matching sections are calculated for each transducer from data listed in Table 2.4 as follows

For Aluminium: $v_{Al} = (E/p)^{1/2} = 5128$ m/s
For Polyester Resin: $v_{PR} = 2411$ m/s

At f=500 kHz, Al: $t_1 = v_{Al}/4f = 2.6$ mm
PR: $t_2 = v_{PR}/4f = 1.2$ mm

At f=1 MHz, Al: $t_1 = v_{Al}/4f = 1.3$ mm
PR: $t_2 = v_{PR}/4f = 0.6$ mm

Note that the aluminium section is sandwiched between the PZT5A disk and the polyester resin section, the latter being in contact with the loading medium.

5.5 Experimental Results

5.5.1 1 Quarter-Wave Matching Layer

A 1-MHz PZT5A transducer of diameter 20 mm is initially implemented with a polyester resin matching section of thickness 3 $\lambda/4$ (t_1=1.8 mm) and the corresponding frequency response is measured in pulse-echo mode. The matching section is then gradually machined down to thicknesses of $\lambda/2$

(t_1=1.2 mm) and $\lambda/4$ (t_1=0.6 mm) and calibrated at each step. Transmission line theory states that a $3\lambda/4$ matching section possesses the same transformer characteristics as one of length $\lambda/4$, whereas a $\lambda/2$ section has no transformer effect, i.e. it is transparent to the source. This exercise, besides assessing the effect of 1 quarter-wave layer on the frequency characteristics of a PZT5A transducer, provides experimental verification of the above theoretical predictions.

Figures 5.7 (i) to (iv) show the frequency responses of the 1 MHz transducer with four lengths of matching layer. The 2-way Insertion Loss is measured firstly when the transducer is unmatched as shown in Figure 5.7(i) and then when it is implemented with a matching layer of polyester resin of three different thicknesses, namely $\lambda/4$, $\lambda/2$ and $3\lambda/4$, as shown by the curves of Figure 5.7(ii), (iii) and (iv) respectively. In each case, the electrical capacitance C_o is tuned out by a parallel inductor. The curves obtained with $\lambda/4$ and $3\lambda/4$ matching sections are similar in shape and exhibit bandwidths wider than the two other cases, thereby confirming the theoretical predictions stated above. The performance values of the 1 MHz transducer are listed in Table 5.3 below for the four lengths of matching section.

PZT5A DISK : f_o = 1.0 MHz ; D = 20 mm

Performance Parameters	Matching Condition			
	None	$t_1 = \lambda/4$	$t_1 = \lambda/2$	$t_1 = 3\lambda/4$
3-dB Bandwidth (MHz)	0.10	0.15	0.10	0.15
10-dB Bandwidth (MHz)	0.19	0.28	0.18	0.25
Q-value ($f_o/\Delta f_{3dB}$)	10	6.7	10	6.7
Min. Insertion Loss (dB)	9.0	6.0	8.0	6.5

Table 5.3: Performance values of a 1 MHz PZT5A transducer implemented with quarter-, half- and three-quarter-wave matching sections operating in pulse-echo mode in water.

The implementation of a quarter-wave matching layer made of polyester resin on a 1 MHz PZT5A transducer increased its bandwidth from 0.10 to 0.15 MHz. This is not a remarkable

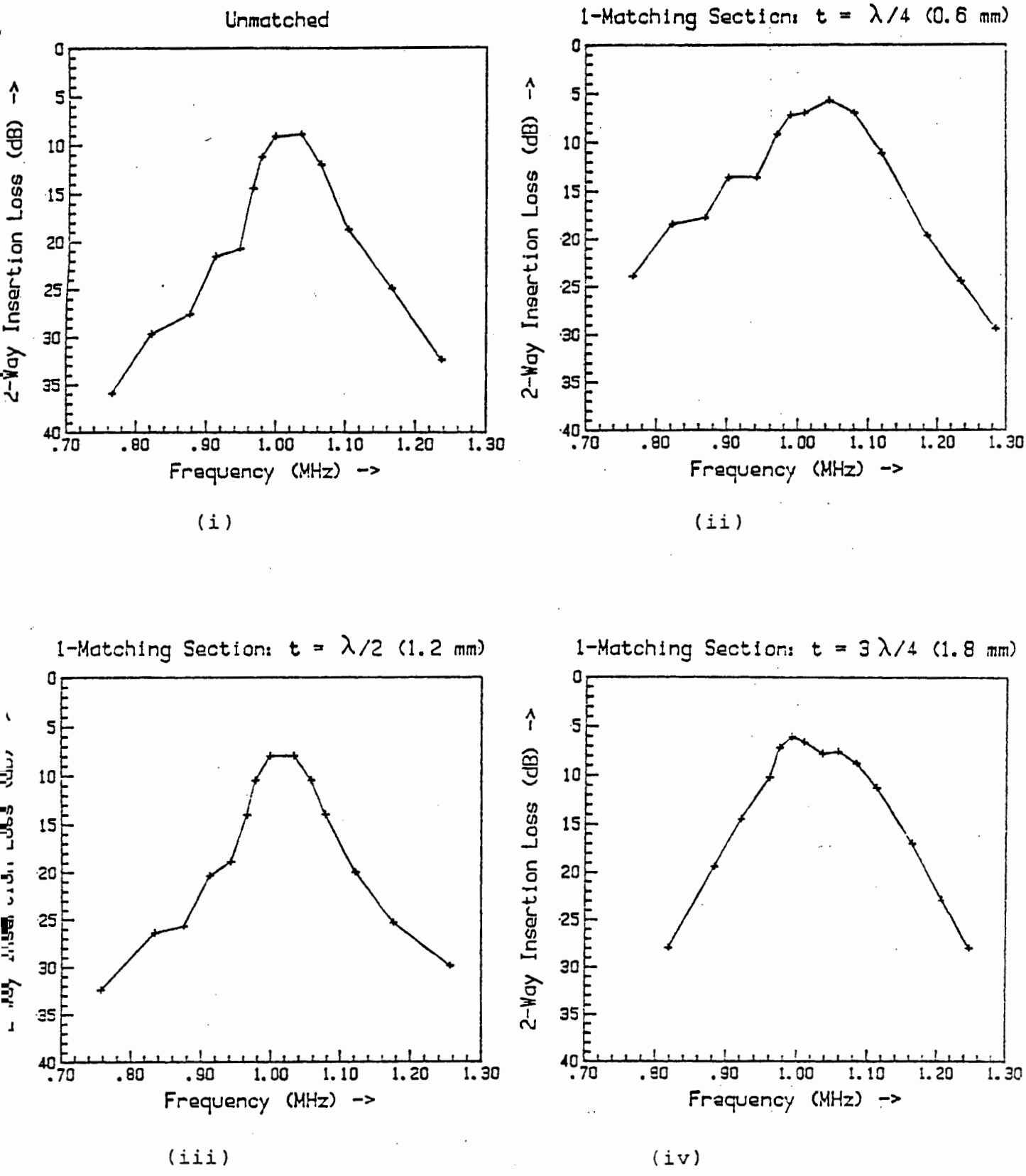

Figure 5.7 : 2-way Insertion Loss curves of a 1MHz PZT5A transducer of diameter 20 mm and D/λ ratio 13 operating in water under 4 different matching conditions: (i) Unmatched (ii) t= λ/4; (iii) t= λ/2; (iv) t=3 λ/4.

improvement and the reason for this may be due to the acoustic impedance being too low. While theory prescribed an impedance of 7.2×10^6 Pa.s/m for the matching section, the impedance used in practice was 2.9×10^6 Pa.s/m due to the unavailability of materials.

At 500 kHz, two PZT5A transducers, one of diameter 40 mm and D/λ ratio 13 and another of diameter 20 mm and D/λ ratio 7, are each implemented with one quarter-wave matching layer of polyester resin of thickness t_1=1.2 mm. Their frequency responses are measured with and without the presence of the matching section and plotted as shown in Figure 5.8(i)-(iv). The effects of the D/λ ratio on the frequency characteristics of an acoustically matched PZT5A transducer are clearly illustrated. The superior performance of the transducer with D/λ =13 confirms the findings of Chapter 3 which indicated that a D/λ ratio lying between 10 and 15 produced the best results in terms of acoustic coupling and directivity. Table 5.4 below lists the performance values of the two transducers as obtained from the curves of Figure 5.8.

PZT5A DISKS : f_o = 500 kHz

Performance Parameters	D=40 mm; D/λ =13 Matching Cond.		D=20 mm; D/λ =7 Matching Cond.	
	None	$t_1 = \lambda/4$	None	$t_1 = \lambda/4$
3-dB Bandwidth (kHz)	50	68	25	45
10-dB Bandwidth (kHz)	80	130	45	80
Q-value ($f_o/\Delta f_{3dB}$)	10	7	20	11
Min. Insertion Loss (dB)	5	5	20	23

Table 5.4: Performance values of two 500 kHz transducer of diameters 20 and 40 mm respectively implemented with one quarter-wave matching section.

Once again, the implementation of a quarter-wave matching section on two 500 kHz PZT5A transducers has not proved very successful - the 3-dB bandwidth increased from 50 kHz to 68 kHz, i.e. by 35% only. This may again be accounted for by the use of a material of too low an acoustic impedance for the matching section.

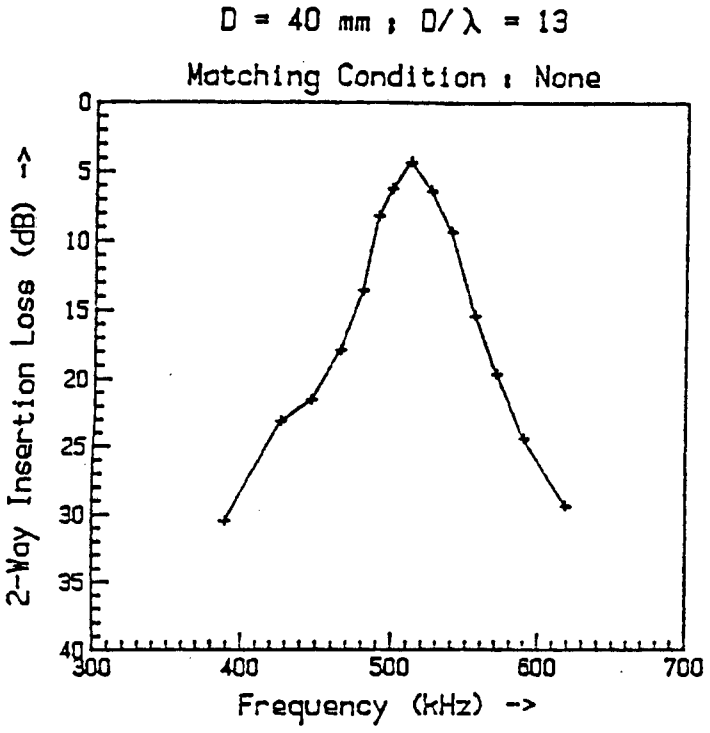

(i)

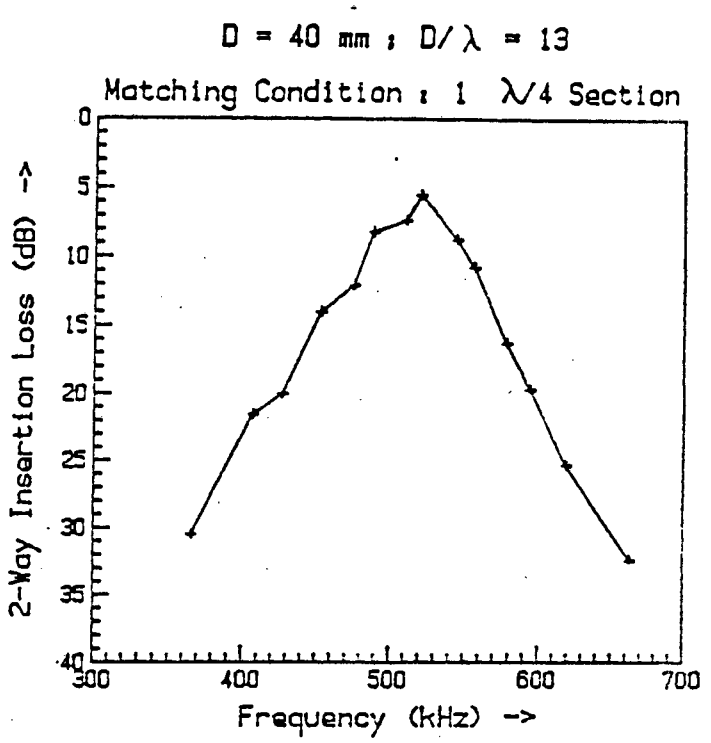

(ii)

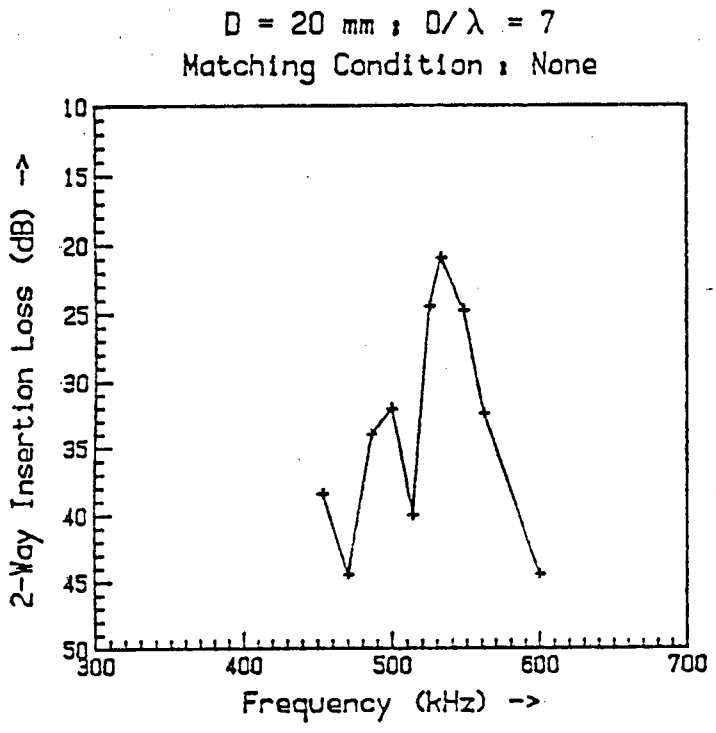

(iii)

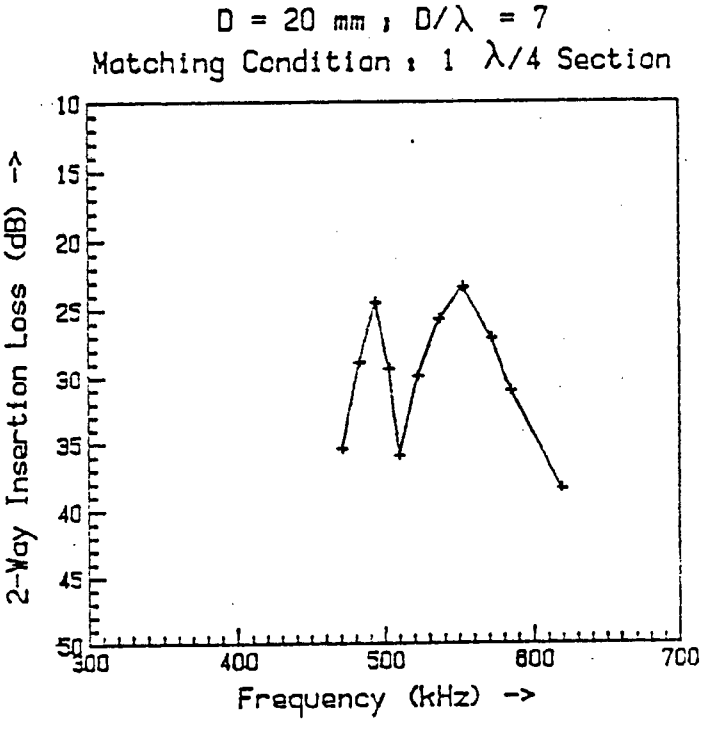

(iv)

Figure 5.8: Calibration curves of two 500 kHz transducers of diameters 20 mm and 40 mm respectively with and without the presence of one quarter-wave matching section.

5.5.2 2 Quarter-Wave Matching Layers

Two quarter-wave matching sections are implemented on two PZT5A transducers of resonant frequencies 500 kHz and 1 MHz respectively according to the design specifications of section 5.4. The transducers are then calibrated by measuring their 2-way Insertion Losses when operating in pulse-echo mode in water.

Figures 5.9 and 5.10 show the frequency responses of the 500 kHz and 1 MHz transducers with and without the presence of the 2 matching sections. The unmatched curves are reproduced here from Figures 5.7(i) and 5.8(i) for comparison purposes. Table 5.5 below lists the performance values of the two transducers as obtained from the curves of Figures 5.9 & 5.10.

Performance parameters	f_o=500 kHz ; D=40 mm Matching Cond.		f_o=1 MHz ; D=20 mm Matching Cond.	
	None	2x $\lambda/4$	None	2x $\lambda/4$
3-dB Bandwidth	50 kHz	54 kHz	0.10 MHz	0.12 MHz
10-dB Bandwidth	80 kHz	138 kHz	0.19 MHz	0.70 MHz
Q-value (f_o/ f_{3dB})	10.0	9.3	10.0	8.3
Min. Ins. Loss(dB)	5.0	7.5	9.0	8.0

Table 5.5: Performance values of 500 kHz and 1 MHz PZT5A transducers implemented with 2 quarter-wave matching sections.

A comparison of the values of Tables 5.4 and 5.5 for the case of the 40mm 500 kHz PZT5A disk implemented with 1 and 2 matching sections indicates that there is no significant improvement in the 3-dB and 10-dB bandwidths. However, the corresponding frequency responses of Figures 5.8(iv) & 5.10(ii) show that the 2-matching layer case is characterised by a double hump, a useful feature in broadband applications.

Flatter frequency responses can be expected for both transducers if, in addition to the two quarter-wave matching layers, electrical matching circuits are implemented at their elctrical ports. The next section looks at the combined use of

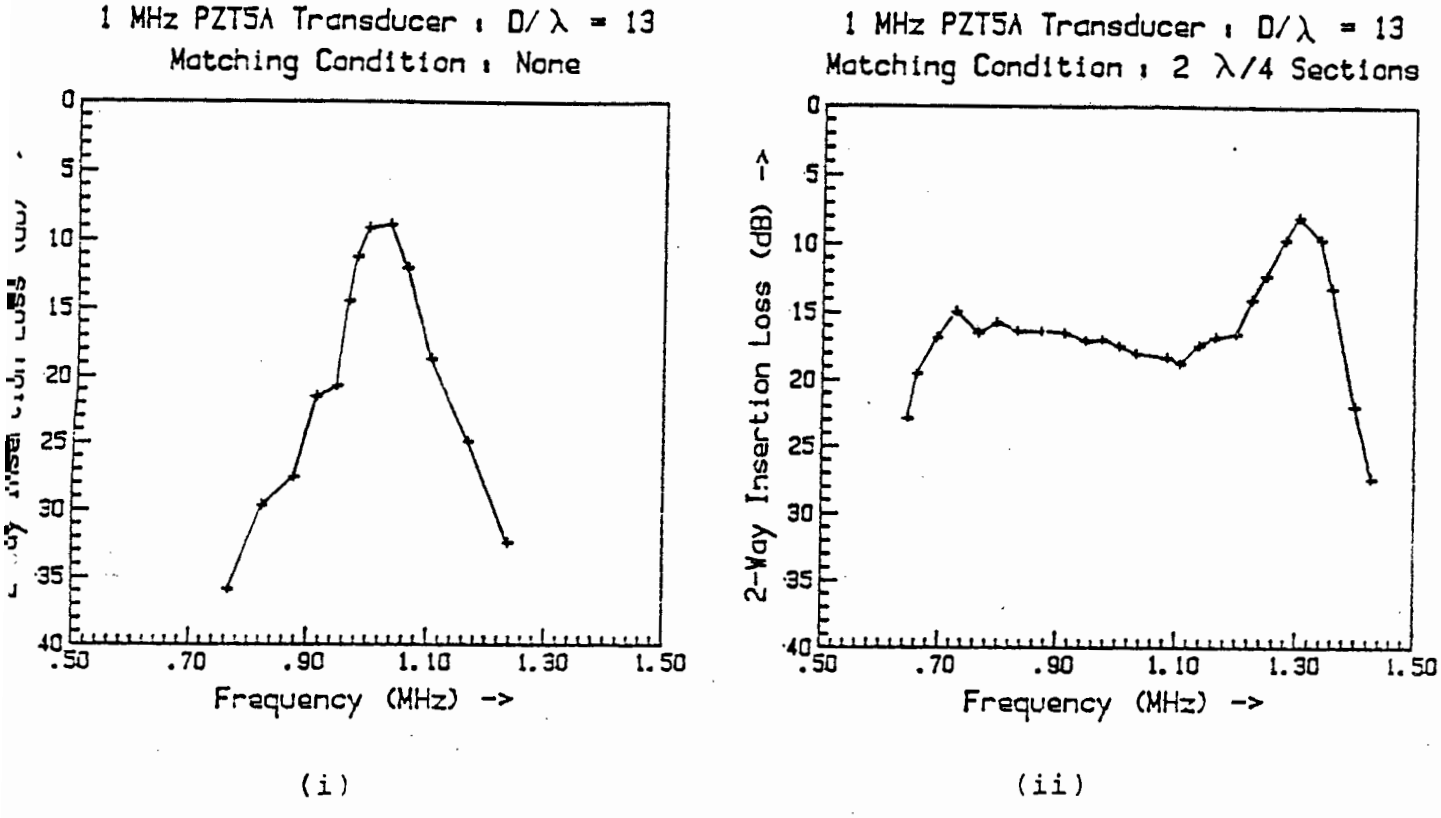

Figure 5.9: 2-way Insertion Loss curves of 1 MHz PZT5A transducer operating in water (i) unmatched; (ii) 2 Quarter-wave matching sections.

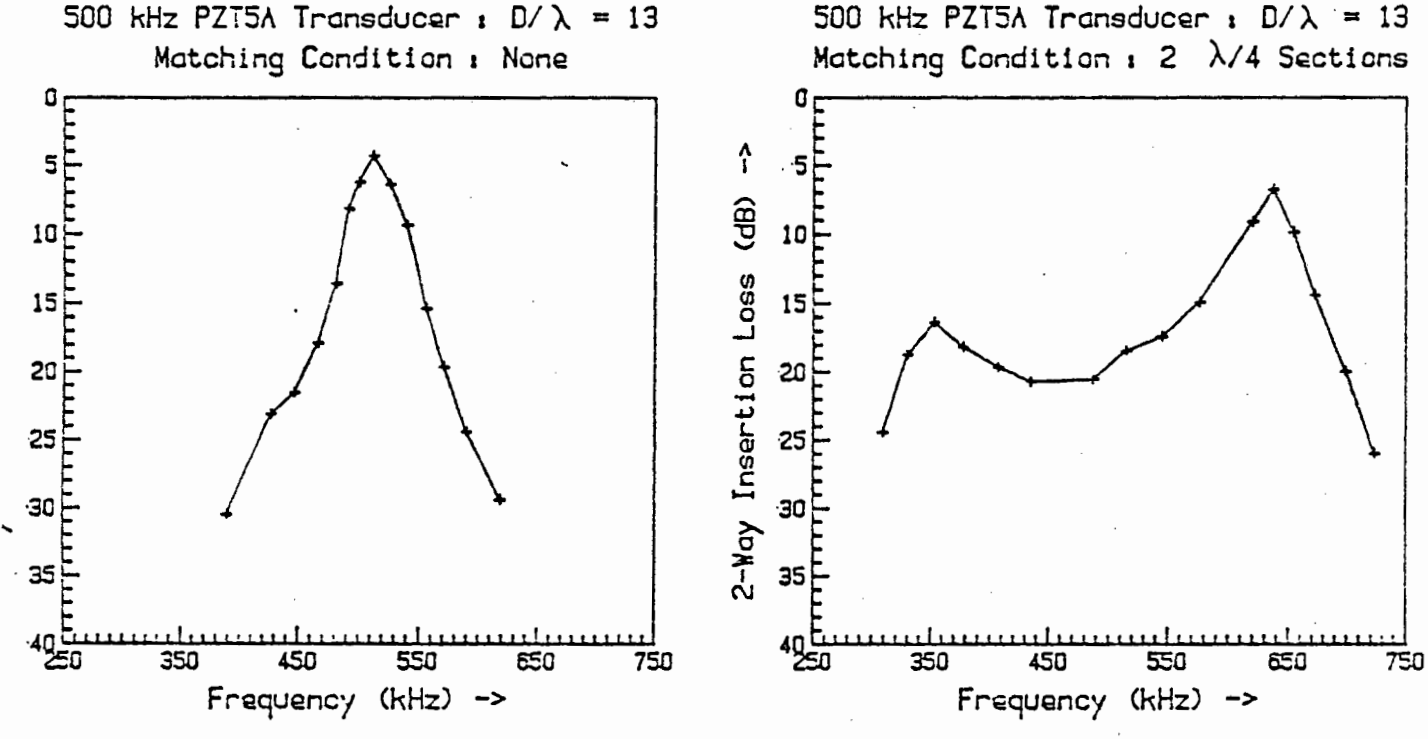

Figure 5.10: 2-way Insertion Loss curves of 500 kHz PZT5A transducer operating in water (i) unmatched; (ii) 2 Quarter-wave matching sections.

electrical and acoustic matching in order to optimise the frequency characteristics of PZT5A thickness-mode transducers.

5.5.3 Combining Electrical and Acoustic Impedance Matching

Further improvements in the frequency characteristics of the 500 kHz and 1 MHz PZT5A transducers used in the previous section are obtained by adding appropriate electrical matching sections at their electrical ports. By inserting an impedance transformer and tuning components between the source and the transducer, the electrical impedance of the transducer is matched to the output impedance R_o of the source (typically 50Ω) at resonance.

Figures 5.11 and 5.12 show the circuit configurations of the two acoustically matched transducers implemented with their respective electrical matching sections and the corresponding frequency responses. Comparing these two curves with those of Figures 5.9 and 5.10, the improvements in flatness achieved by the combined usage of electrical and acoustic matching techniques are made evident. The performance values of the two transducers are given in Table 5.6 below.

Performance parameter	Transducer Specifications	
	f_o=500 kHz ; D=40 mm	f_0=1 MHz ; D=20 mm
3-dB Bandwidth	138 kHz	0.72 MHz
10-dB Bandwidth	354 kHz	0.83 MHz
Q-value ($f_o/\Delta f_{3dB}$)	3.62	1.39
Min. Ins. Loss(dB)	12	16

Table 5.6: Performance values of 500 kHz and 1 MHz PZT5A transducers with combined electrical and acoustic impedance matching.

5.5.4 Using the FFT Technique

In this section, the two PZT5A transducers of section 5.5.3 which were implemented with both acoustic and electrical

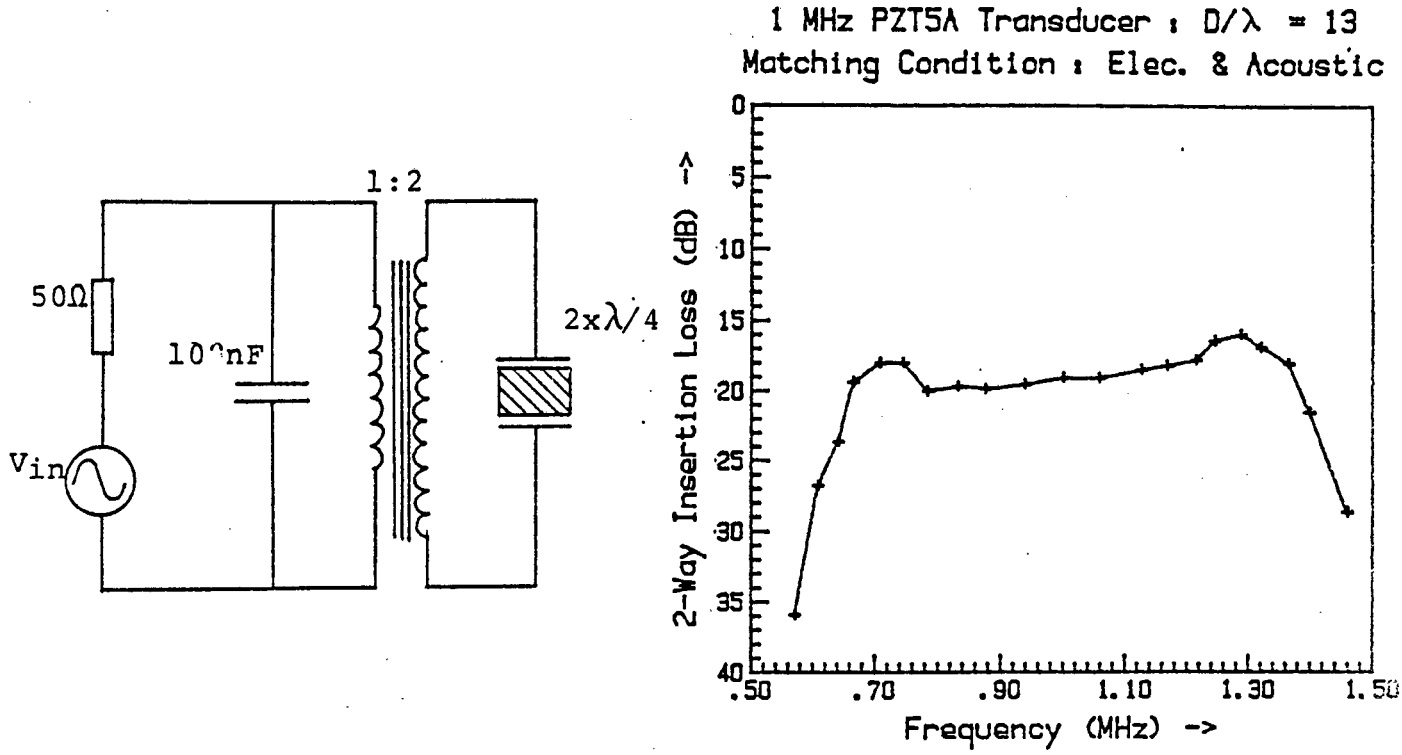

Figure 5.11: 1 MHz PZT5A transducer of diameter 20 mm implemented with acoustic and electrical impedance matching.

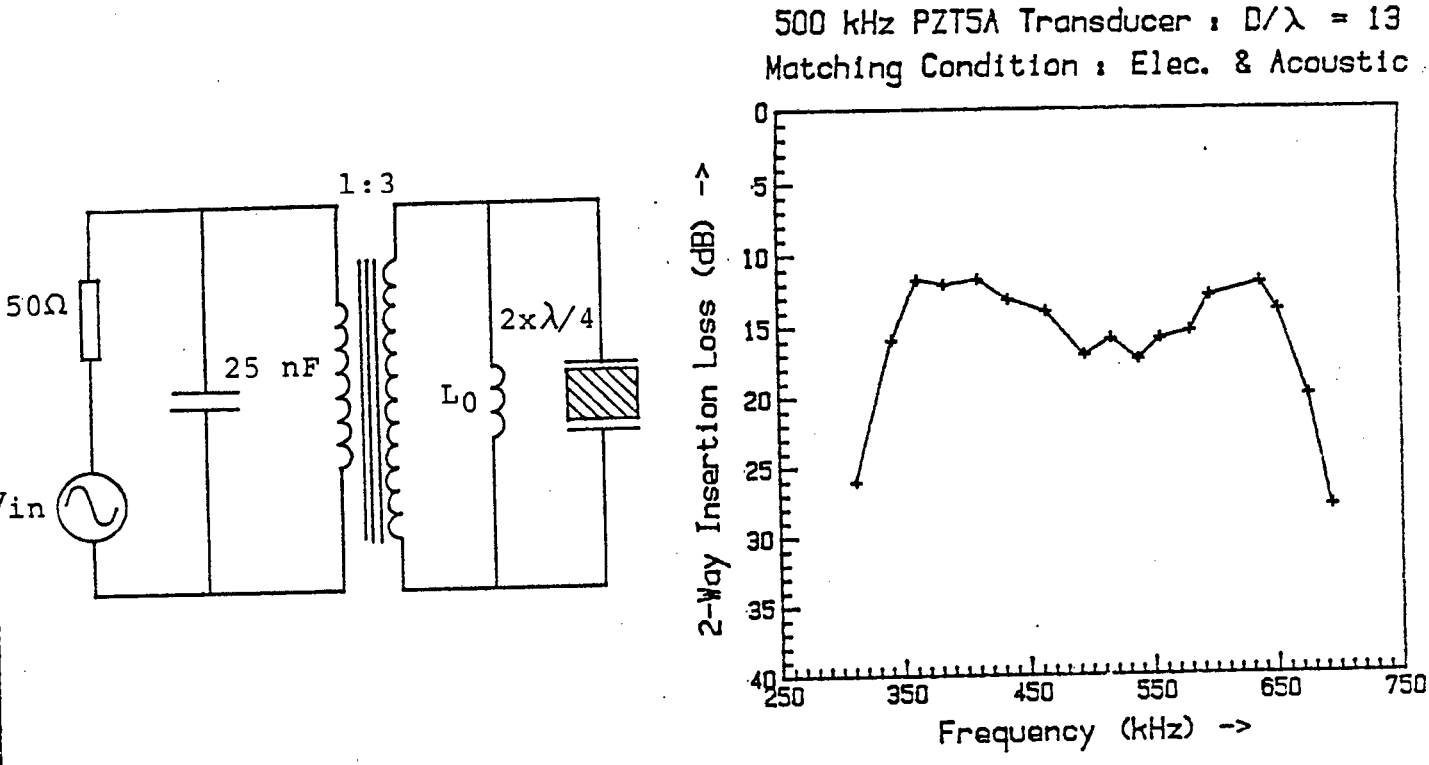

Figure 5.12: 500 kHz PZT5A transducer of diameter 40 mm implemented with acoustic and electrical impedance matching.

matching are calibrated using the FFT technique as described in section 5.3.2. The transducers are excited with square voltage pulses and the corresponding echo responses are stored digitally so that an FFT can be performed on them. The duration of the square pulse in the case of the 1 MHz transducer is 0.25 μs and in the case of the 500 kHz transducer, it is 0.5 μs. This ensures that in each case the frequency response of the input pulse is flat over the frequency region of interest.

Figure 5.13(i) shows the impulse response of the 1 MHz PZT5A transducer as sampled by the digital storage oscilloscope.By performing an FFT on the impulse response, the curve of Figure 5.13 (ii) is obtained. This curve is very similar in shape to that of Figure 5.11 (ii) which is the frequency response of the transducer measured directly. This indicates therefore that the FFT technique provides a viable method of determining the frequency response of a pulse-echo transducer. This is further confirmed by the FFT curve of the 500 kHz transducer in Figure 5.14 (ii) which is again in good agreement with that of Figure 5.12 (ii).

5.5.5 An Application of the FFT Technique

To demonstrate the use of the FFT technique in an application such as the the measurement of ultrasound attenuation through a medium, a simple experiment is devised whereby the attenuation characteristics of glycerine are investigated as functions of temperature and frequency. The experiment is based on the use of a 1 MHz PZT5A transducer which exhibits a flat frequency response over a bandwidth of 0.72 MHz in water when operating in pulse-echo mode. It is assumed that the attenuation of ultrasound in water is negligible. Therefore, when the frequency response of the same transducer is measured in glycerine, it is assumed that any change in the shape of the response is a result of the attenuation characteristics of the medium.

Figure 5.15 (i) shows the frequency responses of the transducer operating in pulse-echo mode in water at temperatures of 5^{o}C and 20^{o}C. The similarity between the two curves establishes

1 MHz PZT5A TRANSDUCER

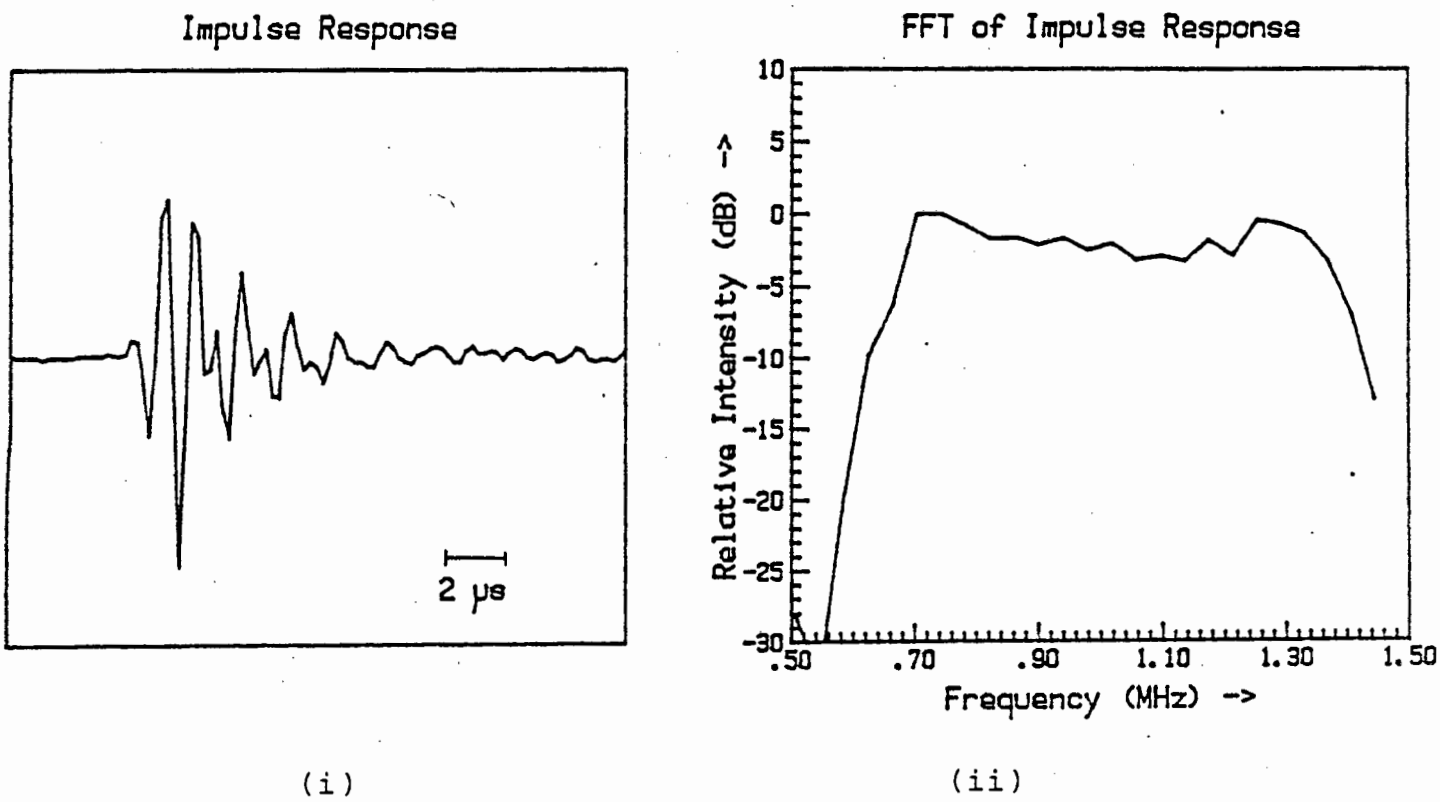

Figure 5.13: (i) Impulse Response of pulse-echo transducer
(ii) FFT of Impulse Response

500 kHz PZT5A TRANSDUCER

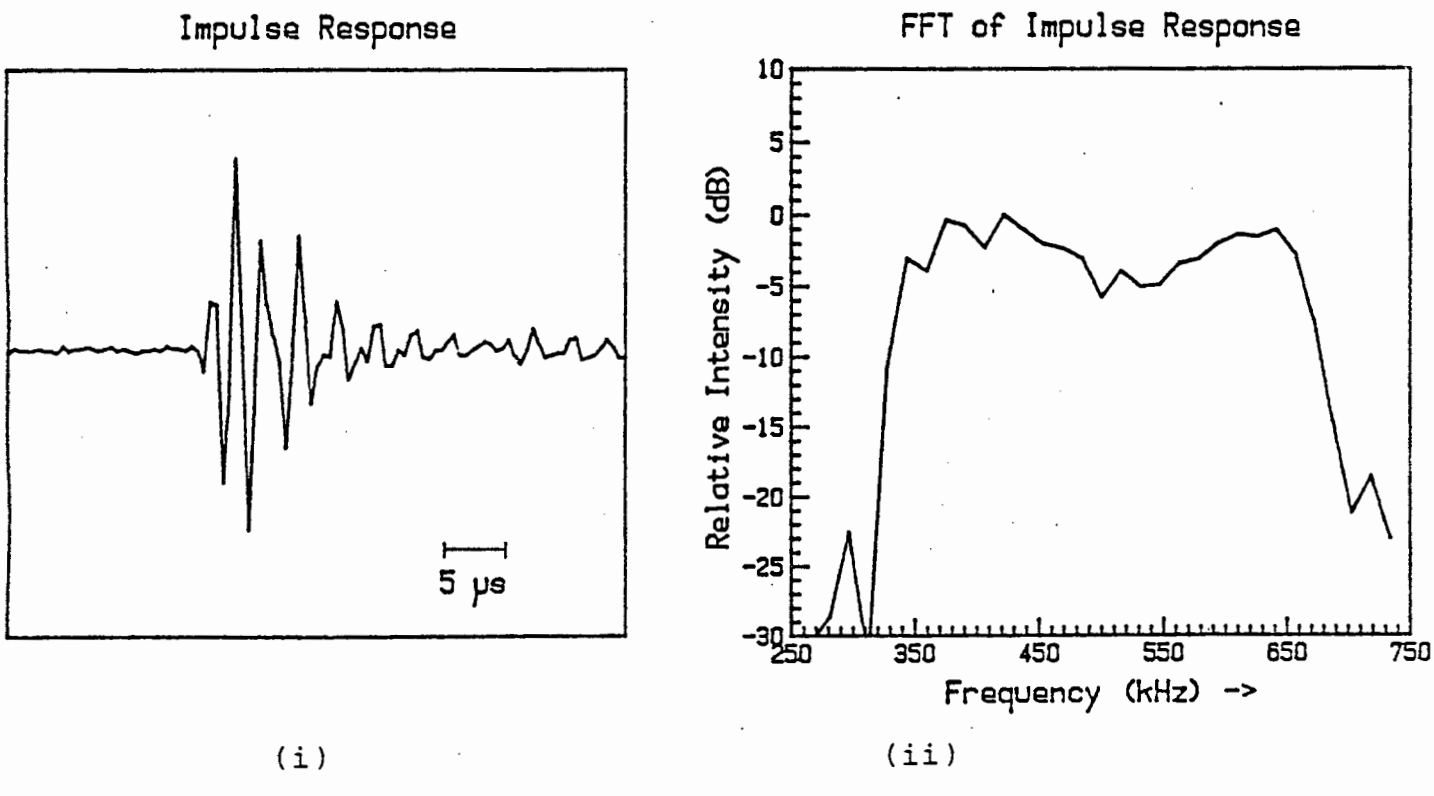

Figure 5.14: (i) Impulse Response of pulse-echo transducer
(ii) FFT of Impulse Response.

therefore that temperature effects on the frequency response of the transducer are negligible. The transducer is then placed in glycerine at temperatures of 11°C, 22°C and 33°C and the coresponding frequency responses are determined by recording the impulse response of the pulse-echo transducer for each case and computing its FFT. These are plotted as shown in Figure 5.15 (ii). Note that each curve is normalised with respect to its highest value and, therefore, at any particular frequency, the difference between two curves does not represent the actual attenuation. From the graphs of Figure 5.15, it is found that the attenuation of glycerine as a function of frequency is more pronounced at low temperatures. As the temperature rises, the attenuation characteristics of the medium become similar to those of water.

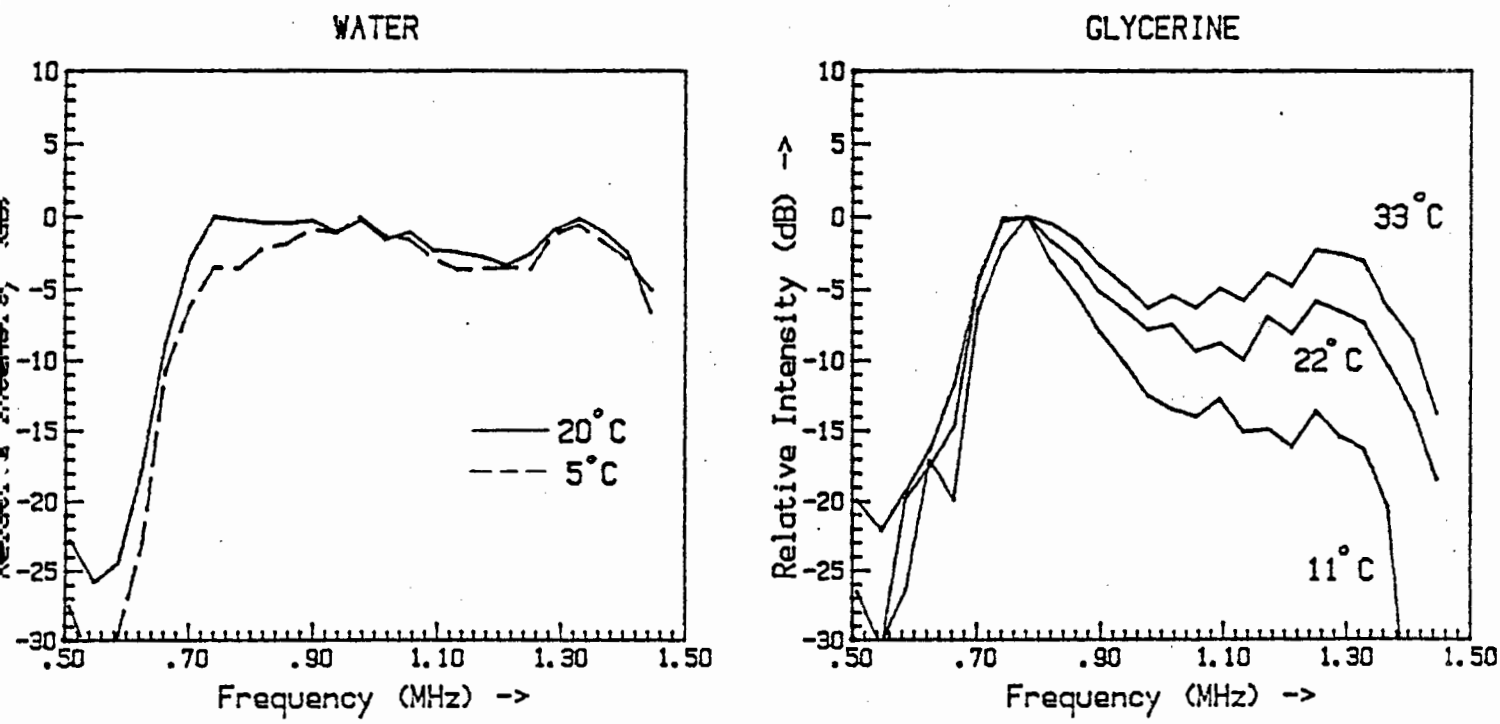

Figure 5.15: (i) Frequency responses of 1 MHz pulse-echo transducer in water at 5°C and 20°C.
(ii) Frequency responses of same transducer placed in glycerine at 11°C, 22°C and 33°C.

5.6 Discussion of Results

The implementation of acoustic impedance matching on PZT5A thickness-mode transducers has proved very successful, especially when two quarter-wave matching sections were used. Further improvements in bandwidth were obtained by the combined use of electrical and acoustic impedance matching. At 500 kHz, the 3-dB bandwidth of the transducer increased from 50 kHz (28 %) for the unmatched case to 138 kHz (28 %) with a 2-way Insertion Loss of 12 dB when both electrical and acoustic matching were used. Similarly, at 1 MHz, the 3-dB bandwidth increased from 0.10 MHz (10 %) to 0.83 MHz (72 %) with an accompanying 2-way Insertion Loss of 16 dB.

The findings of Chapter 3 on the effects of the D/λ ratio on the performance of a thickness-mode transducer were again confirmed by the use of two 500 kHz transducers of different diameters in an impedance matching experiment. The transducer of diameter 40 mm and D/λ ratio 13 produced much better results than the one of diameter 20 mm and D/λ ratio 7 as illustrated by the graphs of Figure 5.7.

Finally, the FFT technique was used to determine the frequency responses of two pulse-echo transducers in water. A comparison of these curves with those obtained by direct measurement indicated that there was good agreement between them and, thus, confirmed the validity of the FFT technique. The analysis of the absorption characteristics of glycerine as a function of temperature and frequency illustrated how the FFT technique could be used effectively in an attenuation measurement system.

CHAPTER 6

CONCLUSION

The main objective of this thesis was to design and construct low-loss wideband ultrasonic transducers using piezoceramics for use in an ultrasound attenuation measurement system operating in the frequency range 100 kHz-10 MHz. This forms part of a current research programme of the Council for Mineral Technology in the measurement of the concentration of graphite particles in suspension in an agitated pulp. Preliminary work indicated that the most suitable transducers for this application were piezoceramic disks vibrating in thickness-mode. However, due to their inherent narrowband characteristics when operating in water, special design techniques involving the use of electrical and acoustic impedance matching have to be used. To acquire an understanding of the various aspects of wideband piezoelectric transducers, investigations were carried out in three related fields, namely,

(i) a study of the resonance spectra of the various modes of disk and rod vibration and their application in material characterisation.

(ii) a study of the radiation characteristics of thickness-mode transducers as a function of the D/λ ratio.

(iii) the implementation of acoustic and electrical impedance matching techniques on piezoceramic transducers for low-loss wideband applications.

In Chapter 2, a number of disks and rods of various materials were excited in their longitudinal, flexural and in-plane modes of vibration and their resonance spectra were accurately determined by a pulse-echo technique. The elastic constants of the materials, i.e. Poisson's ratio and Young's modulus, were then determined by a calculation scheme which made use of their resonance spectra. The piezoelectric coupling of certain in-plane modes of vibration of thin disks, e.g. the "breathing" mode, was also demonstrated by the pulse-echo technique. Their

positions relative to the other modes in the frequency spectrum were carefully noted . It was found that generally, for a thin disk, the in-plane and thickness mode resonance spectra were remote from one another and, thus, interaction between the two was unlikely for most materials.

Chapter 3 was devoted to a study of the radiation characteristics of thickness-mode transducers. This was performed in two parts: the first part consisted of investigating the effects of the D/λ ratio on the Radiation Impedance of a transducer; the second was a qualitative evaluation of beamwidth (or directivity) and extent of near-field of circular thickness-mode transducers as functions of the D/λ ratio. Experiment showed that the resistive component of Radiation Impedance, and therefore the acoustic coupling between the transducer and the loading medium, reached a maximum at $D/\lambda = 13$. This observation has important implications on the design of wideband transducers where efficient transfer of energy between the transducer and the load is the important criterion. As far as the beam characteristics are concerned, it was found experimentally that the same D/λ ratio, i.e. $D/\lambda=13$, gave the best compromise between echo amplitude and sensitivity to transmitter-reflector parallelism in pulse-echo applications where transmitter-reflector distances were typically 15 cm. Both experimental observations relating to acoustic coupling and beamwidth suggest therefore that when designing thickness-mode ultrasonic transducers for broadband applications in the low megahertz region, the dimensions of the transducers must be chosen so that their D/λ ratios lie between 10 and 15.

The implementation of electrical impedance matching techniques for enhancing the bandwidths of piezoceramic transducers operating in thickness-mode was carried out in Chapter 4 on a number of PZT5A disks of resonant frequencies 500 kHz and 2 MHz. Significant improvements in bandwidth were obtained at both frequencies: the 3-dB bandwidth of a 500 kHz PZT5A transducer of diameter 40 mm and a D/λ ratio of 13 improved from 45 kHz for the unmatched case to 115 kHz when an electrical matching section was included. The accompanying loss in echo amplitude was 11 dB. Similarly at 2 MHz, electrical

impedance matching improved the 3-dB bandwidth of a PZT5A transducer of diameter 10 mm with a D/λ ratio of 13 from 0.17 to 0.89 MHz with an accompanying loss of 3 dB in echo amplitude. The effects of the D/λ ratio on the frequency characteristics of a transducer were also demonstrated by the calibration of four 2 MHz transducers of D/λ ratios varying between 7 and 53. Best performance in terms of bandwidth and efficiency was obtained with the transducer having a D/λ ratio of 13, thereby confirming the findings of the previous chapter.

Finally, the implementation of acoustic impedance matching was investigated in Chapter 5 where two PZT5A transducers of resonant frequencies 500 kHz and 1 MHz respectively were each implemented with 1 and 2 quarter-wave matching sections. Improvements in bandwidth were particularly significant in the case where 2 sections were used. The acoustically matched transducers were then matched electrically as well to further improve their frequency characteristics. The 3-dB bandwidth of a 500 kHz PZT5A disk of diameter 40 mm and a D/λ ratio of 13 increased from 50 kHz for the unmatched case to 138 kHz for the case when both acoustic and electrical matching were implemented. The resulting 2-way Insertion Loss was 12 dB. Under similar matching conditions, the 3-dB bandwidth of a 1 MHz PZT5A transducer of diameter 20 mm and a D/λ ratio of 13 increased from 0.1 MHz to 0.83 MHz with an accompanying 2-way Insertion Loss of 16 dB. An alternative method for determining the frequency response of a pulse-echo system based on the evaluation of the Fast Fourier Transform (FFT) of the Impulse Response of the system was developed and successfully verified. Its effective application in an ultrasound attenuation measurement system was then illustrated by way of an experiment to investigate the effects of temperature and frequency on the absorption characteristics of glycerine.

APPENDIX A1

c/c_0 as a function of D/λ and σ:

D/λ	σ						
	0.10	0.15	0.20	0.25	0.30	0.35	0.40
0.00	1.00000	1.00000	1.00000	1.00000	1.00000	1.00000	1.00000
0.05	0.99984	0.99982	0.99975	0.99961	0.99944	0.99924	0.99901
0.10	0.99975	0.99943	0.99896	0.99843	0.99774	0.99694	0.99602
0.15	0.99941	0.99868	0.99766	0.99655	0.99543	0.99362	0.99187
0.20	0.99899	0.99754	0.99568	0.99353	0.99054	0.98732	0.98373
0.25	0.99816	0.99581	0.99287	0.98909	0.98466	0.97967	0.97419
0.30	0.99710	0.99362	0.98906	0.98337	0.97601	0.96979	0.96214
0.35	0.99556	0.99038	0.98366	0.97572	0.96685	0.95739	0.94747
0.40	0.99323	0.98569	0.97627	0.96559	0.95410	0.94218	0.93007
0.45	0.98951	0.97866	0.96592	0.95226	0.93810	0.92367	0.91001
0.50	0.98296	0.96771	0.95135	0.93479	0.91854	0.90277	0.88758
0.55	0.97014	0.95037	0.93119	0.91285	0.89549	0.87899	0.86333
0.60	0.94487	0.92436	0.90502	0.88683	0.86964	0.85341	0.83830
0.65	0.90658	0.89089	0.87432	0.85890	0.84222	0.82709	0.81261
0.70	0.86495	0.85471	0.84201	0.82861	0.81466	0.80110	0.78792
0.75	0.82653	0.82089	0.81074	0.79983	0.78815	0.77632	0.76452
0.80	0.79506	0.78893	0.78202	0.77332	0.76355	0.75330	0.74284
0.85	0.76443	0.76167	0.75044	0.74043	0.74125	0.73236	0.72310
0.90	0.74015	0.73812	0.73402	0.72826	0.72150	0.71355	0.70532
0.95	0.71949	0.71791	0.71454	0.70967	0.70365	0.69652	0.68944
1.00	0.70156	0.70059	0.69768	0.69344	0.68814	0.68203	0.67557
1.20	0.65419	0.65266	0.65030	0.64712	0.64321	0.63869	0.63368
1.40	0.62536	0.62435	0.62361	0.62048	0.61687	0.61284	0.60844
1.60	0.61393	0.61319	0.60815	0.60479	0.60111	0.59713	0.59290
1.80	0.60165	0.60130	0.59869	0.59526	0.59136	0.58731	0.58301
2.00	0.59080	0.59067	0.59326	0.58932	0.58524	0.58101	0.57664
∞	0.60213	0.59491	0.58804	0.58148	0.57516	0.56903	0.56301

Table A1: c/c_0 as a function of D/λ and σ

APPENDIX A2

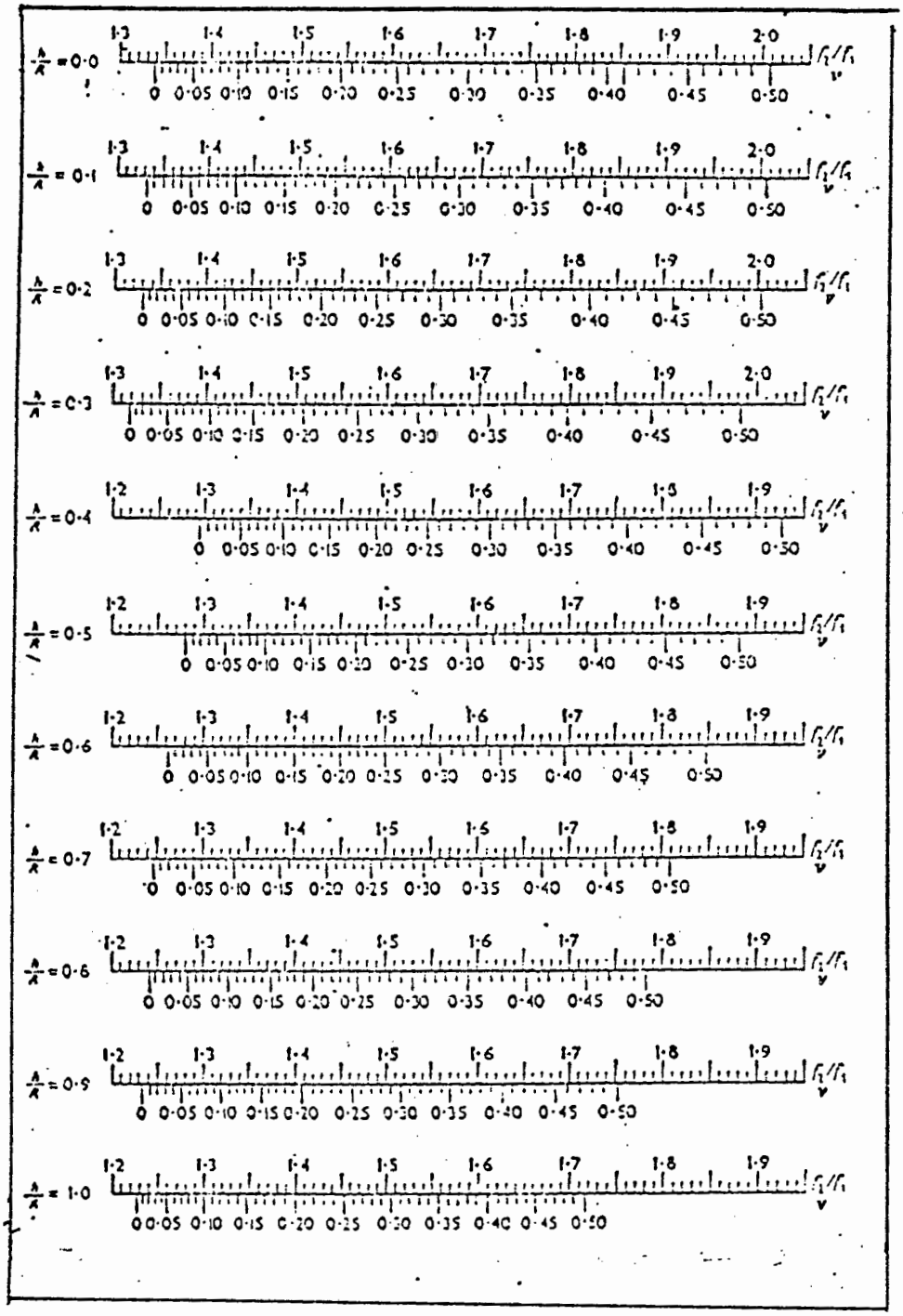

Values of $\bar{\omega}$ for the second natural vibration

h/R	0	0·25	0·50	0·75	1·00	1·25	1·50
ν = 0	0	0·554	0·942	1·188	1·351	1·460	1·532
ν = 0·15	0	0·583	0·997	1·243	1·404	1·525	1·603
ν = 0·30	0	0·626	1·055	1·316	1·482	1·594	1·681
ν = 0·50	0	0·713	1·168	1·436	1·597	1·712	1·788

Nomograms and Table used for determining Youngths modolus and Poisson's ratio using the first two modes of flexural vibrations of a free disk.

APPENDIX A3

Table A3.1

K. R. Chaplain Tables. K = Wa/Cp

IGMA	1,R	.2,R	1,1	2,1	1,2	1,3	1,4	SIGMA
=0.00	1.84118	5.33144	1.74965	3.53782	1.65192	2.50683	3.23202	0.00
-0.01	1.84886	5.3333	1.74819	3.53764	1.64396	2.49623	3.21990	0.01
=0.02	1.85647	5.33533	1.74652	3.53750	1.63595	2.48547	3.20752	0.02
=0.03	1.86403	5.33727	1.74464	3.53740	1.62788	2.47458	3.19491	0.03
=0.04	1.87153	5.33921	1.74256	3.53735	1.61976	2.46354	3.18206	0.04
=0.05	1.87898	5.34115	1.74027	3.53733	1.61158	2.45236	3.16897	0.05
=0.06	1.88637	5.34309	1.73777	3.53734	1.60334	2.44104	3.15565	0.06
=0.07	1.89371	5.34503	1.73507	3.53738	1.59505	2.42958	3.14211	0.07
=0.08	1.90099	5.34697	1.73217	3.53745	1.58670	2.41800	3.12835	0.08
=0.09	1.90822	5.34891	1.72906	3.53754	1.57830	2.40627	3.11437	0.09
=0.10	1.91959	5.35084	1.72575	3.53764	1.56984	2.39442	3.10018	0.10
=0.11	1.92252	5.35278	1.72223	3.53776	1.56132	2.38243	3.08577	0.11
=0.12	1.92959	5.35471	1.71852	3.53788	1.55274	2.37032	3.07116	0.12
=0.13	1.93661	5.35665	1.71460	3.53801	1.54410	2.35808	3.05634	0.13
=0.14	1.94359	5.35858	1.71048	3.53813	1.53541	2.34571	3.04131	0.14
=0.15	1.95051	5.36051	1.70617	3.53823	1.52666	2.33321	3.02608	0.15
=0.16	1.95739	5.36244	1.70165	3.53832	1.51784	2.32058	3.01065	0.16
=0.17	1.96421	5.36437	1.69693	3.53838	1.50897	2.30785	2.99502	0.17
=0.18	1.97099	5.36630	1.69201	3.53839	1.50003	2.29495	2.97920	0.18
=0.19	1.97773	5.36823	1.68690	3.53835	1.49103	2.28194	2.96317	0.19
-0.20	1.98441	5.37015	1.68158	3.53825	1.48197	2.26881	2.94695	0.20
-0.21	1.99105	5.37200	1.67607	3.53807	1.47284	2.25555	2.93054	0.21
=0.22	1.99765	5.37401	1.67036	3.53779	1.46365	2.24216	2.91393	0.22
0.23	2.00420	5.37593	1.66445	3.53740	1.45439	2.22865	2.89712	0.23
0.24	2.01071	5.37785	1.65835	3.53687	1.44507	2.21500	2.88012	0.24
0.25	2.01717	5.37977	1.65024	3.53618	1.43568	2.20123	2.86292	0.25
0.26	2.02359	5.38159	1.64554	3.53530	1.42621	2.18733	2.84553	0.26
0.27	2.02997	5.38361	1.63884	3.53420	1.41668	2.17330	2.82795	0.27
0.28	2.03630	5.38553	1.63195	3.53283	1.40780	2.15913	2.81016	0.28
0.29	2.04260	5.38745	1.62485	3.53115	1.39740	2.14483	2.79218	0.29
0.30	2.04885	5.38936	1.61756	3.52912	1.38765	2.13040	2.77400	0.30
0.31	2.05506	5.39128	1.61007	3.52666	1.37783	2.11583	2.75563	0.31
0.32	2.06123	5.39319	1.60237	3.52371	1.36793	2.10112	2.73705	0.32
0.33	2.06736	5.39511	1.59448	3.52018	1.35795	2.08628	2.71827	0.33
0.34	2.07346	5.39702	1.58639	3.51599	1.34789	2.07129	2.69928	0.34
0.35	2.07951	5.39893	1.57809	3.51103	1.33774	2.05616	2.68009	0.35
0.36	2.08552	5.40084	1.56959	3.50518	1.32752	2.04089	2.66069	0.36
0.37	2.09150	5.40274	1.56089	3.49831	1.31721	2.02547	2.64108	0.37
0.38	2.09743	5.40465	1.55199	3.49029	1.30681	2.00990	2.62126	0.38
0.39	2.10333	5.40656	1.54288	3.48099	1.29633	1.99417	2.60122	0.39
0.40	2.10920	5.40846	1.53356	3.47029	1.28576	1.97829	2.58096	0.40
0.41	2.11502	5.41036	1.52403	3.45806	1.27509	1.96226	2.56048	0.41
0.42	2.12081	5.41227	1.51430	3.44422	1.26432	1.94606	2.53977	0.42
0.43	2.12657	5.41417	1.50435	3.42873	1.25346	1.92970	2.51884	0.43
0.44	2.13229	5.41607	1.49419	3.41156	1.24251	1.91318	2.49767	0.44
0.45	2.13797	5.41796	1.48318	3.39274	1.23144	1.89648	2.47626	0.45
0.46	2.14362	5.41986	1.47321	3.37231	1.22028	1.87961	2.45461	0.46
0.47	2.14923	5.42176	1.46239	3.35037	1.20900	1.89256	2.43271	0.47
0.48	2.15481	5.42365	1.45135	3.32699	1.19762	1.84533	2.41056	0.48
0.49	2.16036	5.42554	1.44009	3.30229	1.18612	1.82791	2.38315	0.49
0.50	2.16587	5.42743	1.42859	3.27635	1.17451	1.81030	2.36548	0.50

Table A3.1 (contd)

K. R. Chaplain Tables. K = Wa/Cp

SIGMA	1,5	1,6	1,7	1,8	1,9	1,10	SIGMA
0.00	3.90945	4.56565	5.21067	5.84907	6.48317	7.11431	0.00
0.01	3.89595	4.55073	5.19428	5.83116	6.46372	7.09527	0.01
0.02	3.88212	4.53540	5.17741	5.81271	6.44364	7.07155	0.02
0.03	3.86795	4.51966	5.16006	5.79370	6.42295	7.04915	0.03
0.04	3.85346	4.50353	5.14224	5.77416	6.40166	7.02609	0.04
0.05	3.83866	4.48700	5.12396	5.75409	6.37977	7.00236	0.05
0.06	3.82355	4.47009	5.10523	5.73350	6.35731	6.97800	0.06
0.07	3.80813	4.45281	5.08605	5.71241	6.33427	6.95300	0.07
0.08	3.79241	4.43515	5.06643	5.69081	6.31066	6.92373	0.08
0.09	3.77640	4.41713	5.04639	5.66872	6.28650	6.90113	0.09
0.10	3.76010	4.39875	5.02592	5.64614	6.26180	6.87428	0.10
0.11	3.74351	4.38002	5.00503	5.62308	6.23655	6.84683	0.11
0.12	3.72664	4.36094	4.98373	5.59954	6.21076	6.81878	0.12
0.13	3.70949	4.34151	4.96202	5.57554	6.18445	6.79015	0.13
0.14	3.69207	4.32174	4.93990	5.55107	6.15762	6.76095	0.14
0.15	3.67437	4.30163	4.91739	5.52614	6.13027	6.73117	0.15
0.16	3.65640	4.28118	4.89448	5.50076	6.10242	6.70082	0.16
0.17	3.63817	4.26041	4.87118	5.47493	6.07405	6.66991	0.17
0.18	3.61967	4.23931	4.84749	5.44866	6.04515	6.63845	0.18
0.19	3.60090	4.21788	4.82342	5.42194	6.01582	6.60645	0.19
0.20	3.58188	4.19613	4.79896	5.39479	5.98596	6.57386	0.20
0.21	3.56259	4.17406	4.77413	5.36719	5.95561	6.54075	0.21
0.22	3.54304	4.15166	4.74891	5.33917	5.92477	6.50709	0.22
0.23	3.52324	4.12895	4.72332	5.31071	5.89344	6.47289	0.23
0.24	3.50318	4.10592	4.69736	5.28182	5.86163	6.43816	0.24
0.25	3.43286	4.08257	4.67102	5.25250	5.82933	6.40289	0.25
0.26	3.46228	4.05891	4.64430	5.22275	5.79655	6.36708	0.26
0.27	3.44144	4.03493	4.61722	5.19257	5.76330	6.33074	0.27
0.28	3.42035	4.01063	4.58976	5.16197	5.72955	6.29387	0.28
0.29	3.39900	3.98601	4.56192	5.13094	5.69533	6.25646	0.29
0.30	3.37783	3.96108	4.53372	5.09948	5.66063	6.21852	0.30
0.31	3.35551	3.93583	4.50514	5.06759	5.62544	6.18004	0.31
0.32	3.33338	3.91026	4.47618	5.03526	5.58977	6.14102	0.32
0.33	3.31098	3.88437	4.44684	5.00251	5.55361	6.10146	0.33
0.34	3.28832	3.85815	4.41712	4.96932	5.51696	6.06136	0.34
0,35	3.26539	3.83161	4.38703	4.93569	5.47982	6.02072	0.35
0.36	3.24219	3.80474	4.35654	4.90163	5.44219	5.97955	0.36
0.37	3.21872	3.77753	4.32567	4.86712	5.40405	5.93779	0.37
0.38	3.19497	3.75000	4.29441	4.83216	5.36542	5.89549	0.38
0.39	3.17095	3.72213	4.26275	4.79675	5.32628	5.85262	0.39
0.40	3.14664	3.69391	4.23069	4.76088	5.28662	5.80920	0.40
0.41	3.12205	3.66535	4.19823	4.72456	5.24645	5.76519	0.41
0.42	3.09717	3.63644	4.16536	4.68776	5.20576	5.72061	0.42
0.43	3.07200	3.60718	4.13208	4.65050	5.16454	5.67544	0.43
0.44	3.04653	3.57756	4.09837	4.61275	5.12277	5.62968	0.44
0.45	3.02076	3.54757	4.06424	4.57452	5.08047	5.58332	0.45
0.46	2.99468	3.51721	4.02968	4.53580	5.03761	5.53634	0.46
0.47	2.96828	3.48647	3.99467	4.49657	4.99418	5.48874	0.47
0.48	2.94156	3.45534	3.95922	4.25683	4.95019	5.44051	0.48
0.49	2.91452	3.42382	3.92331	4.41657	4.90561	5.39163	0.49
0.50	2.88715	3.39191	3.88693	4.37578	4.86044	5.34210	0.50

Table A3.2

Data for Determination of Poisson's Ratio

K.R. Chaplain

Sigma	$\frac{K_{1R} - K_{13}}{K_{13}}$	$\frac{K_{21} - K_{15}}{K_{15}}$	$\frac{K_{2R} - K_{19}}{K_{19}}$	$\frac{K_{21} - K_{14}}{K_{14}}$	Sigma
0	-0.26553	-0.09506	-0.17765	0.09462	0
0.01	-0.25934	-0.09197	-0.17487	0.09868	0.01
0.02	-0.25307	-0.08877	-0.17200	0.10288	0.02
0.03	-0.24662	-0.08546	-0.16903	0.10720	0.03
0.04	-0.24031	-0.08206	-0.16596	0.11165	0.04
0.05	-0.23381	-0.07850	-0.16280	0.11624	0.05
0.06	-0.22723	-0.07485	-0.15954	0.12095	0.06
0.07	-0.22056	-0.07110	-0.15617	0.12580	0.07
0.08	-0.21382	-0.06723	-0.15271	0.13077	0.08
0.09	-0.20698	-0.06325	-0.14914	0.13588	0.09
0.10	-0.20006	-0.05916	-0.14548	0.14111	0.10
0.11	-0.19304	-0.05496	-0.14171	0.14648	0.11
0.12	-0.18692	-0.05065	-0.13783	0.15197	0.12
0.13	-0.17873	-0.04623	-0.13385	0.15760	0.13
0.14	-0.17110	-0.04169	-0.12976	0.16336	0.14
0.15	-0.16202	-0.03705	-0.12557	0.16925	0.15
0.16	-0.15651	-0.03229	-0.12126	0.17527	0.16
0.17	-0.14889	-0.02743	-0.11684	0.18142	0.17
0.18	-0.14116	-0.02246	-0.11230	0.18770	0.18
0.19	-0.13331	-0.01737	-0.10765	0.19411	0.19
0.20	-0.12535	-0.01218	-0.10288	0.20065	0.20
0.21	-0.11727	-0.00688	-0.09798	0.20731	0.21
0.22	-0.10905	-0.00148	-0.09296	0.21410	0.22
0.23	-0.10071	0.00402	-0.08781	0.22101	0.23
0.24	-0.09223	0.00962	-0.08253	0.22803	0.24
0.25	-0.08362	0.01531	-0.07712	0.23517	0.25
0.26	-0.07486	0.02109	-0.07157	0.24240	0.26
0.27	-0.06595	0.02695	-0.06588	0.24974	0.27
0.28	-0.05689	0.03289	-0.06004	0.25716	0.28
0.29	-0.04766	0.03888	-0.05406	0.26466	0.29
0.30	-0.03828	0.04493	-0.04792	0.27221	0.30
0.31	-0.02872	0.05101	-0.04163	0.27980	0.31
0.32	-0.01899	0.05710	-0.03517	0.28741	0.32
0.33	-0.00907	0.06318	-0.02854	0.29501	0.33
0.34	0.00105	0.06924	-0.02174	0.30257	0.34
0.35	0.01136	0.07523	-0.01476	0.31004	0.35
0.36	0.02187	0.08111	-0.00760	0.31740	0.36
0.37	0.03260	0.08686	-0.00024	0.32458	0.37
0.38	0.04355	0.09243	0.00731	0.33153	0.38
0.39	0.05474	0.09778	0.01507	0.33821	0.39
0.40	0.06617	0.10286	0.02305	0.34457	0.40

REFERENCES

1. W.P. Mason, " An electromechanical representation of a piezoelectric crystal used as a transducer", Physical Acoustics, vol. 1, Academic, pp 353-364, 1964.

2. R. Krimholtz, D.A. Leedom, G.L. Matthei, " New equivalent circuit for elementary piezoelectric transducers ", Electronics Letters, vol. 6, pp 398-399, 1970.

3. G. Hayward, M.N. Jackson, " Discrete time modeling of the thickness-mode piezoelectric transducer ", IEEE Trans. on Sonics and Ultrasonics, vol SU-31, pp 137-150, 1984.

4. G. Kossoff, " The effects of backing and matching on the performance of piezoelectric ceramic transducers ", IEEE Trans. on Sonics and Ultrasonics,vol SU-13, pp 20-30, 1966

5. J.H. Goll, B.A. Auld, " Multilayer impedance matching schemes for broadbanding of water-loaded piezoelectric transducers and high Q electric resonators", IEEE Trans. on Sonics and Ultrasonics, vol. SU-22, pp 52-53, 1975.

6. C.S. Desilets, J.D. Fraser, G.S. Kino, " The design of efficient broadband piezoelectric transducers ", IEEE Trans. on Sonics and Ultrasonics, vol. SU-25, pp 115-125, 1978.

7. J. Souquet, P. Defranould, J. Desbois, " Design of low-loss wideband ultrasonic transducers for non-invasive medical application ", IEEE Trans. on Sonics and Ultras., vol. SU-26, pp 75-81, 1979.

8. M. Houze, M.G. Gazalet, J.M. Rouvaen, B. Nongaillard, E. Bridoux, " Adjustment of piezoelectric transducer parameters for bandwidth enhancement ", Ultrasonics, pp 276-280, 1985.

9. A.E.H. Love, " A treatise on the mathematical theory of elasticity ", 4th edition, Camb. Univ. Press, 1927.

10. P.M. Morse, " Vibration and Sound ", Mc Graw-Hill, 1948.

11. J.F.W. Bell, J.Y.F. Chen, "Pulse-echo method of determining the elastic constants of rectangular strips and square plates ", NDT International, pp 325-327, 1981.

12. J.F.W. Bell, A.C. Johnson, J.C.K. Sharp, " Pulse-echo method of investigating the properties of mechanical resonators ", J.A.S.A., vol. 57, pp 1085-1093, 1975.

13. L.E. Kinsler, A.R. Frey, A.B. Coppens, J.V. Sanders, "Fundamentals of Acoustics", 3rd edition, Wiley, 1982.

14. D. Bancroft, " The velocity of longitudinal waves in cylindrical bars ", Physical Review, vol. 59, pp 588-593, 1941.

15. A.W. Leissa, " Vibration of Plates ", NASA SP-160, 1969.

16. K.R. Chaplain, Ph.D thesis, Univ. of Aston, 1978.

17. G. Martincek, " The determination of Poisson's ratio and the dynamic modulus of elasticity from the frequencies of the natural vibration of thick circular plates", Journal of Sound and Vibration, vol. 2, pp 116-127, 1965.

18. W. Sachse, N.N. Hsu, " Ultrasonic transducers for materials testing and their characterisation ", Physical Acoustics, vol. XIV, pp 375-393, 1979.

19. R.E. Collin, " Theory and design of wideband multisection quarter-wave transformers ", Proc. IRE, 43, pp 179-185, 1955.

20 HP-85 Manual on Waveform Analysis Pac.